IMPACT BEHAVIOUR OF UNIFORM AND LAYERED ALUMINIUM MATRIX SYNTACTIC FOAMS

Thesis submitted in accordance with the requirements of the University of Liverpool for degree of Doctor in Philosophy

by

Chen Liang

March 2021

ABSTRACT

Aluminium matrix syntactic foams (AMSFs) are composite materials consisting of hollow ceramic microspheres (CMs) embedded in a metal matrix. They have higher specific stiffness, specific strength and energy absorption capacity than metal foams or polymeric syntactic foams. They are promising candidate materials for energy absorption applications, e.g. crash protection, packing materials and damping panels.

The present study focuses on the fabrication of AMSFs and characterisation of their mechanical properties under static and dynamic loading. CMs with three different particle size ranges, large - 250-500 μm, medium - 125-250 μm and small - 70-125 μm, were used. Three types of AMSFs were fabricated: uniform, layered and mixed structures. Uniform AMSFs contain large, medium or small CMs alone. Double-CM layered AMSFs contain half each of large and small CMs, and have six layer structures. Triple-CM layered AMSFs contain one third each of large, medium and small CMs, and have three different layer structures. Fully mixed AMSFs contain a single layer of fully mixed large and small CMs, and have three different proportions. Partly mixed AMSFs contain several layers of fully mixed large and small CMs, with different proportions. All AMSFs exhibited homogeneous microstructures in each layer or the whole sample with uniformly distributed CMs in the Al matrix.

Static compression tests were conducted on the AMSFs. The compressive strength of uniform AMSFs increased with decreasing CM size. The results show that the compressive strength of layered AMSFs increased with increasing number of layers and reducing layer thickness. Layer order had no effect on compressive strength, with soft layers failing before strong layers regardless the relative layer locations. The compressive behaviour of mixed AMSFs was similar to uniform AMSFs, with the compressive strength higher than the average strength of the uniform AMSFs containing the same constituent CMs.

Low speed impact tests were performed on the AMSFs. Three failure modes, ductile, brittle and ductile-brittle, were observed. Uniform AMSFs with smaller CMs and layered AMSFs with more layers had higher peak stresses. Mixed AMSFs had a higher peak stress than the average of peak stresses of their constituent layers, while layered AMSFs had a lower peak stress than the average of peak stresses of their constituent layers. Layered AMSFs showed better

ductility than uniform and mixed AMSFs. The ductility of AMSFs decreased with increasing impact energy. Both peak stress and energy absorption were found to increase with impact energy, but not significantly affected by impact momentum.

The energy absorption capacity of the different types of syntactic foams was compared. The energy absorption was mainly determined by the type of CMs in the AMSFs and was less affected by the structure. Uniform AMSFs with smaller CMs and layered AMSFs with more layers had higher energy absorption. Mixed AMSFs had higher energy absorption than the average of the uniform AMSFs containing the same constituent CMs.

An analytical model has been developed to simulate the stress and strain evolutions in ASMFs under impact loading. Impact loading generates an elastic wave and a plastic wave at the top of specimen. The elastic wave turns into a plastic wave when it bounces back at the bottom of the specimen. The two plastic waves then propagate inside the specimen with the same speed but opposite directions. The analytical model captures the key characteristics of stress fluctuation during impact. Both the inertia stress, caused by movement of particles in the specimen, and the contact stress, caused by momentum loss of impactor, can also be calculated by the analytical model. Experimental stress was caused by momentum loss of impactor. Theoretical predictions of evolutions of the base stress, which is the sum of inertia stress and contact stress, and the strain during impact agreed well with the experimental results.

Acknowledgement

Foremost, I would like to express my sincere gratitude to my supervisor Prof. Yuyuan Zhao for the continuous support for my PhD study and research, for his patience, enthusiasm and immense knowledge. His guidance helped me in all the time for research and writing of this thesis. Especially theoretical work and analytical model of this thesis. I could not have imagined having a better advisor and mentor for my PhD study.

Besides my supervisor, I would like to thank Dr. Liping Zhang for the guidance and support for my experimental work. Her suggestion in material, equipment and method helped me in all the experimental procedure. I thank her for her encouragement, insightful comments and support.

My thanks also go to University of Liverpool and China Scholarship Council, for offering me a PhD studentship. Their support helped me pursue my PhD. It is my dream to study in an advanced academic environment in a country like UK. My view is expanded, and it is only possible due to their support.

I thank my fellow lab mates in University of Liverpool: Yue Zhang, Kaikan Diao, Xianke Lu, Pengcheng Zhu, Zhining Wu and Zejun Wang, for the stimulating discussions, for the physical and mental support in the study, for all the fun we have had in the last four years.

Last but not least, I would like to thank my family: my parents Xiaoji Liang and Huiqin Yang, for giving birth to me at the first place and solid support throughout my life and my PhD study.

Publications

[1] C. Liang, Y. Y. Zhao. Experimental and Analytical Study on Homogeneous and Layered Al Matrix Syntactic Foams under Impact. *International Journal of Impact Engineering*, 153 (2021) 103861.

[2] C. Liang, Y. Y. Zhao. Quasi-Static and Impact Response of Graded Aluminium Matrix Syntactic Foams. *Materials Science Forum*, 933 (2018) 246-255.

CONTENTS

List of Symbols

A cross sectional area of specimen

c_0 speed of elastic wave

c_1 speed of plastic wave

$c_{1(n-1)}$ plastic wave speed in cycle $n-1$

E elastic modulus

f_{CM} volume fraction of CM

h_0 initial specimen height

h_A initial height of zone A

h_B initial height of zone B

h_n specimen height in cycle n

h_X initial height of zone X

h_Y initial height of zone Y

M mass of impact hammer

P plastic modulus

P_v porosity in the CM powder

t time

Δt cycle time

Δt_{n-1} cycle time in cycle $n-1$

v_0 initial impact speed

v_{n-1} impact velocity in cycle $n-1$

Δv impact velocity change between two adjacent cycles

ε total strain

ε_A strain in zone A

ε_B strain in zone B

ε_X strain in zone X

ε_Y strain in zone Y

ε_z strain in zone z

ε_y yield strain

ρ_0 initial AMSF density

ρ_{n-1} AMSF density of cycle $n-1$

ρ_m density of metal matrix

ρ_f density of syntactic foam

ρ_s density of solid part of the cellular spheres

ρ_e density of the cellular spheres

σ_b base stress

σ_c contact stress

σ_i inertia stress

σ_y yield stress

$\sigma_{A(1)}$ stress in zone A in cycle 1

$\sigma_{B(1)}$ stress in zone B in cycle 1

$\sigma_{X(1)}$ stress in zone X in cycle 1

$\sigma_{Y(1)}$ stress in zone Y in cycle 1

$\sigma_{z(n)}$ zone stress in cycle n

φ porosity of the syntactic foams

$L_{0\mathrm{R}}$ initial wood cylinder length in Reid's approach

$A_{0\mathrm{R}}$ cross sectional area in Reid's approach

$\rho_{0\mathrm{R}}$ initial density in Reid's approach

M_R impact mass in Reid's approach

v_{0R} impact velocity in Reid's approach

σ_{crR} stress ahead of the shock in Reid's approach

ε_{1R} locking strain in Reid's approach

σ_R^* impact stress in Reid's approach

t_R time in Reid's approach

x_R deformed length of the crushed wood in Reid's approach

δt_R time increment in Reid's approach

u_R displacement of the rigid mass in Reid's approach

x_{0R} the un-deformed length of the crushed portion in Reid's approach

L_R un-deformed length of the wood in Reid's approach

v_R current velocity of the rigid mass in Reid's approach

ρ_{1R} density when fully crushed in Reid's approach

γ_R density ratio in Reid's approach

ε_{1R} strain in Reid's approach

c_{sR} shock speed in Reid's approach

δm_R mass increment of shaded element in Reid's approach

δx_R distance increment in Reid's approach

List of Figures

List of Tables

Chapter 1 Introduction

1.1 Motivation

Aluminium matrix syntactic foams (AMSFs) are a novel class of lightweight composite materials, which use hollow particles known as ceramic microballoons (CM) such as alumina cenospheres (Kiser *et al*. 1999; Alizadeh *et al*. 2012) and fly ash (Rohatgi *et al*. 2002; Rohatgi *et al*. 2009) to embed in aluminium matrix. The main role of microballoons is to introduce porosity. AMSFs offer advantages of low weight, high specific stiffness, high damage tolerance, and high mechanical energy absorption capabilities. In comparison with polymeric syntactic foams, AMSFs have higher strength and can be used at higher temperatures. In comparison with metal foams or porous metals, AMSFs have higher compressive yield strength and better energy-absorption capacity, due to the extensive strain accumulation at relatively higher plateau stress, although they usually have higher density. These properties of AMSFs lead to many applications. AMSFs are used as core layer in sandwich structure, crash protection and damping panels (Zhao *et al.* 2009). Energy absorption capacity is usually affected by porous structure. It is possible to design syntactic foams with various kind of hollow spheres (Goel *et al*. 2015) for various applications. Hollow spheres can be divided into different densities and sizes by flotation methods and sieves.

AMSFs are normally manufactured with pressure infiltration to acquire homogeneous structure. The main disadvantage of this method is that the volume percentage of ceramic particles in the syntactic foam is largely fixed, around 63% (Hartmann *et al*. 1999) when the particles have a similar size and are randomly packed. In impact loading, stress evolution is not evenly distributed across the specimen, which means homogeneous AMSFs are not

structurally fit for impact loading. Functionally graded syntactic foams (FGSFs) have a gradual and controlled positional change of at least one property. FGSFs have been proposed and manufactured in different industries (Jamil *et al*. 2017; Gupta *et al*. 2006; Movahedi *et al*. 2019).

In order to optimise the physical and mechanical property of syntactic foams to the desired level, it is important to keep each layer independent during fabrication. Traditional solution is to fabricate each layer independently and then bond layers together with adhesive like epoxy. However, graded structures manufactured from this approach have poor structural integrity between layers. FGSFs manufactured by one-step infiltration casting have a better structural integrity and mechanical properties (Pham *et al*. 2018).

Nowadays, most studies have focused on the energy absorption capacity in FGSFs, few has studied if FGSFs have sufficient ductility to match the energy absorption capacity. Besides, the theoretical explanation on impact response in FGSFs is not thoroughly. This work have studied the match between energy absorption capacity and impact ductility of layered syntactic foams, and the analytical explanation on the impact stress evolution.

1.2 Objectives and contributions

The primary objective of this study is to fabricate AMSFs with different structures (uniform, graded, mixed), to study their mechanical properties and to investigate the effect of impact loading on mechanical property. The specific objectives to be achieved by experimental work and analytical modelling are as follows.

The effect of material parameters is studied. Including the effect of CM size and the effect of structure variation (uniform, layered and mixed) on the compressive strength and energy absorption behaviour.

The effect of loading parameters is studied based on the failure mode. Loading parameters include impact velocity, impact momentum and impact energy, on the impact peak stress, energy absorption and impact ductility in AMSFs is studied.

An analytic model for impact loading is developed to theoretically understand the stress evolution and strain evolution in AMSFs under impact loading. Experimental results is compared with the prediction of analytic model.

The original contributions of this work are: manufacturing layered syntactic foam with the structure benefit of increasing impact ductility without compromising energy absorption capacity, in comparison with uniform structure. Proposing a way to study impact ductility by judging if the syntactic foam have sufficient ductility to fulfil its energy absorption capacity. Explaining two key features in impact stress evolution, the time interval and amplitude of the fluctuation with analytical model.

1.3 Structure of thesis

A total of seven chapters are included in this thesis. Chapter 2 evaluates the relevant literature to the work presented. The manufacture methods and mechanical properties of metallic syntactic foams are first reviewed. The compressive behaviours of cellular materials are then introduced. The current understandings in the effect of impact loading on graded structure are also reviewed.

Chapter 3 gives a detailed experimental procedures used in this work, including fabrication procedures used to manufacture different types of syntactic foams, the characterization methods, and the mechanical tests for characterising the syntactic foam samples.

Chapter 4 presents the experimental results. The microstructures of the syntactic foam are presented. The calculated values of density and porosity of the syntactic foams are also presented. The mechanical properties in both quasi-static compression and impact tests are also presented. Moreover, ductility criteria are developed based on different failure mechanisms found in AMSFs.

Chapter 5 presents an analytic model for predicting the stress evolution and strain evolutions in AMSFs under impact loading. The theoretical basis of the analytic model is introduced. An iteration-based numerical solution of the model is proposed. The predictions and experimental results on both stress evolution and strain evolution are compared.

Chapter 6 presents a detailed analysis of the experimental and modelling results. The effects of material parameters and loading parameters, including ceramic sphere type, syntactic

foam structure (uniform, layered and mixed), impact velocity, impact momentum and impact energy on the mechanical properties, including strength, peak stress and energy absorption, of syntactic foams are analysed and discussed. Effects of experimental parameters on impact ductility in AMSFs are also discussed.

Chapter 7 summarises the conclusions drawn from this study and possible areas for future work.

Chapter 2 Literature Review

2.1 Introduction to syntactic foam

Syntactic foam with hollow spheres is a porous composite material with good crush strength and good energy absorption capacity. It has attracted increasing interest and attention from scientific and engineering communities. Syntactic foam materials can be applied in numerous fields such as mining, marine, transportation, civil defence and aerospace (Gibsib *et al*. 2003). For instance, due to the damping capacity and low density features, they can be used as automotive brake rotors, and steer rods, or as covers/hulls/packaging (sandwich cores) structures (Gupta *et al*. 2014; Lapcik *et al*. 2016). Their high-energy absorption capacity and high compressive strength can also be beneficial in crash energy absorption zones and protective panel applications. By applying syntactic foam for roadside barrier, the impact force can be significantly reduced while the energy absorption capacity remains (Kim *et al*. 2000). In open pit mines, syntactic foam can be applied to the edge protection, which allows narrower open pit haul roads while satisfying the safety requirement for trucks (Durkin *et al.* 2016). For marine applications, syntactic foam is able to provide buoyancy due to its light weight and withstand high water pressure for deep-sea exploration (Hinves *et al.* 1993; Le Gall *et al*. 2014; Wu *et al*. 2016).

Syntactic foam can be classified into one-phase, two-phase and three-phase foams (Wu *et al.* 2016; Pham *et al*. 2018). Typical syntactic foam consists of a filler and a binder matrix. The fillers can be made of glass, metal, ceramic in forms of micro-sphere or macro-sphere (Lau *et al*. 2006; Swetha *et al.* 2011; Geng *et al.* 2016). The binder matrix can be made of polymers,

normally epoxy (Gupta *et al*. 2006), vinyl ester (Gupta *et al*. 2010) and bismaleimide (Koopman *et al.* 2006), or metals, normally aluminium (Tao & Zhao, 2009), steel (Castro *et al*, 2012; Luong *et al.* 2015), magnesium (Xia *et al.* 2015), titanium (Mondal *et al*. 2012; Xue *et al*. 2012) and Zinc (Broxtermann *et al*. 2018). One-phase foam is formed by bonding an engineered composite sphere matrix, which is made from expanded polystyrene (EPS) beads coated with epoxy resin or fibre reinforced epoxy using "rolling ball method" (Wu *et al*, 2016). The coated EPS spheres beads can be cured and post-cured to shrink the EPS beads inside the spheres to produce a hollow structure. The hollow composite spheres are then bonded to form into a one-phase foam. To improve the mechanical properties of syntactic foams, the micro-spheres and macro spheres made of various fillers can be added and mixed with binder matrix to form two-phase and three-phase syntactic foams (Swetha *et al*, 2011; Geng *et al*, 2016).

From a structure perspective, syntactic foam can be classified into uniform syntactic foam and functionally graded syntactic foam (FGSF). FGSFs are advanced engineering materials that exhibit a gradual and controlled positional change of at least one property. The graded properties may arise from geometrical parameters such as diameter, width, wall thickness etc. They can also be caused by variable material properties including density, strength and even material type. The graded property can be a single factor alone, or multiple graded properties can take effect the same time. The graded properties can be achieved by changing the volume fraction of constituents, microstructure or material type from one location to another (Naebe *et al*. 2016). Designing FGSF with tailored properties (mechanical or physical) has the potential to produce considerable benefits. In general, the introduction of gradients in FGSF brings

greater flexibility and a wider design domain in energy-absorption structures and materials. The crashworthiness performance of these FGSFs can be further improved by appropriate design optimization (Baroutaji *et al*, 2017). There is no doubt that design optimization techniques will always play an important role in this process to obtain optimal solutions with different objectives, constraints and design variables.

As syntactic foam is mainly designed for mechanical applications and the main loading mode is compression, the compressive behaviour of syntactic foams has been widely studied (Kiser *et al*, 1999; Rohatgi *et al*, 2006; Daoud *et al*, 2007; Orbulov *et al*, 2012; Santa Maria *et al*, 2014). Due to its importance, the testing methodology and characteristic properties of syntactic foams under quasi-static loading have been described in standard procedures (DIN 50134 standard, 2008). Dynamic loading is also important from the perspective of collision damper or protective applications. In dynamic studies, dynamic loading is normally applied with either Split Hopkinson Pressure Bar (SHPB) for high strain rate (Luong *et al*, 2011), or drop weight impact for low strain rate (Hebert *et al*, 2008). However, the effect of dynamic loading has not been investigated as fully as compression, for example, deformation mechanism under dynamic loading.

In this chapter, syntactic foams with both uniform and graded structures will be reviewed, including fabrication methods, microstructural characteristics and mechanical properties. Meanwhile, current investigations on the effects of compressive loading, both quasi-static and dynamic/impact, on mechanical properties such as peak strength, energy absorption and ductility will also be reviewed.

2.2 Syntactic foams with uniform structure

2.2.1 Polymeric syntactic foam

2.2.1.1 Fabrication process

The three primary constituents used in the fabrication of polymeric syntactic foams are (i) matrix material (epoxy resin), (ii) porosity provider material (hollow spheres) and (iii) curing agent to cure the matrix material (Huang *et al*, 2016). A fourth constituent, a diluent, which helps in lowering the viscosity of the resin, is sometimes used (Woldesenbet *et al.* 2005).

Fabrication of polymeric syntactic foams is carried out with two primary steps: mixing and casting. The resin is heated to a liquid form before mixing. The hollow spheres are added to the epoxy resin matrix in multiple steps (Huang & Li, 2015) and mechanically mixed with epoxy resin thoroughly using a stirrer. Ultrasonic mixing is applied in some cases by immersing an ultrasonic probe in the mixture to improve mixing further (Woldesenbet, 2008). After the mixture becomes a uniform slurry, the slurry is left in a vacuum oven at room temperature to reduce the air bubbles arising during the stirring process. Subsequently, the mixture is cast in a metallic mould and cured for at least 24 h at room temperature.

Although this process is easy to operate, a few issues should be considered. Firstly, breakage of hollow spheres should be prevented during the mixing process. Apart from gentle stirring, a wooden or other soft material stirrer may be used to minimize breakage (Gupta *et al*. 2006). Secondly, different casting methods should be used according to different viscosities caused by different volume fractions of hollow spheres (Bunn *et al*. 1992). For syntactic foams with a

low volume fraction of hollow spheres, the mixture slurry has a low viscosity and can be directly poured into the mould. With an increased volume fraction, the mould has to be filled by extrusion due to the increased viscosity of the slurry. For a volume fraction of hollow spheres high than 50%, the slurry is too dry to extrude and high pressure moulding is used to produce the sample. Thirdly, different densities between hollow spheres and epoxy resin matrix can lead to inhomogeneous structure during the casting. However, the gravity-settling effect caused by different densities could be used to fabricate syntactic foams with gradient structures (Kishore *et al*. 2005).

2.2.1.2 Microstructure

The microstructure of polymeric syntactic foams consists of matrix resin and hollow microspheres. The scanning electron micrograph of a typical polymeric syntactic foam is shown in Figure 2.1 (Gupta *et al*. 2011). The microstructure of the syntactic foam after dynamic loading is shown in Figure 2.2. As the syntactic foam is made by mixing epoxy resin and microballoons by stirring followed by casting, air voids are observed in the microstructure (Gupta *et al*. 2004). Under dynamic loading, some microballoons are crushed and the foam is densified. With increased strain rate, the specimen showed higher content of uncrushed microballoons while the epoxy resin shows brittleness, indicated by cracks in the matrix.

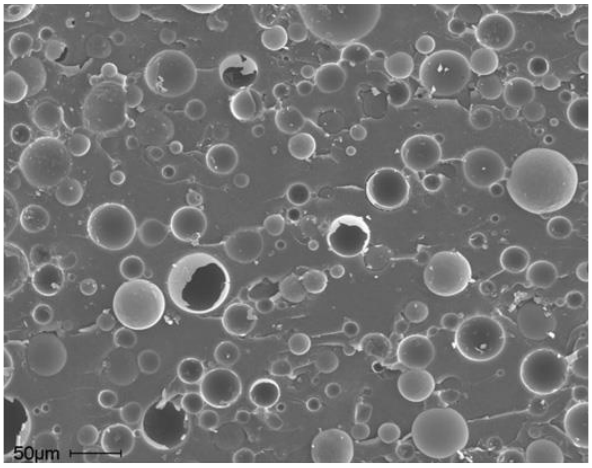

Figure 2.1 *Scanning electron micrograph of a typical syntactic foam containing glass microballoons in vinyl ester matrix (Gupta et al. 2011)*

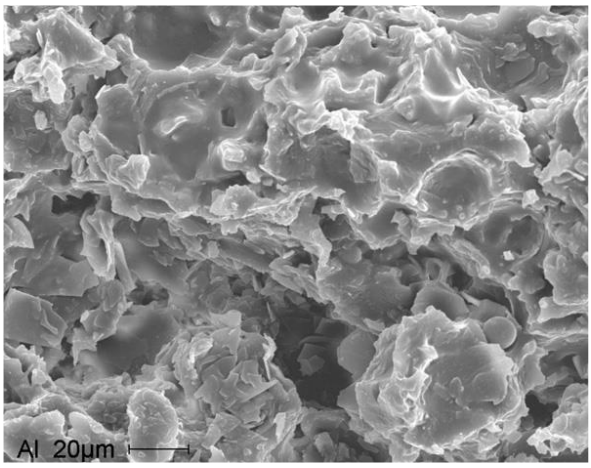

Figure 2.2 *SEM image showing the fracture surface of a syntactic foam containing glass microballoons in vinyl ester matrix tested at a strain rate of 903s^{-1} (Gupta et al. 2011)*

2.2.1.3 Mechanical property

Compressive properties of syntactic foams generally include compressive strength, energy absorption capacity and failure mechanism. The mechanical properties of syntactic foams are a function of either material parameters, such as types of constituents, volume fraction of microballoons (Gupta *et al*. 2004), wall thickness of microballoons (Woldesenbet *et al*. 2009), size of microballoons (Ahmadi *et al*. 2015) and strengthening particles (Wouterson *et al*. 2007; Li *et al*. 2008), or loading parameters in different loading conditions, such as compressive

loading (Song *et al*. 2004), tensile loading (Yu *et al.* 2012), and flexural loading (Woldesenbet *et al*. 2009).

Syntactic foams are mainly designed for impact protection purposes. Therefore, compressive properties of syntactic foams are widely investigated. Early results on compressive strength were reported by Bunn and Mottram (1993). They tested syntactic foams with volume fractions of microballoons between 0% and 53%. As the volume fraction of the microballons decreased from 53% to 0%, it was found that the bulk density increased from 0.78g/cm^3 to 1.5g/cm^3. A linear relation was observed between the filler content and the bulk density. Compressive tests showed that the lowest strength was for foams having the highest microballoon concentration. This indicates that the addition of microballoons reduced the compressive strength.

D'Almedia (1999) studied the effect of changing the diameters of the diameters of the microballoons on the mechanical properties. At a fixed volume fraction of microballoons, which act as pores inside the resin matrix, the compressive strength and elastic modulus are higher for composites fabricated with microballoons of smaller diameters. This means smaller microballoons leads to higher strength and elastic modulus. Rousseau *et al*. (2017) pointed out that the size of the embedded particulates is one of the key factors that regulates the behaviour of syntactic foam. As impact loading causes impact wave inside the specimen, the use of larger particulates promotes greater attenuation levels of such impact wave. With larger microspheres, large void pockets enhance stress wave scattering, whereas the pure epoxy matrix reduces the wave through an absorptive phenomenon.

Karthikenyan *et al*. (2000) studied the compressive strength of syntactic foams with and without fibrous reinforcements in the matrix. They found that besides physical features like voids, microstructural variations had a significant influence on the compressive behaviour. The addition of fibres in low proportions of around 2% did not increase the compressive strength, whereas the addition of fibres in high proportions, around 6%, increased the compressive strength significantly. The compressive fracture surfaces had plastic deformation marks in the form of steps. These marks cannot be generated if the matrix fractures in compression, but are possible in shear failure. The banded structure appeared due to the frequent change in the localized plane of crack propagation in specific directions. Li *et al*. (2007) pointed out that fibrous reinforcement not only increased the compressive strength, but also increased the energy absorption by providing new energy absorption mechanisms such as fibre pull-out and fibre bridge-over. SEM observations showed that syntactic foams with fibrous reinforcement could not only absorb impact energy through micro-damage, but also had mechanisms to contain and arrest micro-length scale damages and prevent them from propagating into catastrophic macrocracks. Therefore, fibrous reinforcements provided more impact damage tolerance in comparison with plain syntactic foams.

The effect of adding nanocaly in the matrix on the mechanical properties of epoxy syntactic foam has also been investigated. Ho *et al*. (2006) concluded that adding montmorillonite clay to epoxy resin hinders the linking of epoxy chains thereby decreasing the ductility of the composite. However, the hardness increased with addition of nanoclay in the epoxy, which suggests that such a composite can resist high stress but will have limited capacity for deformation. Lam *et al*. (2005) also observed that the ductility of epoxy-nanoclay composite

is less than that of plain epoxy. Balakrishnan *et al*. (2005) however stated that the decrease in ductility of the composite is not significant in the case of nanoscale particles because of formation of subcritical cracks. It was found that the addition of nanoparticles not only increases the strength of the epoxy matrix but also serves as a mechanism to contain the microcracks from developing into macrocracks. Major improvement in properties was also observed when the nanoclay was fully exfoliated and reinforced in the polymer without agglomeration (Fu *et al*.2006). The method of mixing nanoclay in epoxy resin is important to achieve effective dispersion of the nanoclay. Ultrasonication of nanoclay in epoxy resin with additional diluents produced superior nanoscale dispersion compared to shear mixing methods (Hussain *et al*. 2007).

Gupta and Nagorny (2005) studied the tensile behaviour of polymeric syntactic foams fabricated with glass microballoons with different volume fractions in the range of 30% to 60% and different wall thickness to diameter ratios. They reported that the tensile strength increases with a decrease in volume fraction of microballoons. The tensile strengths of all the syntactic foams were found to be decreased by 60%-80% compared with that of neat resin. They also studied the effect of wall thickness to diameter ratio on tensile modulus and found that foams containing low strength microballoons showed lower tensile modulus compared with the nest resin, but the presence of high strength microballoons led to an increase in the tensile modulus. Yu *et al*. (2012) stated that the mechanical behaviour of syntactic foams is dominated by brittle fracture under tensile loading. They developed a three-dimensional microstructure based finite element model by means of a representative volume element (RVE), to predict the tensile strength and associated failure modes of syntactic foams. They

introduced cohesive elements into the finite element model to capture the progressive damage behaviour of the microsphere-matrix interface.

Kim and Khamis (2001) studied the fracture characteristics of polymeric syntactic foams by varying the volume fraction of the microballoons. The specific flexural strength decreased as the volume fraction of microballoons increased. The specific fracture toughness decreased with increase in the volume fraction of microballoons. The fracture characteristics of the syntactic foams with high volume fractions of microballoons were dominated by microballoons and less affected by matrix. Maharsia *et al.* (2006) investigated the flexural properties of syntactic foams modified by rubber and nanoclay particles, developed for high damage tolerance. In the rubber hybrid foams, 40 and 75 um rubber particles, 2% by volume, were used. In nanoclay hubrid foams, the volume of nanoclay particles was maintained at 2% and 5% to study the effect of volume fraction of nanoclay particles. The total volume of all types of particles was maintained at 65% in all types of plain and hybrid syntactic foams. An increase in flexural strength was observed with the incorporation of rubber particles in syntactic foams. In nanoclay hybrid foams, flexural strength was observed to depend on the nanoclay volume fraction. The strength of microballoons played an important role in determining the fracture mode of plain and hybrid syntactic foams. Rubber particles were found to increase the energy absorption under the flexural loading conditions.

2.2.2 Metal matrix syntactic foam

2.2.2.1 Fabrication process

Most metal matrix syntactic foams (MMSFs) commonly use light metals or alloys including aluminium (A356, A380, 2014, 6061 and 7075) (Santa Maria *et al*. 2013; Ferguson *et al*. 2013; Zou *et al*. 2013) and magnesium (AM20, AM50 and AZ91) (Anantharaman *et al*. 2015) as matrix materials. While commonly used filler materials are fly-ash (Rohatgi *et al*. 2005), glass microballoons (Anbuchezhiyan *et al*. 2017), or metallic hollow spheres (Szlancsik *et al*. 2015), naturally occurring materials such as pumice (Taherishargh *et al*. 2015), expanded clay (Puga *et al*. 2018), expanded perlite (EP) (Taherishargh *et al*. 2014; Fiedler *et al*. 2015) and expanded glass (EG) (Al-Sahlani *et al*. 2017) are attractive alternatives due to a further reduction in material costs.

Metal matrix syntactic foams are normally fabricated by infiltration casting or stir casting. In infiltration casting (pressure infiltration, melt infiltration), the molten metal is pressed to infiltrate in to the packed ceramic particles and solidifies to produce a metal matrix syntactic foam. The infiltration casting process can be conducted either by a gas pressure assisted infiltration (Balch 2005) or by die casting (Rohatgi *et al*. 2009) (Zhang *et al*. 2009). The reported infiltration pressure is in the range of 0.2-3.5 MPa depending on the matrix and spheres used in the fabrication process. Marchi & Mortensen (2002) suggested that the pressure required for full infiltration is related to the size and volume fraction of spheres. Finer spheres and larger volume fractions of CMs require higher infiltration pressures. It is suggested that the heating temperature be about 100°C above the melting point of the metal matrix (Nadler *et al*. 1999). A temperature far higher than the melting point of matrix could accelerate the dissolution of ceramic spheres used for fabricating the syntactic foam (Palmer *et al*. 2007). In most cases, the packed spheres are randomly distributed and account for 63%,

i.e., the voids between the packed spheres account for about the 37%, when they have a similar size (Hartmann 1999).

In stir casting, the ceramic particles are mixed in the liquid metal and then cast to produce syntactic foams (Daoud 2008). This method is widely used in producing metal matrix composites and its advantages and limitations are well documented. The volume fraction of the ceramic particles can be easily adjusted and production cost is low. However, this method has a few problems. The ceramic particles are normally not wetted by the molten metal and tend to cluster together. They also tend to float to the top of the melt because they are much lighter than the metal. Both of these problems lead to potential poor dispersion of the ceramic particles in the liquid metal and therefore inhomogeneous structures of the syntactic foams.

2.2.2.2 Microstructure

Metallic syntactic foams fabricated by different methods can have different microstructures, as shown in Figure 2.3 and Figure 2.4. The syntactic foams fabricated by the infiltration casting method have a more uniform distribution of ceramic spheres and better bonding between metal matrix and ceramic spheres than those fabricated by the stir casting method. Some hollow spheres may be broken either when received or during packing and infiltration, and can be infiltrated with metal in both foams fabricated by the infiltration method and the stir casting method.

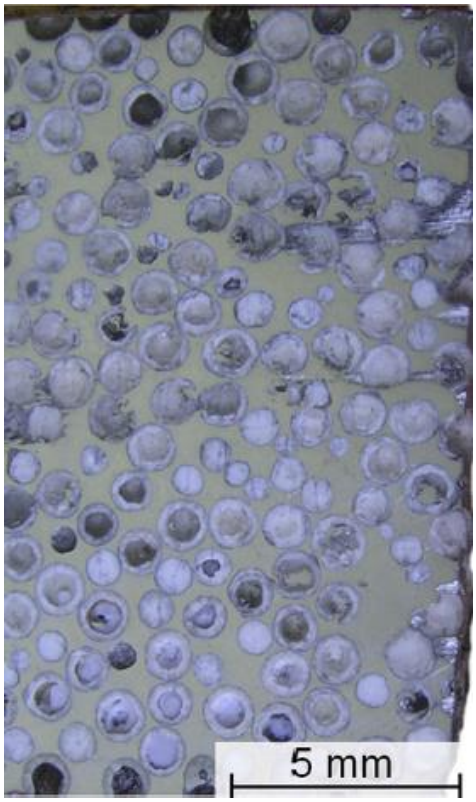

Figure 2.3 *Microstructure of metallic syntactic foam fabricated by melt pressure infiltration method (Myers et al. 2015)*

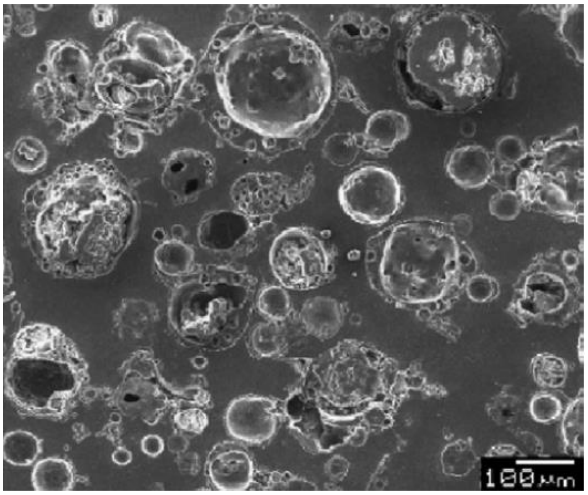

Figure 2.4 *Microstructure of metallic syntactic foam fabricated by stir casting method (Goel et al. 2014)*

In comparison to polymeric syntactic foams, the porosity of metallic syntactic foams is determined mainly by the porosity of the cellular spheres since there are normally no voids in the metal matrix. Zhang and Zhao (2007) developed a formula to calculate the porosity of metallic syntactic foams suitable for all types of cellular spheres:

$$\varphi = \frac{\rho_m - \rho_f}{\rho_m - \rho_e}\left(1 - \frac{\rho_e}{\rho_s}\right) \quad (2.1)$$

where φ is the porosity of the syntactic foams, ρ_m, ρ_f and ρ_s are the densities of metal matrix, syntactic foam and solid part of the cellular spheres, respectively, and ρ_e is the effective density of the cellular spheres.

2.2.2.3 Mechanical property

Similar to polymeric syntactic foams, mechanical property of metal matrix syntactic foams (MMSFs) also includes strength, energy absorption capacity and failure mechanism. The mechanical properties of MMSFs are a function of material parameters, like volume fraction (Rohatgi *et al*. 2006), density (Rohatgi *et al*. 2006), porosity (Tao *et al*. 2009; Santa Maria *et al*. 2013), wall thickness (Orbulov *et al*. 2013) and size (Santa Maria *et al*. 2014) of microballoons/microspheres, and loading parameters and conditions, such as quasi-static compressive loading (Tao *et al*. 2009) and dynamic/impact loading (Peroni *et al*. 2014). In this section, we focus on the mechanical properties of syntactic foams under quasi-static loading. The effect of dynamic/impact loading will be discussed separately in Section 2.4.

The compressive strength of MMSFs is largely determined by their density. However, the micro-sphere size, microsphere structure and distribution are also important parameters

determining the properties. In early research, Kiser *et al*. (1999) studied the effect of wall thickness to radius ratios (t/R) of hollow Al_2O_3 spheres on Al matrix syntactic foams. The compressive strength was found to be sensitive to t/R. With the same A202 aluminium alloy matrix, the compressive strength of the syntactic foam increased from 70 to 230 MPa with the t/R increasing from 0.12 to 0.48. Licitra *et al*. (2015) performed quasi-static compression tests on MMSFs with A356 alloy matrix and Al_2O_3 particles. They reported that lower density syntactic foams have lower modulus, compressive strength and plateau stress. Failure in the specimen was found to initiate from particle failure, followed by shear failure of matrix. The study on the compressive behaviour of syntactic foams with hollow ceramic microspheres of same composition but different densities showed similar result (Zhou *et al*. 2006). The syntactic foams with high density ceramic microspheres were found to have a higher compressive strength than those with low density microspheres. Wu *et al*. (2007) indicated that the size of the ceramic spheres also affects the compressive strength of MMSFs. Orbulov *et al*. (2014) studied various kinds of MMSFs with matrix of Al99.5, AlSi12, AlMgSi1 and AlCu5 alloys and particles of ceramic hollow spheres Al_2O_3, SiO_2 and mullite under both free and constrained quasi-static loading. MMSF with 1450 μm sphere had densification limit of 40%, while MMSF with 150 μm had densification limit of 55%. With same other parameters, they reported that the densification limit was primarily influenced by the hollow spheres' size and distribution in constrained compression. The amount of recoverable energy in the constrained compression was influenced by the applied heat treatment. The overall absorbed mechanical energy was largely influenced by the compression mode (free or constrained).

The energy absorption is defined as the area under the stress-strain curve in the compression test, up to the onset densification strain. Therefore, the energy absorption capacity of syntactic foam is generally determined by plateau stress and densification strain, as shown in Figure 2.5. The plateau stress is dependent on the strength of the constituents, i.e. the metal matrix and the ceramic particles. The densification strain, defined as the strain where the syntactic foam is densified with no pores inside, is mainly dependent on the level of porosity in the syntactic foam. Metal matrix syntactic foams have higher strength than polymer matrix syntactic foams. Therefore, they often have better capability of energy absorption. Balch *et al*. (2004) achieved specific energy absorption of 39 and 49 J/g for syntactic foams with a CP Al matrix and an Al 7075 - T6 matrix, respectively. Wang *et al*. (2013) reported that the specific mechanical properties of MMSFs are much higher than those of conventional metal foams.

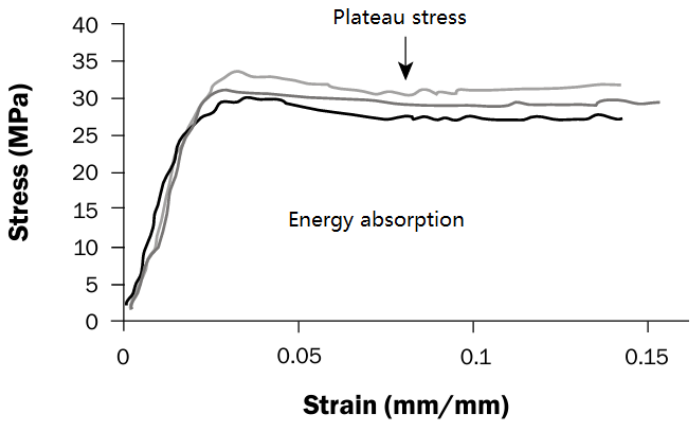

Figure 2.5 *Typical stress-strain curve for compression test of syntactic foam (Gupta et al. 2003)*

Apart from strength and energy absorption, failure behaviour is also important. Ductile failure leads to better structural integrity, stable plateau stress in the stress-strain curve and therefore a higher energy absorption, while brittle failure leads to poor structural integrity and lower energy absorption. The ductile foam materials collapse due to the crushing of

ceramic microspheres, whereas the brittle ones fail due to the shear failure in the form of cracks (Mondal *et al*. 2009). The ductility of MMSFs could sharply drop if the thickness to diameter (t/D) ratio of microspheres is too high, which may shorten the plateau regime. Three other factors can also affect the failure behaviour of MMSFs: (i) the structure of the ceramic microspheres (Wu *et al*. 2007; Orbulov *et al*. 2010), (ii) the volume fraction of the ceramic microspheres (Rohatgi *et al*. 2006) and (iii) the void defects in the metal matrix. As a consequence, the ductility of MMSFs can be tailored by selecting suitable metal matrix and ceramic microspheres.

2.3 Functionally graded structures and materials for energy absorption

Introduction of property gradients can bring greater flexibility and wider design domain in energy-absorption structures and materials. The crashworthiness of these structures and materials can be further improved by appropriate design optimization (Baroutaji *et al*. 2017). There is no doubt that design optimization techniques always play an important role in this process to obtain optimal solutions with different objectives, constraints and design variables.

However, the introduction of gradients may result in some difficulties in the fabrication or manufacturing of such structures and materials. Fortunately, this obstacle can be eliminated with the advance of manufacturing science and process technology. For example, various tailoring and forming technologies can be employed to fabricate structures with graded properties. Some mature production technologies, such as tailor welded blank (TWB), tailor rolling blank (TRB) and tailor hot stamping (THS), etc., have been widely applied in various engineering fields, especially in the automotive industry. The components produced by those

technologies are all representations of thin walled structures with graded properties. Although manufacturing metal syntactic foams with graded structures is still a challenging task, progress is being made in this field.

2.3.1 Thin-walled structures

2.3.1.1 Thin-walled structures with graded diameter

Thin-walled tapered tubes or frusta are the most simple and commonly-used structures with gradient property, as shown in Figure 2.6. They are employed to endure axial or oblique impact loads. A prior motivation of employing tapered tubes is to improve the load uniformity of energy absorbers during impact scenarios. For a circular (square) tube, a decrease in the diameter will lead to a reduction in the initial peak force. That is why the smaller end of tapered tubes is always placed proximal to the striker.

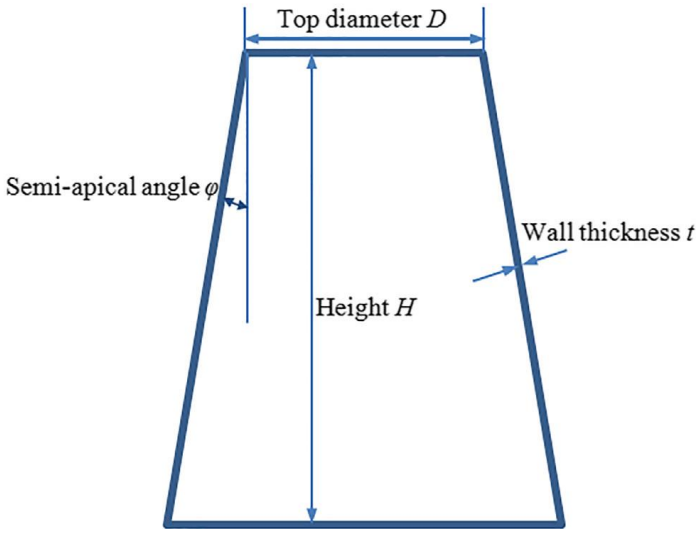

Figure 2.6 *Schematic diagram of a thin-wall frustum (Xu et al. 2018)*

Early studies on axial crushing of tapered tubes were performed by Mamalis and Johnson (1983) in the 1980s. Based on the compression tests of thin-walled cylinders and frusta,

empirical expressions of the mean crushing load were firstly derived for frusta with various semi-apical angles by fitting the results of frusta with various crumpling modes (Mamalis *et al*. 1984). A theoretical model was then proposed to analyse the extensional mode of frusta (Mamalis *et al*. 1986), and the mean force was correlated with the yield stress of material, wall thickness, top diameter and semi-apical angle of the frusta. The effect of end constraints on the energy absorption of frusta was investigated experimentally by Sobky *et al*. (2001). Constraining the frusta at the top was reported to enhance the energy absorption capacity under both static and impact loading.

With the advance of computer technology, numerical simulation have been widely applied in the crashworthiness analysis and design of tapered tubes. For example, Nagel and Thambiratnam (2004; 2005) investigated the energy absorption response of tapered thin-walled rectangular tubes numerically and compared with that of straight tubes. Effects of various factors including wall thickness, taper angle, impact mass and velocity were analysed. Avalle and Chiandussi (2007) introduced a tapered initiator to a tubular component as the front structure or front longitudinal beam of a vehicle body. Results showed that the tapered initiator could reduce the initial peak force and hence lower the maximum acceleration during impact events.

Apart from improving load uniformity, another significant benefit of tapered tubes is to resist oblique loading. In fact, energy-absorbing structures are always subject to oblique or inclined loading in real crashing events. A compression analysis of the responses of straight and tapered rectangular tubes under oblique loading was carried out by Nagel and Thambiratnam

(2006) using a numerical model validated by experiment. The influences of load angle, impact velocity and geometric dimensions were analysed, and tapered tubes were found advantageous in applications where oblique loading is expected. In addition, filling the structure with foam filler is also one of the most commonly-used ways to improve the crashworthiness of thin-walled tubes. The foam filler was found to further improve the performance of tapered tubes (Ahmad *et al*. 2010), especially under oblique loading. Moreover, adopting multi-cell sections is another effective way to substantially increase the capacity of energy absorbing components (Zhang & Zhang, 2013; Zhang *et al*. 2017).

2.3.1.2 Thin-walled structures with graded wall thickness

Thin-walled structures with graded wall thickness also attracted wide attentions in recent years. It is not a new concept to employ variable wall thickness to improve the crashworthiness. In 1993, Chirwa (1993) investigated the plastic collapse of a type of invert buck tube with graded thickness along the longitudinal direction. The energy absorption efficiency was reported to be increased by up to 50%, compared to tubes with constant wall thickness. However, due to the limitations on fabrication, the variation or distribution of the wall thickness was not controlled artificially at that time.

With the advance in material rolling technology, metal plates with continuous thickness changes can be produced without difficulty. As shown in Figure 2.7, tailor rolled blank (TRB) technology is now employed to produce vehicle components with graded thickness and lighter weight. Yang *et al*. (2007) applied TRB for designing frontal energy-absorption structures and Chuang *et al*. (2008) investigated the performance of TRB in vehicle structures.

Based on the design optimization technology, they both reported that the components with graded thickness through TRB technology could achieve comparable performance as traditional design with less structural mass.

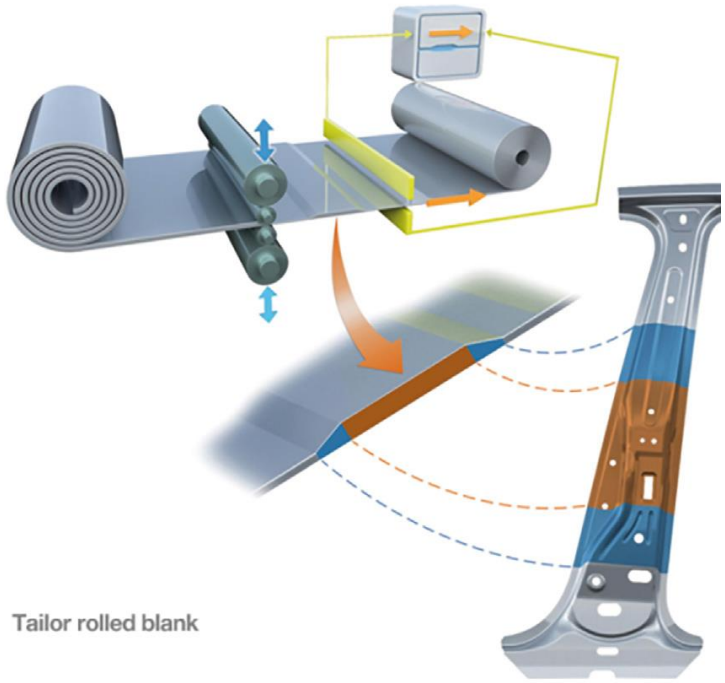

Figure 2.7 *Schematic of tailor rolled blank (TRB) technology (Merklien et al. 2014)*

Thin-walled structures with variable wall thickness can be fabricated by other methods in laboratory. Wire cut electrical discharge machining (WEDM) technique is one effective approach with high accuracy. As shown in Figure 2.8, two types of square tubes with linearly distributed wall thickness along the cross-section, i.e., tubes with single surface gradient (SSG) and double surface gradient (DSG), were fabricated and their axial crush response was investigated by Zhang *et al*. (2014). Square tubes with uniform thickness and the same mass were also tested for comparison. Up to 30%-35% increase in mean force and energy absorption efficiency was achieved without the increase of structural mass and initial peak force. Their work was further extended to the axial crush of multi-cell tubes with variable thickness by Fang *et al*. (2015).

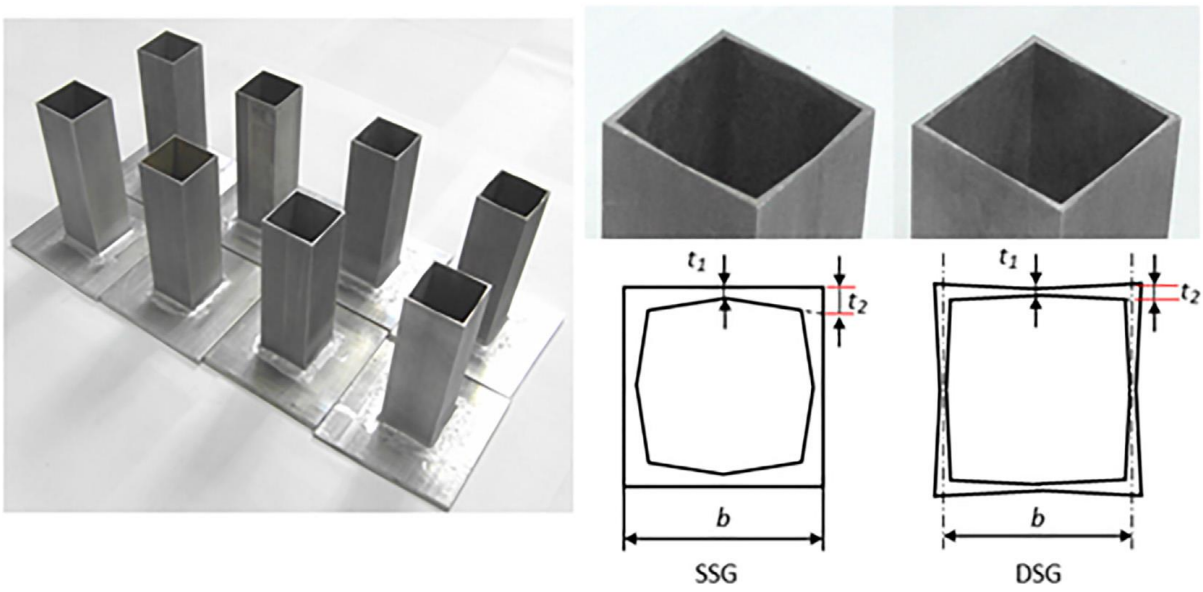

Figure 2.8 *Square tubes with graded thickness along the radial direction (Zhang et al. 2014)*

Numerical analysis and optimization design strategy were also performed to improve the performance of graded structures. For axial crushing of square tubes, thickness gradient in the axial direction was investigated numerically by Sun *et al*. (2014). The performance of tubular structures with graded thickness was superior to counterparts with uniform thickness. They also performed a multi-objective design optimization to achieve high specific energy absorption and low initial peak force. Axially graded thickness was also extended to multi-cell sections by Yin *et al*. (2015) and corresponding optimization design was performed.

2.3.1.3 Thin-walled structures with graded material property

The material property of structures can also show gradient tendency by adopting some advanced fabrication technologies. For example, the tailored hot stamping (THS) process is often used to alter the tensile properties of materials, and thus the energy-absorbing structures with graded strength or variable hardness profile could be obtained (Karbasian &

Tekkaya, 2010; Kranjc et al. 2010). Different strengths can be fabricated through tooling heated up to various temperatures, so that the structures will show different mechanical properties in different regions of the same part. For example, THS is often employed to B-pillars in automotive body to achieve a structure containing a soft zone, a hard zone and a transition zone across its area (Perez-Santiago et al. 2013). Other components, such as A-pillars, side impact protections, frame components, bumpers can also be manufactured by the THS technology. By the combination of forming and hardening, an ideal graded strength property could be tailored for the construction of structural elements and energy-absorbing components in the automotive industry.

George *et al*. (2012) performed crushing tests on a structure with graded material properties and reported that the graded specimen absorbed more energy and displayed better crush efficiency. In summary, the graded material property from THS technology provides another way for engineers and designers to obtain remarkable energy-absorbing structures. Structures with variable strength or hardness profile can be fabricated through hot stamping and cooling to meet the requirements of lightweight and higher energy-absorption capacity.

2.3.2 Cellular materials with graded structures

2.3.2.1 Graded cellular foam

Although metal matrix syntactic foam and metal foam are different types of material in that the former is a composite and the latter is a one phase material, both can be classified as

cellular materials. This section reviews the mechanical properties of graded structure cellular materials, which have some common characteristics with graded metal matrix syntactic foam.

The major merit of graded structure cellular material lies in the fact that the microstructural detail can be spatially varied and graded through a non-uniform distribution of the two phases with different properties, sizes and shapes (Brook, 1995). By varying microscale parameters (density, cell wall and face thickness, area inertia moment, etc.), the local load-bearing capacity becomes a controllable spatial variable rather than an approximately constant value (Yu *et al*. 2007).

Early studies, as described by Gibson and Ashby (1999), have shown that foams can absorb a considerable amount of energy when the stress reaches a roughly constant plateau value. Graded aluminium foam blocks with varying or gradient cross-sections have also been investigated more recently (Shen *et al*. 2015; Gan *et al*. 2016). Significant advances have been made in syntactic foam technology to enable the fabrication of spatial grading of properties of the foams containing microballoons (hollow particles) (Chittineni *et al*. 2010; Gupta, 2007).

Various approaches have been reported to produce and evaluate functionally graded foams using different techniques. He *et al*. (2014) produced uniform and functionally graded closed cell aluminium foams using a specially modified casting technique. Quasi-static compression tests indicated noticeable strain hardening. Dynamic loading of graded foams produced a lower peak stress and a more extended plateau region than uniform foams. Hangai *et al*.

(2016) fabricated a functionally graded foam using a sintering-dissolution technique. During the dissolution step, the removal of the space holder (NaCl) was partially stopped. The resulting graded material was a combination of open-cell Al foam and Al/NaCl composite. In another study (Hangai *et al*. 2011), a functionally graded closed-cell aluminium foam was prepared by the friction stir processing technique, using different amounts of foaming agent in the precursor. The as-produced samples consisted of two layers with different porosities. By tailoring the high and low porosity layers, it was possible to control the deformation mechanism of the functionally graded composite foam. Hassani *et al*. (2012) fabricated a functionally graded open cell aluminium foam using a powder metallurgical method. They used carbamide particles as space holders and changed the particle size in the longitudinal direction of the foam.

MMSFs are a special group of metal foams, which consist of a metal matrix with embedded filler particles (Gupta *et al*. 2015). In most cases, MMSFs are produced by homogeneous distribution of fillers inside the matrix. As a result, MMSFs with uniform physical properties are achieved. To gain the benefits of graded structure, a property gradient can be introduced into syntactic foams by altering the size or volume fraction of particles and/or by employing tailored distributions of two or more different particle types. Ferreira *et al*. (2010) produced a functionally graded aluminium syntactic foam using a centrifugal casting technique. In their study, a changing volume fraction of microballoons was distributed along the radial direction of the cast samples. Majlinger and Orbulov (2014) studied hybrid metal syntactic foams. They embedded random mixtures of two different filler particles, hollow ceramic and hollow iron spheres, inside an aluminium alloy matrix.

2.3.2.2 Graded honeycomb

Graded honeycomb, another widely studied cellular material, is also an effective energy absorption element (Ruan *et al*. 2003). Honeycombs are typical thin-walled structures with periodic cells with different properties in different directions. Gradients can be introduced in wall thickness, cell width or material properties. A variable yielding stress or strain hardening of honeycomb cell wall was introduced as the graded characteristic by Shen *et al*. (2013) and Mousanezhad *et al*. (2014). Different strengths were achieved among the honeycomb cells, which provided a graded feature to control the in-plane crushing collapse.

Honeycombs with variable cell wall thickness were also investigated (Al *et al*. 2008). By varying cell wall thickness along the crushing direction, a thickness-graded in-plane crushing mode was established (Zhang *et al*. 2014). The in-plane dynamic crushing behaviour of graded honeycomb structures with miss-wall defects was also investigated (Fan, 2016). Besides hexagonal honeycombs, dynamic response of the circle-arc honeycombs with density gradients was investigated (Zhang *et al*. 2015). The gradient density of cellular structure was demonstrated to have a remarkable influence on the energy absorption capability.

In summary, cellular materials with graded properties are promising energy absorbing materials. Energy absorption capability can be significantly affected by multiple factors such as density, cell wall thickness, material strength, graded distribution and the number of layers. By appropriate design of these factors, cellular materials can be made to bear much higher loads and absorb more energy.

2.4 Effect of dynamic/impact loading on mechanical properties of syntactic foams

The attention on mechanical behaviour of syntactic foams normally lies in three aspects: strength (peak stress, plateau stress), energy absorption and failure mechanism. Therefore, the effects of dynamic/impact loading can be considered in these aspects. However, these three aspects are interdependent. Generally speaking, high strength leads to high energy absorption but can result in a brittle failure mechanism, while brittle failure in return leads to low energy absorption. In this section, the effects of dynamic/impact loading will therefore be discussed as a whole instead of on each aspect separately, unlike the case with mechanical properties of syntactic foams under quasi-static loading.

2.4.1 Polymeric syntactic foams

Dynamic properties of polymeric syntactic foams have been extensively investigated experimentally. Song *et al*. (2007) investigated the mechanical properties of epoxy syntactic foam at intermediate strain rates using modified split Hopkinson pressure bar (SHPB) and reported that the failure strength exhibited strain-rate dependency. Li *et al*. (2009) conducted compressive tests on glass microballoon syntactic foams using a hydraulic loading machine for medium strain rates and SHPB for high strain rates up to 4000 s^{-1}. The stress-strain response obtained exhibited strain rate dependency. They combined microscopic observations with numerical simulations to study the failure mode and failure mechanism. Ouellet *et al*. (2006) also investigated the compressive properties of polymeric syntactic foams under quasi-static condition and medium and high strain rate conditions using SHPB. They found that the strain rate effects became pronounced at strain rates above 1000 s^{-1}.

Viot *et al*. (2008) examined the properties of syntactic foams under high strain rate loadings. They observed significant effects of microsphere volume fraction, projectile mass and drop height on the energy absorption. The energy absorption mechanism included the visco-plastic deformation of the matrix and the fracture of the glass bubbles. The energy absorption was mainly governed by the failure of the glass bubbles when their volume fraction was high and was primarily controlled by the resin deformation when the volume fraction of glass bubbles was low. Shams *et al*. (2017) developed a micromechanical model to simulate syntactic foams under high strain rate loads. This numerical model was able to predict syntactic foam behaviour at a wide range of strain rates and various microballoon configurations.

2.4.2 Metal matrix syntactic foams

The compressive behaviour of MMSFs, especially aluminium matrix syntactic foams (AMSFs), under dynamic loading has been widely studied. As the present thesis is focused on AMSFs, this section mainly reviews the dynamic properties of AMSFs.

Balch *et al*. (2005) fabricated AMSFs by liquid metal infiltration of commercially pure aluminium and 7075 aluminium alloy. The dynamic compression tests showed about 10-30% increase in peak strength compared to the quasi-static results. Strain rate sensitivity was similar to that of aluminium matrix composite materials. Goel *et al*. (2012) studied the dynamic behaviour of aluminium cenosphere syntactic foams with 30% porosity at higher strain rates (up to 1400/s) and reported that the compressive strength and energy absorption of these foams reached a maximum at a strain rate of approximately 750/s and then decreased with further increasing strain rate. Luong *et al*. (2011) determined the strain rate

dependence of compressive response for A4032 aluminium alloy/hollow fly ash AMSFs. They reported that the AMSFs showed a higher strength and a higher energy absorption capability at a higher strain rate. Santa Maria *et al*. (2014) studied the quasi-static and dynamic mechanical properties of A380-Al_2O_3 AMSFs with six different microsphere sizes and different size ranges. The tests, conducted at strain rates between 880 and 1720 s^{-1}, revealed that the properties of the AMSFs containing hollow spheres with average diameters of 0.425-0.85 and 0.85-1 mm were not strain rate-dependent and, therefore, their performance was similar to that in quasi-static tests. Dou *et al*. (2007) investigated the high strain rate compression behaviour of AMSFs with cenosphere and pure aluminium and compared their performance to that displayed under quasi-static loading conditions. It was found that the foams exhibited distinct strain rate sensitivity and that the peak strengths increased by about 50% and the energy absorption capacity increased by about 50-70%. Goel *et al*. (2012; 2013; 2014) studied the compression behaviour of AMSFs with cenosphere at strain rates ranging from quasi-static conditions to 1400 s^{-1}. The compressive strength and energy absorption of the foams attained a maximum at a strain rate of approximately 750 s^{-1}, and then decreased as the strain rate increased. It was also found that the foam with coarser cenospheres appeared to be more strain rate sensitive. Feidler *et al*. (2015) conducted a dynamic analysis of low cost AMSFs with expanded perlite under dynamic compressive loading conditions. The yield stress was found to increase slightly at higher strain rates, indicating positive strain-rate sensitivity. The perlite particles had a positive effect on the compression resistance at high strain rates. Cox *et al*. (2014) studied the dynamic behaviour of AMSFs with A356 alloy and SiC particles at strain rates up to 1520 s^{-1}. They found that the hollow spheres were crushed at the end of the elastic region and failure of the AMSFs at high strain rates was initiated by particle cracking and shear band formation.

The effects of low strain rate dynamic loading have also been investigated. Park *et al*. (2002) studied the mechanical properties of steel syntactic foams at strain rates 4.5 x 10^{-5} s^{-1} to 16 s^{-1}. Their results showed that the energy absorption increased linearly with strain rate. The yield strength of the samples showed stronger strain rate dependence at higher strain rates. Mondal *et al*. (2009) assessed the deformation response and energy absorption characteristics of closed cell aluminium-fly ash particle composite foams at different strain rates (from 10^{-2} to 10^{1} s^{-1}). The influence of strain rate on the deformation response was found to be very marginal; the strain rate sensitivity was measured to be very low (0.02-0.04) when the foam relative density was greater than 0.1 and was found to be negative when the foam relative density was less than 0.1.

In summary, dynamic loading, i.e. high strain rate, leads to higher stress and higher energy absorption capacity than quasi-static loading. At low strain rates (around 10 s^{-1}), strain rate sensitivity is negative. At higher strain rates (around 1000 s^{-1}), strain rate sensitivity causes significant increases in strength and energy absorption (10%-70%). When the strain rate is greater than a certain value, the strength and energy absorption no longer increase.

2.4.3 Theoretical analysis of impact loading

For decades, many efforts have been made to theoretically explain the material behaviour under impact loading. Generally speaking, the theoretical models for impact loading are based on the propagation of impact wave in one-dimensional formulation. There are two approaches in these models: non-linear wave theory or linear wave theory with simplified

stress-strain curve. This section reviews the development, advantages and disadvantages of both approaches.

Any material with a stress-strain curve which is monotonically increasing and is convex to the strain axis tends to form impact wave under impact loading (Reid *et al.* 1997). Jahsman (1968) used one-dimensional non-linear wave theory to model the behaviour of syntactic foams under high velocity dynamic compression. His model includes a precursor elastic wave and a centred fan of inelastic waves preceding the impact front. Similarly, Zaretsky and Ben-Dor (1995) derived impact equations based on more complex experimental or theoretical stress-strain relationships for the material to produce Hugoniot relationships for polymeric foams. Recently, Karagiozova *et al*. (2010, 2012, 2015) proposed an approach to study the compaction of cellular materials with uniform density exhibiting strain hardening. It was based on one-dimensional stress wave propagation and used actual experimentally-derived stress-strain curves together with their Hugoniot strain velocity representation. The densification strain was not assumed in advance but obtained as part of the solution. This model was verified by numerical simulations under various loading conditions. Similarly, Rostilov *et al*. (2021) also used Hugoniot condition to describe shocked states behind the wave front and demonstrated the two-wave configuration of stress-evolution in syntactic foam under impact.

The mathematical equations used to describe the constitutive relationships in non-linear wave theory can only be solved numerically. Non-linear wave theory also causes problems in certain systems like ring systems (Reid *et al*. 1983). A first order approximation was then

produced by Johnson (1972) with an idealized material model of linear strain hardening. This approach retained the two key features of the stress-strain curves, a yield strength and a densification strain as these two basic parameters can be simply defined from experimental results. This model provides an analytical expression for the crushing stress under impact loading and gives a good physical feel for the effect of various parameters on the impact process. For example, stress fluctuation was observed experimentally by Rousseau *et al*. (2017). Johnson's theory can demonstrate that propagation of impact waves leads to stress fluctuation in a specimen, resulting in higher stress at the end of specimen than in the middle. Recently, Pham *et al*. (2018) used Johnson's theory to explain the failure mechanism in syntactic foam under impact loading.

Other models were also used to simplify the material's behaviour. Cellular material was idealised as a perfectly-plastic rigid material in Reid's work (1997), assuming a constant plateau stress up to the predefined densification strain. This approach was further extended to linear hardening by Zheng *et al*. (2012). Tan *et al*. (2005a, 2005b) proposed a model taking into account the elastic material properties. Harrigan *et al*. (2005) used an elastic-plastic model with hardening, while Lopatnikov *et al*. (2004) developed an elastic-perfectly-plastic rigid model.

Take Reid's (1997) approach for example, material was assumed to be rigid, perfectly-plastic, locking (RPPL). Fig. 2.9 (i) shows a wooden cylinder of initial length $L_{0\mathrm{R}}$, cross-sectional area $A_{0\mathrm{R}}$ and density $\rho_{0\mathrm{R}}$ with an attached mass M_R striking a rigid target normally with an impact velocity v_{0R}. The wood is assumed to deform under uniaxial compressive strain conditions. When impact occurs an impact wave is initiated which propagates along the cylinder. Because

of the rigid nature of the initial response, the stress in all material ahead of the shock is instantaneously raised to σ_{crR}. As it passes through the material it brings it to rest, increases its density by compaction up to the locking strain ε_{1R} and raises the stress to σ_R^*. Fig. 2.9 (ii) shows the state of the system at time t_R when the shock has advanced a distant x_R from the contact surface. The shaded region ahead of the shock front denotes the material which is traversed by the shock in time δt_R. It is shown in its crushed state in Fig. 2.9 (iii). The equations governing the propagation of the shock are made up of kinematic equations and equations of conservation of mass and momentum for material crossing the shock front.

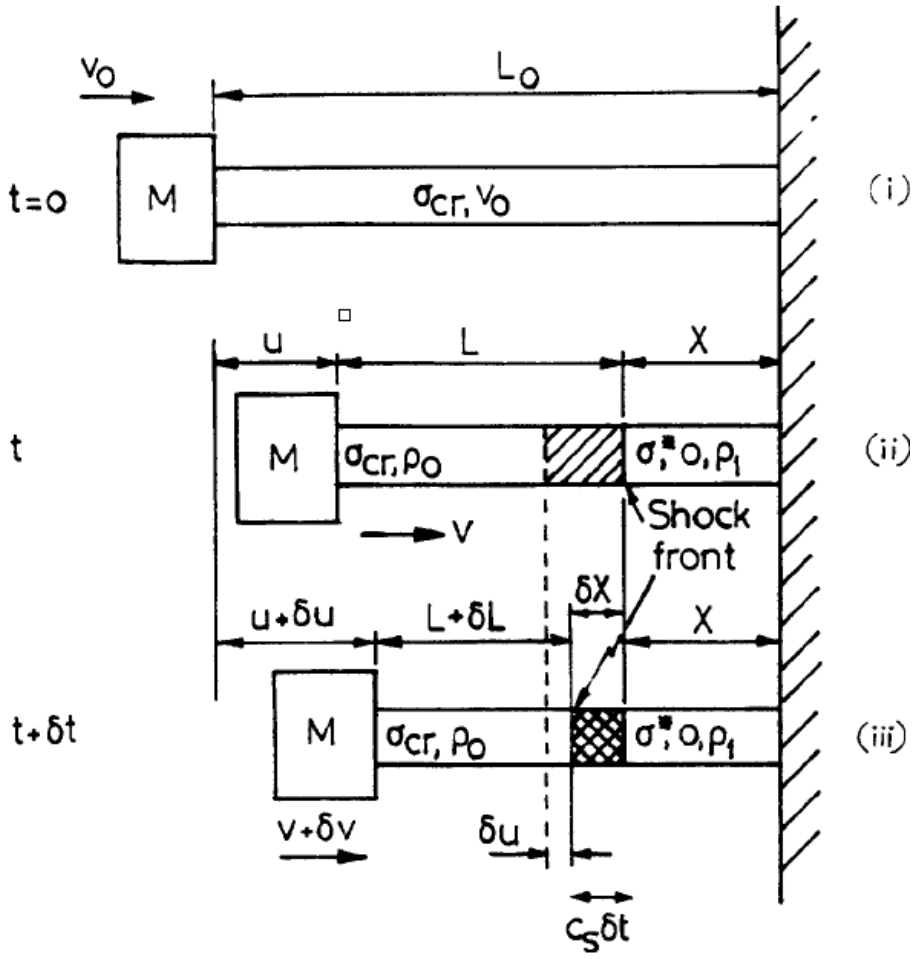

Figure 2.9 *Shock propagation model for RPPL material (Reid & Peng, 1997)*

If u_R is the displacement of the rigid mass at time t_R, the from Fig. 2.9, x_{0R}, the un-deformed length of the crushed portion is given by

$$x_{0R} = u_R + x_R \tag{2.1}$$

Where x_R is the deformed length of crushed wood.

From Fig. 2.9 we also have

$$u_R + x_R + L_R = L_{0R} \tag{2.2a}$$

and so

$$\dot{L_R} = -(\dot{x_R} + \dot{u_R}) \tag{2.2b}$$

Where superposed dots denote differentiation with respect to time and $\dot{u_R}$ =du_R/dt_R = $v_R$is the current velocity of the rigid mass and the un-deformed portion of the wood.

Assuming that no radial expansion occurs, conservation of mass gives,

$$\rho_{1R} A_{0R} x_R = \rho_{0R} A_{0R} (u_R + x_R) \tag{2.3}$$

Where ρ_{0R} is the initial density and $\rho_{1R}$is the density when fully crushed. Thus

$$\gamma_R = \frac{\rho_{0R}}{\rho_{1R}} = \frac{x_R}{u_R + x_R} \tag{2.4}$$

By definition,

$$\varepsilon_{1R} = \frac{x_{0R} - x_R}{x_{0R}} = \frac{u_R}{u_R + x_R} \tag{2.5}$$

Thus,

$$\gamma_R = 1 - \varepsilon_{1R} \tag{2.6}$$

Rearranging Eq. (2.4) gives

$$x_R = \frac{\gamma_R u_R}{1 - \gamma_R} = \frac{1 - \varepsilon_{1R}}{\varepsilon_{1R}} u_R \tag{2.7}$$

The shock speed relative to the projectile, c_{sR} is equal to dx/dt. Thus from Eq. (2.7),

$$c_{sR} = \frac{\gamma_R}{1 - \gamma_R} \dot{u_R} = \frac{\gamma_R}{\gamma_R} v_R \tag{2.8}$$

This indicates that the shock speed reduces as the un-deformed portion of the projectile is slowed down. The mass δm_R of the shaded element of length $\delta x_R = c_{sR} \delta t_R$ is given by

$$\delta x_R = \rho_{1R} A_{0R} c_{sR} \delta t_R = \frac{\rho_{0R} A_{0R} c_{sR} \delta t_R}{\gamma_R}$$

From Eq. (2.4)

Conservation of momentum for this element of mass gives

$$A_{0R}(\sigma_R^* - \sigma_{crR})\delta t_R = \frac{\rho_{0R} A_{0R} c_{sR} v_R \delta t_R}{\gamma_R}$$

Or

$$\sigma_R^* = \sigma_{crR} + \frac{\rho_{0R} c_{sR} v_R}{\gamma_R}$$

Thus

$$\sigma_R^* = \sigma_{crR} + \frac{\rho_{0R} {v_R}^2}{\varepsilon_{1R}} \tag{2.9}$$

In summary, both the non-linear and the simplified approaches are based on the propagation of impact waves. Johnson's theory has simpler mathematical expressions while captures the key features of stress evolution in impact loading. Theoretical analysis in this work is based on Johnson's theory.

2.4.4 Impact ductility

Syntactic foam is designed as impact protection material. It requires not only energy absorption capacity to absorb the impact energy, but also ductility to keep structure integrity during impact. Crack/fracture could be harmful from engineering perspective. Generally, strong material has high energy absorption but low ductility, and material under impact loading has even lower ductility than that of static loading. Therefore, an ideal syntactic foam should have a good match between energy absorption and ductility to ensure a good performance.

However, most studies nowadays are focused on the energy absorption capacity, e.g. specific energy absorption (Broxtermann *et al.* 2018), energy absorption efficiency (Zhang *et al.* 2016). Although fracture strain is mentioned in some researches (Orbulov *et al.* 2014; Myers *et al.* 2015), and fracture mode is also mentioned in some works (Gupta *et al.* 2006; Omar *et al.* 2015; Movahedi et al. 2019). Few has studied the match between energy absorption capacity and ductility. As a result, there is no widely recognized way in studying impact ductility of syntactic foam so far.

This work proposes a way to study impact ductility by judging if the syntactic foam has sufficient ductility to fulfil its energy absorption capacity, i.e. whether it cracks apart or not before densification.

Chapter 3 Experimental Procedure

This chapter presents a detailed description of the raw materials, fabrication processes, density measurement, microstructural observations and mechanical testing procedures for the Al syntactic foam samples with both uniform and layered structures.

3.1 Raw materials

The raw materials used for fabricating the Al matrix syntactic foam samples were an Al 6082 alloy, in the form of a block, and a ceramic microsphere (CM) powder. The Al alloy had a chemical composition of 1.3% Si, 0.5% Fe, 0.4% Mn, 0.8% Mg, by weight, and balance for Al. The CM powder used in this study was supplied by Envirospheres Pty Ltd Australia. The CM powder had a composition of ~60% SiO_2, ~40% Al_2O_3 and 0.4-0.5% Fe_2O_3 by weight, and had an effective density of 0.66 g/cm^3. The effective density is the mass of the powder divided by the volume of the powder less the air voids between the microspheres. The as-received CM powder was divided into three size groups with diameter ranges of 70-125 μm, 125-250 μm and 250-500 μm, which were designated as CM Powder S, M and L, respectively, and are shown in Figure 3.1. The majority of the particles in CM powders M and S have a regular spherical shape, a smooth shining surface and a hollow inner structure. The majority of the particles in CM powder L have a quasi-spherical shape, a coarse surface and a porous inner structure.

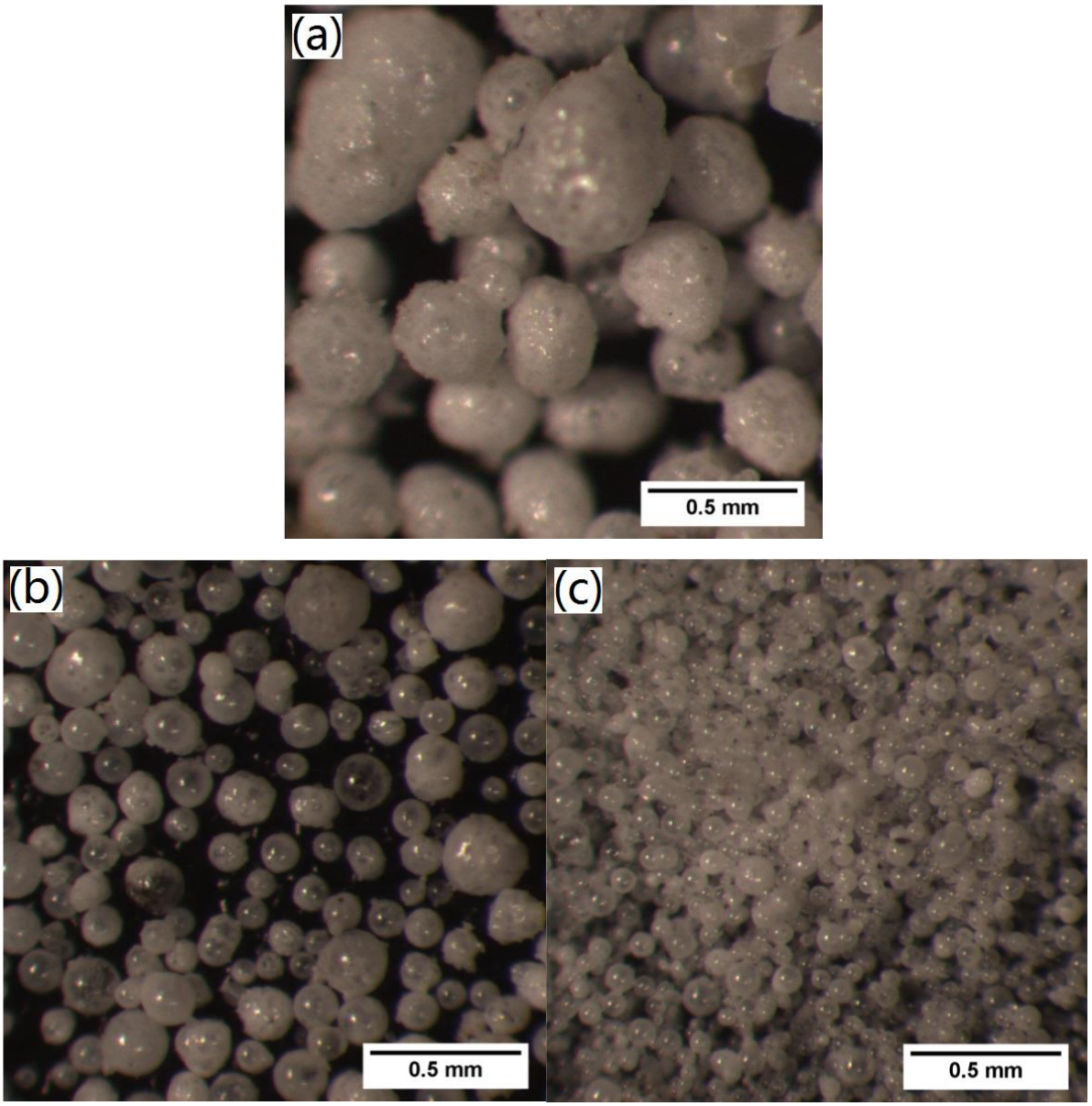

Figure 3.1 *Optical images of the three types of ceramic mircospheres (a) L, 250-500 μm, (b) M, 125-250 μm and (c) S, 70-125 μm*

3.2 Melt infiltration casting method

The Al syntactic foams were produced by melt infiltration casting, as shown in Fig. 3.2. Uniform syntactic foam samples were fabricated by infiltrating molten Al into monomodal (single particle size range) CMs. Graded syntactic foam samples were fabricated by infiltrating molten Al into multimodal (two or three particle size ranges) CMs. All AMSF samples have

nominal dimensions of 15 mm × 15 mm × 15 mm for quasi-static compression tests and 10 mm × 10 mm × 15 mm for impact tests.

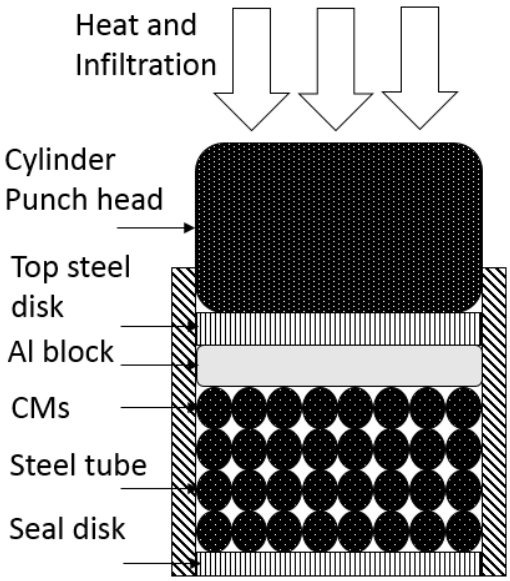

Figure 3.2 *Schematic diagram of melt infiltration casting*

Before infiltration, a steel tube, sealed by a circular steel disc at bottom, was filled with the CM powder or powders. The diameter of the tube was 50 mm and the length was 50 mm. The total mass of the CM powder(s) contained in the tube was 16.5 g. An Al alloy block of 40 g was then placed on top of the CM powder(s). The volume ratio of Al to CM was maintained at 1:2, at which the Al is slightly more than the amount needed to ensure full infiltration of the CM powder. Another circular steel disc, which was slightly smaller than the internal diameter of the tube, was placed above the Al block. The assembly was heated to 755°C and maintained for 30 minutes in an electric furnace to ensure that the Al block was fully molten. The assembly was then moved to a hydraulic machine where the molten Al alloy was compressed into the voids among the CM particles by a piston. After complete solidification, the resultant AMSF sample was removed from the steel tube and ground into cuboid specimens.

3.2.1 Uniform syntactic foam

A uniform syntactic foam sample is shown schematically in Figure 3.3. The uniform AMSF samples are designated as L, M and S, according to the CM powder used. All the samples have a density approximately 1.6 g/cm^3, containing 55% CM particles. The details of composition and structure of the uniform syntactic foam samples are listed in Table 3.1.

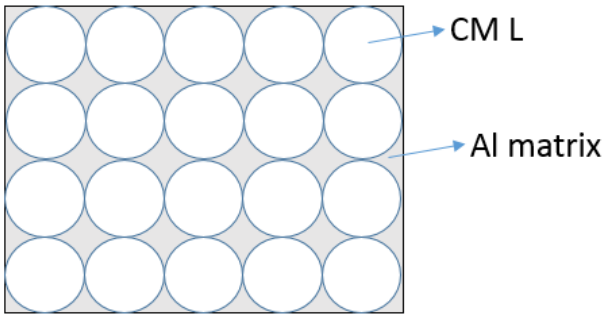

Figure 3.3 *Schematic diagram of uniform AMSF*

Table 3.1 *Composition and structure of uniform syntactic foam samples*

Sample	CM type and volume percentage	Layer structure order and relative thickness of each layer
U1	100% L	L (100%)
U2	100% M	M (100%)
U3	100% S	S (100%)

3.2.2 Layered syntactic foam

Layered syntactic foam samples are shown schematically in Figure 3.4. Four sets of layered AMSFs were fabricated with two, three, four and five layers of CM, either using all three types of CMs (L, M, S) or using any two of the three types of CMs. In manufacturing a layered structure sample, different types of CM were placed in the steel tube layer by layer before infiltration with predetermined order and mass. The different types of CMs contained in the sample had equal masses, with the total mass of CMs maintained at 16.5 g. Each type of CMs

was either kept in one layer or split into two or three separate layers, resulting in two, three, four or five layers in the final sample. The details of composition and structure of the layered syntactic foam samples are listed in Table 3.2.

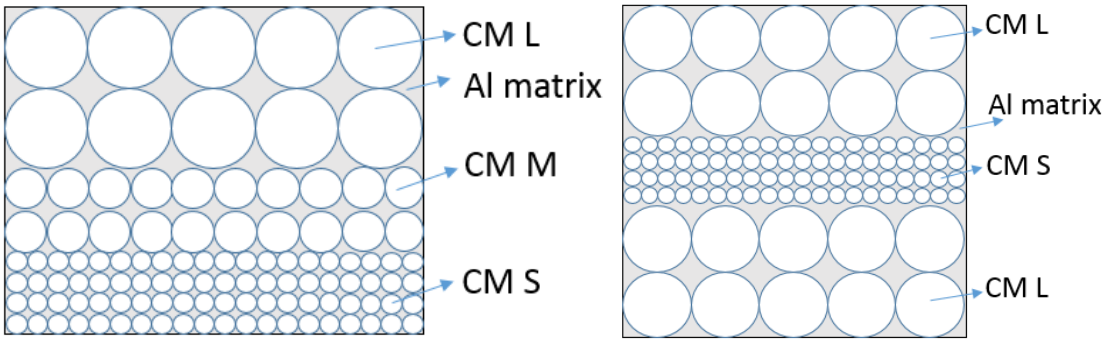

Figure 3.4 *Schematic diagrams of triple (left) and double (right) layered AMSFs*

Table 3.2 *Composition and structure of layered syntactic foams*

Sample	CM type and volume percentage	Layer structure order and relative thickness of each layer
T1	33% L, 33% M, 33% S	L-M-S (33%-33%-33%)
T2	33% L, 33% M, 33% S	M-L-S (33%-33%-33%)
T3	33% L, 33% M, 33% S	L-S-M (33%-33%-33%)
D1	50% L, 50% S	L-S (50%-50%)
D2	50% L, 50% S	L-S-L (25%-50%-25%)
D3	50% L, 50% S	S-L-S (25%-50%-25%)
D4	50% L, 50% S	L-S-L-S (25%-25%-25%-25%)
D5	50% L, 50% S	L-S-L-S-L (17%-25%-17%-25%-17%)
D6	50% L, 50% S	S-L-S-L-S (17%-25%-17%-25%-17%)

3.2.3 Mixed syntactic foam

Syntactic foam samples with mixed-powder structure are shown schematically in Figure 3.5. Three types of fully mixed samples were manufactured by mixing CM powders L (250-500 um) and S (70-125 um) at three different ratios. Three types of partly mixed samples were

manufactured by alternating single powder (L or S) layers with mixed powder (L and S) layers, while maintaining a fixed total ratio of 1:1 between powders L and S. The details of composition and structure of the mixed syntactic foam samples are listed in Table 3.3.

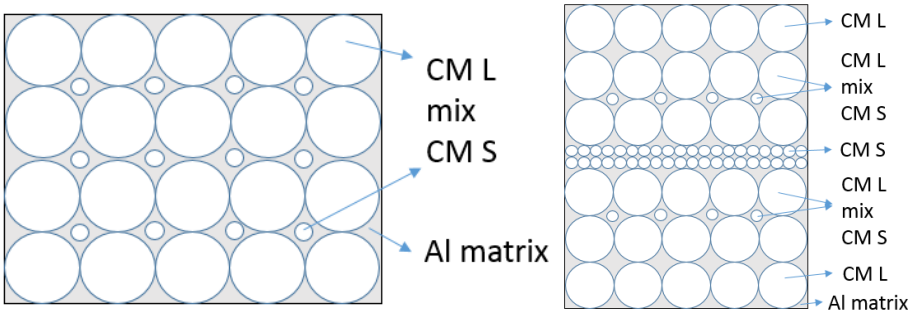

Figure 3.5 *Schematic diagrams of fully-mixed (left) and partly-mixed (right) AMSFs*

Table 3.3 *Composition and structure of fully-mixed and partly-mixed syntactic foams*

Sample	CM type and volume percentage	Layer structure order and relative thickness of each layer
M1	25% L, 75% S	25% L/75% S (100%)
M2	50% L, 50% S	50% L/50% S (100%)
M3	75% L, 25% S	75% L/25% S (100%)
P1	50% L, 50% S	L - 25%L/75%S - S -25% L/75% S - L (20%-20%-20%-20%-20%)
P2	50% L, 50% S	L - 50%L/50%S - S - 50%L/50%S - L (12.5%-25%-25%-25%-12.5%)
P3	50% L, 50% S	75% L/25% S - S - 75% L/25% S (33%-33%-33%)

3.3 Measurement of density

The density of the as fabricated syntactic foam samples was measured by the Archimedes method using water as the working medium. The density of the three CM powders, L, M and S, was also measured by the Archimedes method. As the CM particles have a lower density than water and are also subject to water penetration, a small amount of pure wax was used

to achieve more accuracy. The wax was first placed in a glass container, melted and then cooled to full solidification. The volume of the wax together with the glass container was measured by the Archimedes method in water. The wax was then re-melted at 80°C without any evaporation. An amount of the CM powder was weighed, poured into the liquid wax, gently stirred with a steel wire to eliminate any air bubbles and then allowed to cool to room temperature and solidify. After complete solidification, the total volume of the wax, CM powder and glass container was measured again by the Archimedes method. The volume of the CM powder was the difference between the two measurements. The density of the CM powder was determined using the measured values of its weight and volume.

3.4 Microstructural observation

The syntactic foam samples were ground by metallographic sandpaper with different grit sizes from 120 to 600, and then polished with silk on a polishing machine for optical microscopy. A Nikon optical microscope was used to observe the distribution of CM particles and the bonding condition with the Al matrix in the AMSFs.

3.5 Mechanical tests

Compressive and impact tests were performed on all the uniform, layered and mixed syntactic foams. At least three samples were tested for each type of syntactic foam to verify the repeatability.

3.5.1 Quasi-static compression test

Uniaxial quasi-static compression tests were carried out on an Instron 4045 machine. The samples were cubic with the approximate dimensions 15 mm x 15 mm x 15 mm, with errors less than 10%. Each sample was tested with a cross head speed around 0.9 mm/min to a strain rate of 0.001 s^{-1}. The load-displacement history was recorded. The stress was calculated by dividing the applied load by the original cross-sectional area of the sample; the strain was calculated by dividing the displacement by the original length of the sample. The stress-strain curve was then obtained.

3.5.2 Low speed drop weight impact test

Drop weight impact tests were conducted using an instrumented drop weight impact tower as shown in Fig. 3.6. The vertical guides of the impact tower were lubricated to minimize any friction generated during the descent of the carriage. The samples were manufactured manually. They were rectangular parallelepipeds with the approximate dimensions 15 mm x 10 mm x 10 mm, with errors less than 20%. In each test, the sample was placed at the base and the drop weight was released from a pre-determined height to achieve a pre-determined kinetic impact energy. One of four drop weights, 10 kg, 12 kg, 15 kg and 20 kg, was used, depending on the type of the syntactic foam. The impact velocity was varied from 1.7 m/s to 5 m/s by adjusting the height of drop weight accordingly, to achieve a kinetic impact energy varying from 22 J to 150 J, depending on the type of the syntactic foam. The impact test conditions for all the syntactic foam samples are summarised in Table 3.4. The instant impact force-time data was recorded by a Kistler 9061A piezo-electric load-cell with a maximum capacity of 200 kN. The impactor velocity and displacement as a function of time were measured by a MotionPro-X4 high-speed camera. Images were captured with a time interval

of 0.2 ms. ProAnalyst software was used to analyse the motion of drop weight and to obtain displacement-time and velocity-time data.

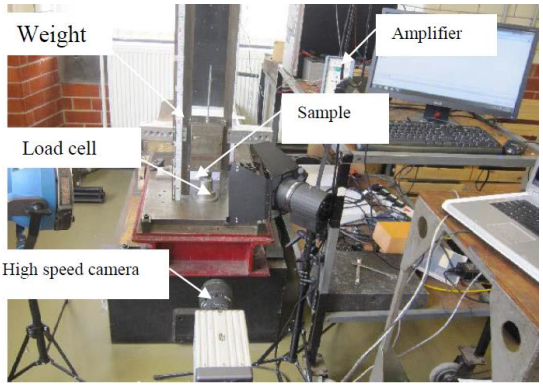

Figure 3.6 *Drop weight test facility*

Table 3.4 *Impact test conditions*

Sample	Impact mass (kg)	Impact velocity (m/s)	Strain rate (/s)	Impact energy (J)
U1	10	3.6	240	65
	12	4	267	96
		4.4	293	116
		5	333	150
	15	3.3	220	82
		3.5	233	92
		3.7	247	103
		4	267	120
		4.3	287	139
	20	2	133	40
U2	10	4.6	307	105
	12	3.8	253	86
		4.2	280	106
		4.6	307	127
	15	3.2	213	77
U3	10	4.5	300	101
	12	3.9	260	91
		4.3	287	110
		4.8	320	138
	15	1.7	113	22
		2.4	160	43
		2.9	196	63
		3.3	220	82
	20	1.5	100	23

(To be continued)

Sample	Impact mass (kg)	Impact velocity (m/s)	Strain rate (/s)	Impact energy (J)
T1-up	10	4	267	80
	12	3.5	233	73
		3.9	260	91
		4.3	287	111
	15	2.2	147	36
		3.3	220	82
		3.7	247	103
		4	267	120
		4.3	287	139
	20	2.6	173	68
T1-down	15	3.3	220	82
		3.7	247	103
		4	267	120
		4.3	287	139
T2	10	3.5	233	62
	12	3.9	260	91
		4.2	280	106
		4.6	307	127
	15	3.7	247	103
	20	2.8	187	78
T3	10	3.8	253	72
	12	3.4	227	69
		3.6	240	78
		3.8	253	87
	15	2.8	187	59
	20	2.1	140	40
D1	10	4.3	287	92
	12	3.6	240	78
		4.2	280	106
		4.5	300	122
	15	3.1	207	72
		3.3	220	82
		3.7	247	103
		4	267	120
		4.3	287	139
	20	2.5	167	63
D2	15	2.9	193	63
		3.3	220	82
		3.7	247	103
		4	267	120

(To be continued)

Sample	Impact mass (kg)	Impact velocity (m/s)	Strain rate (/s)	Impact energy (J)
D3	15	2.9	193	63
		3.3	220	82
		3.7	247	103
		4	267	120
D4	15	2.9	193	63
		3.3	220	82
		3.7	247	103
		4	267	120
D5	15	2.9	193	63
		3.3	220	82
		3.7	247	103
		4	267	120
D6	15	3.3	220	82
		3.7	247	103
		4	267	120
		4.3	287	139
M1	15	2.4	160	43
		2.9	193	63
		3.3	220	82
		3.7	247	103
M2	15	1.7	113	22
		2.4	160	43
		2.9	193	63
		3.3	220	82
M3	15	1.7	113	22
		2.4	160	43
		2.9	193	63
		3.3	220	82
P1	15	1.7	113	22
		2.4	160	43
		2.9	193	63
		3.3	220	82
P2	15	2.4	160	43
		2.9	193	63
		3.3	220	82
		3.7	247	103
P3	15	2.4	160	43
		2.9	193	63
		3.3	220	82
		3.7	247	103

Chapter 4 Experimental Results

4.1 Structural characteristics of AMSFs

4.1.1 Microstructure of AMSFs

Fig 4.1 shows typical AMSF specimens with one, two or three layers. In the uniform AMSF specimens, the CMs are well distributed in the Al matrix (Fig. 4.1a). The specimen with CM L (left) has the largest pores and the specimen with CM S (right) has the smallest pores. In the two-layer AMSF specimens (Fig. 4.1b), there is a clear straight boundary between the two layers with equal thickness. In the three-layer AMSF specimens, the layers also have an equal thickness and the boundaries are clear and straight.

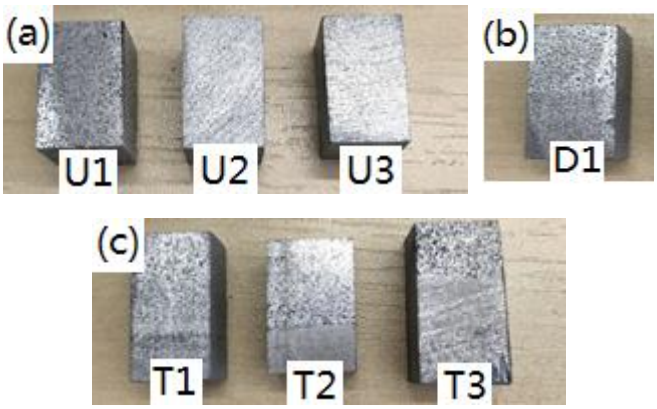

Figure 4.1 *Typical AMSF specimens with (a) uniform, (b) two layer and (c) three layer structures*

Figure 4.2 shows the micrographs of the layered AMSFs with the three types of CM layer boundaries, L-M, M-S and L-S. It is shown that the CMs are distributed randomly in the Al 6082 matrix in all cases, resulting in a homogeneous macroscopic structure. While most CMs in the syntactic foam samples were intact during fabrication, a small number of CMs are infiltrated with molten Al 6082. It seems porous CMs are more defective because of their thin

surface membranes and therefore more apt to be invaded by molten Al under pressure during the melt infiltration process. As consequence, layers with CM L have infiltrated CMs than layers with CM M and CM S. M-S and L-S boundaries are distinctive, with few CMs distributed across the boundary. The L-M boundary is wider than those of M-S and L-S, as the differences in size between some L spheres and M spheres are small.

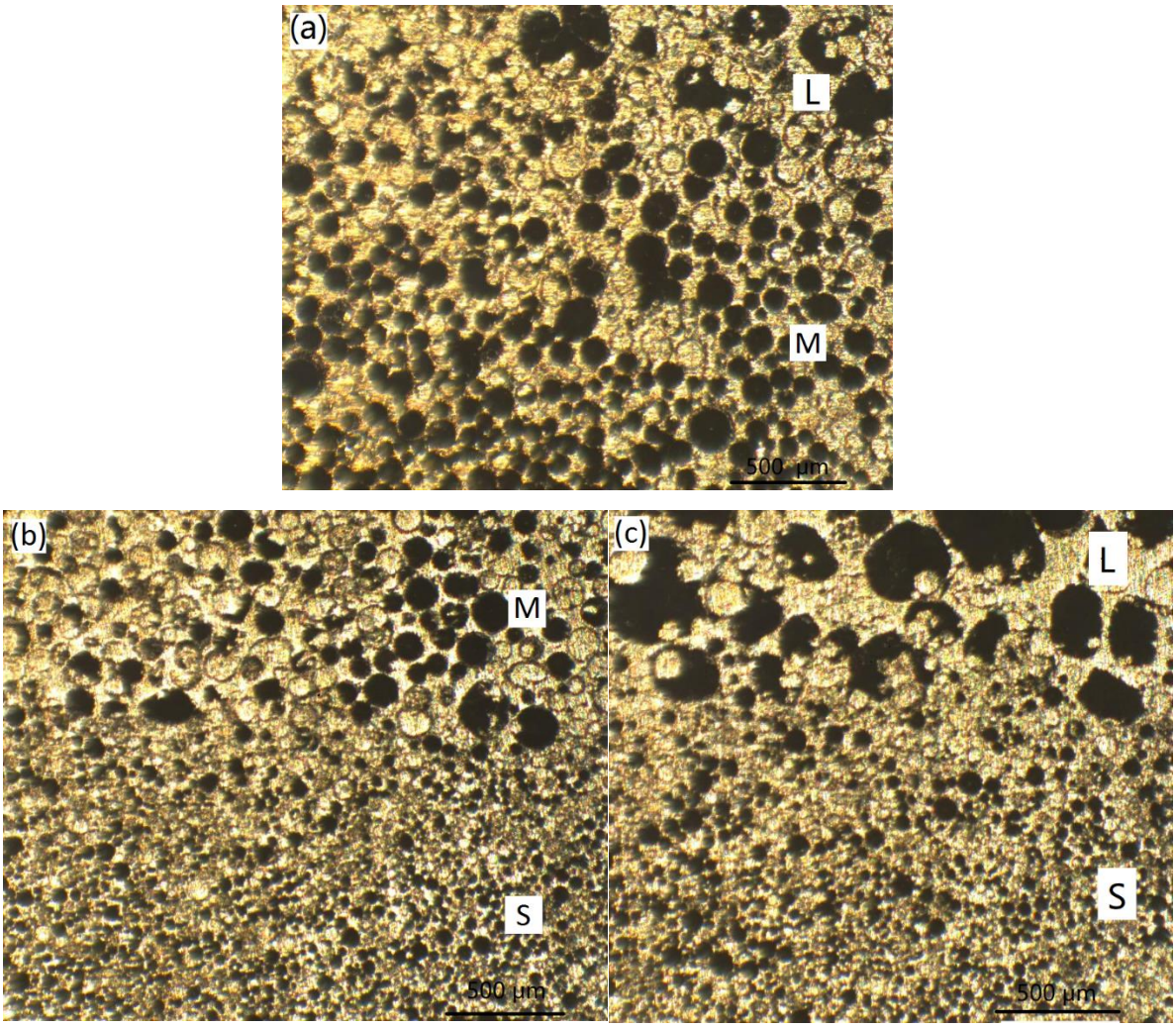

Figure 4.2 *Optical micrographs of layered AMSFs (a) L-M, (b) M-S, (c) L-S, showing layer boundaries*

4.1.2 Density and porosity of AMSFs

4.1.2.1 Density and porosity of uniform syntactic foams

Figure 4.3 shows the average densities and average porosities of the three types of uniform syntactic foams U1 (L), U2 (M), U3 (S) fabricated by melt infiltration, containing monomodal CMs L, M and S, respectively. The average value for each foam was calculated by testing four samples. The syntactic foams containing CM M have a slightly higher density than those containing CMs L and S. The densities of these syntactic foam samples fall in a range of 1.4-1.6 g/cm^3. Given that the theoretical volume percentage of the CMs in a free packed monomodal CM powder is 63% (Hartmann, 1999), the theoretical density of the syntactic foam is calculated to be 1.42 g/cm^3. The experimental density values are slightly higher than the theoretical value, mainly because a small number of CMs were infiltrated with Al.

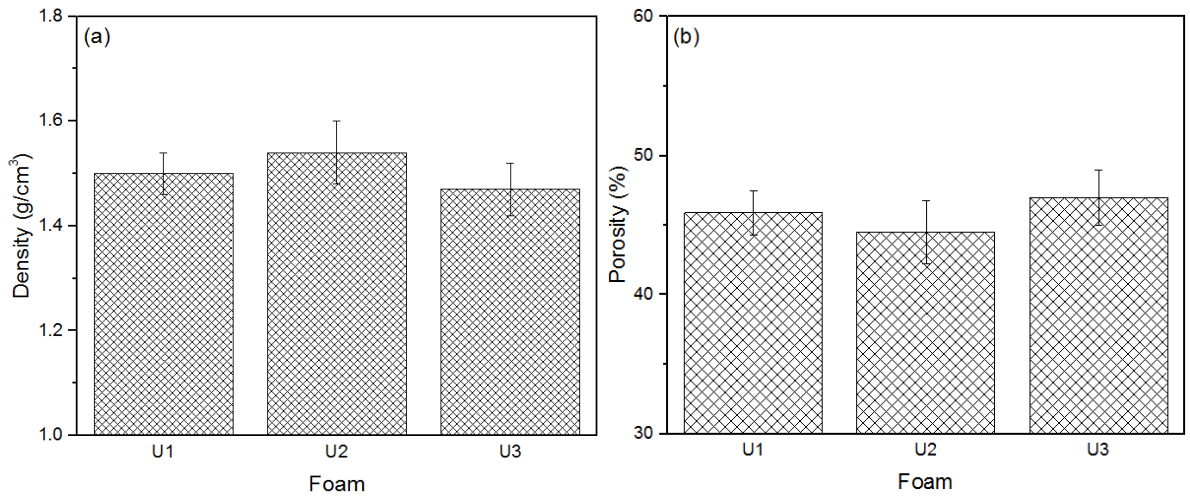

Figure 4.3 *Densities (a) and porosities (b) of uniform syntactic foams*

The porosities of the AMSFs were estimated from the measured densities of the foam specimens and CMs. The basis for the estimation is described as follows. The density of the AMSF specimen is determined by the density of the matrix, and the density and volume fraction of the CMs:

$$\rho_f = \rho_m(1 - f_{CM}) + \rho_e f_{CM} \tag{4.1}$$

where ρ_f is the density of AMSF specimen, ρ_m is the density of the Al matrix, ρ_e is the effective density of the CM and f_{CM} is the volume fraction of the CM. The volume fraction of the CM is therefore:

$$f_{CM} = \frac{\rho_m - \rho}{\rho_m - \rho_e} \tag{4.2}$$

The porosity in the CMs is determined by the density of the CMs and the density of the CM shell, i.e. the solid part of the CM spheres (Zhang and Zhao 2007), by:

$$P_v = (1 - \frac{\rho_e}{\rho_s}) \tag{4.3}$$

where P_v is the porosity in the CM powder, ρ_e is the density of the CM spheres, and ρ_s is the density of the CM shell.

Therefore, the porosity of the AMSF specimen is:

$$\varphi = f_{CM} P_v = \frac{\rho_m - \rho_f}{\rho_m - \rho_e} (1 - \frac{\rho_e}{\rho_s}) \tag{4.4}$$

4.1.2.2 Density and porosity of layered syntactic foams

The densities and porosities of the double-CM syntactic foams, D1-D6, are presented in Figure 4.4. The density of the double-CM syntactic foams is in the range of 1.44-1.64 g/cm^3 and the porosity is in the range of 40.5%-48.2%. Double-CM syntactic foams have slightly higher average densities than uniform syntactic foams, and consequently lower average porosities.

The densities and porosities of the triple-CM layered syntactic foams, T1-T3, are shown in Figure 4.5. The triple-CM syntactic foams have a greater density range of 1.50-1.63 g/cm^3,

with the porosities between 40.8% and 46%. The average densities of the triple-CM syntactic foams T1, T2 and T3 are 1.58, 1.55 and 1.56 g/cm^3, respectively. The corresponding average porosities are 42.8%, 44% and 43.6%, respectively. The average densities are slightly higher than those of the uniform foams.

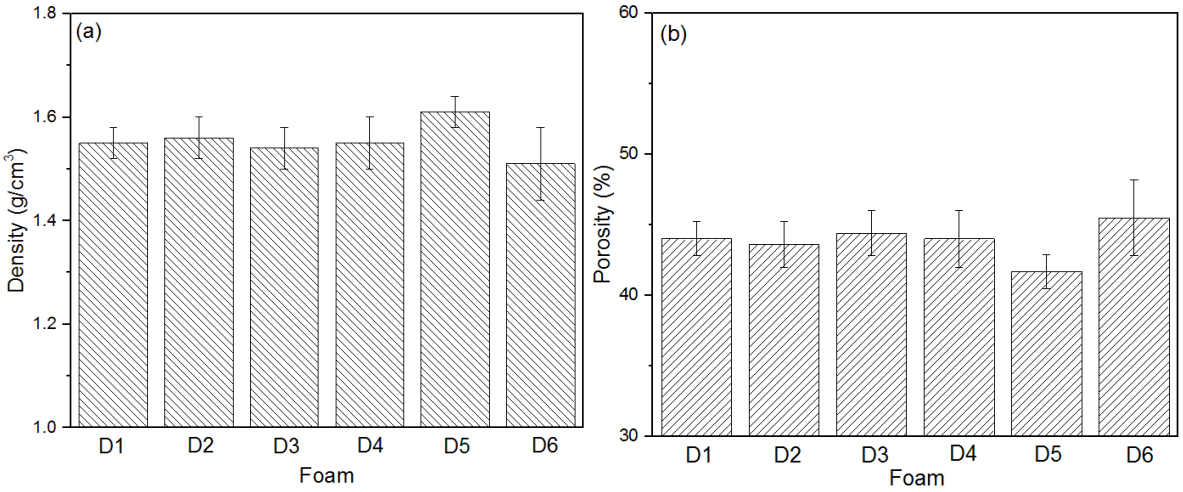

Figure 4.4 *Densities (a) and porosities (b) of double-CM layered syntactic foams*

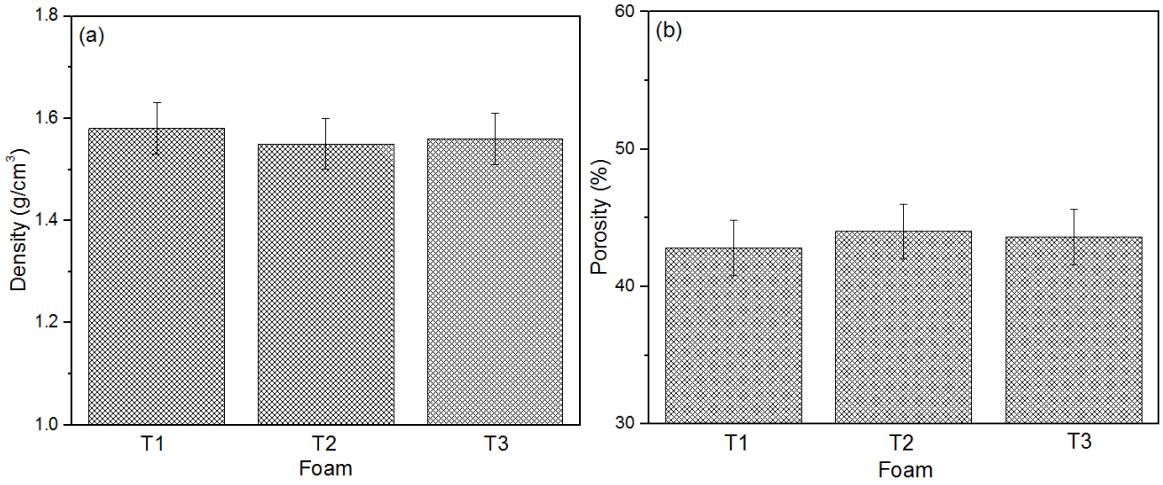

Figure 4.5 *Densities (a) and porosities (b) of triple-CM layered syntactic foams*

4.1.2.3 Density and porosity of mixed syntactic foams

Figure 4.6 shows the densities and porosities of the mixed syntactic foams, including fully mixed M1-M3 and partly mixed P1-P3. The density the double-CM syntactic foams is in the range of 1.48-1.64 g/cm^3 and the porosity is in the range of 40%-46.7%. The average densities

of the mixed syntactic foams are also slightly higher than those of the uniform syntactic foams, with the average densities of M1, M2 and M3 being 1.51, 1.59 and 1.53 g/cm^3 (porosities of 45.5%, 42.4% and 44.8, respectively) and the average densities of P1, P2 and P3 being 1.58, 1.56 and 1.55 g/cm^3 (porosities of 42.8%, 43.6% and 44%, respectively).

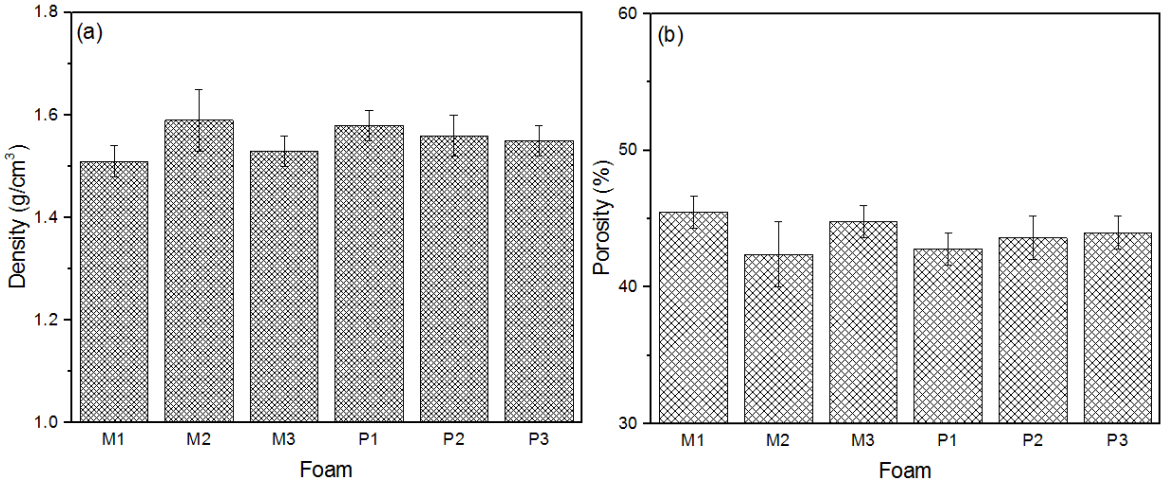

Figure 4.6 *Densities (a) and porosities (b) of mixed syntactic foams*

4.2 Quasi-static loading response

4.2.1 Quasi-static loading response of uniform syntactic foams

Figure 4.7 shows the quasi-static compressive stress-strain curves of the uniform syntactic foams. The three typical regions found in the compression of cellular solids, namely linear elastic, plateau and densification, are observed in all the stress-strain curves. All the curves start with a linear elastic region, followed by a strain-hardening region where the stress increases gradually with increasing strain. The maximum stress of the linear elastic region, i.e. the yield stress of the foam, appears at a strain in the range of 0.03-0.05. The stress-strain curve then enters the plateau region after a small stress drop. In foam U1, this hardening region is nearly linear. In U2 and U3, stress increases in fluctuation. All curves enter the

densification region at a strain in the range of 0.47-0.55, where the stress increases rapidly with a small increase in strain.

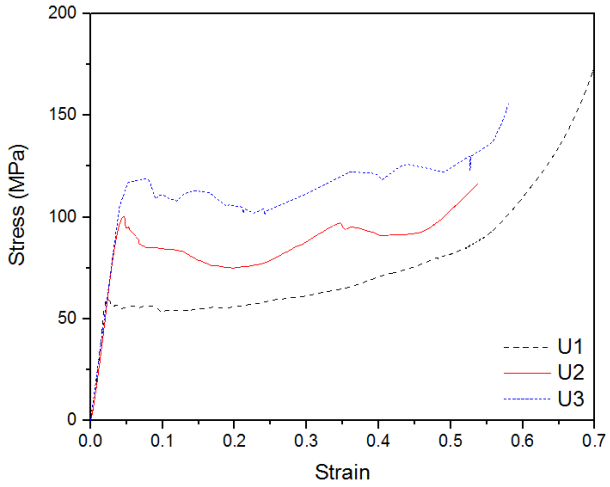

Figure 4.7 *Quasi-static compressive stress-strain curves of uniform AMSFs*

The characteristic compressive properties of the uniform syntactic foams are presented in Table 4.1. The three foams have different yield stresses. With the CM size in U1 to U3 decreasing from L to S, the yield stress increased from 60 MPa to 119 MPa. The apparent Young's modulus, which is defined as the slope of the linear region, is similar between U1, U2 and U3.

Table 4.1 *Characteristic compressive properties of uniform AMSFs*

Specimen	Yield stress (MPa)	Apparent Young's modulus (GPa)	Specific energy absorption (J/g)
U1	60±5	3±0.2	20.3±2
U2	100±6	3±0.2	27.3±2
U3	119±10	2.9±0.2	32.6±3

The specific energy absorption values of the uniform syntactic foams are also shown in Table 4.1. Specific energy absorption is usually defined as the energy absorbed by a unit mass/volume of the syntactic foam from the start of compression up to the onset of densification. It is mainly determined by three factors: density, plateau stress and onset strain of densification, and is shown as the area under the stress-strain curve in quasi-static compression. The onset strain of densification is mainly determined by the porosity of the syntactic foam in equation (4.4). As the densification strain in the uniform syntactic foams is between 0.47 and 0.55, the specific energy absorption is defined here as the energy absorbed by a unit mass of the syntactic foam from the start of compression up to the densification point, which is considered corresponding to 0.5 strain throughout this work for easier comparison.

4.2.2 Quasi-static loading response of layered syntactic foams

Figure 4.8 shows the quasi-static compressive stress-strain curves of the double- and triple-CM layered syntactic foams (D1, D2, D4 and D5, and T1, T2 and T3, respectively). All curves of the double- and triple-CM layered syntactic foams have an initial elastic region with a linear stress-strain relationship. They show different characteristics in the subsequent plastic deformation. D1 (L-S) has a larger stress drop after yield stress in comparison with D2 (L-S-L), D4 (L-S-L-S) and D5 (L-S-L-S-L). Foams T1 (L-M-S) have a stress drop immediately after the stress reaches compressive yield strength, while foam T2 (M-L-S) and T3 (L-S-M) shows a near-plateau region of deformation where the strain increases extensively under a relatively narrow range of stresses.

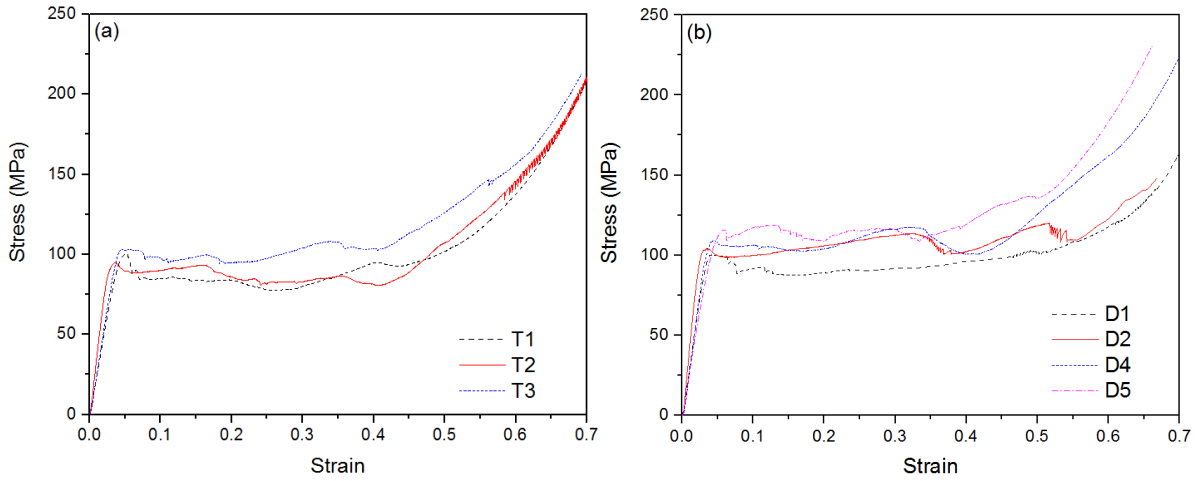

Figure 4.8 *Quasi-static compressive stress-strain curves of triple-CM (a) and double-CM (b) layered AMSFs*

Table 4.2 shows the characteristic compressive properties of the layered syntactic foams. The yield strengths and the specific energy absorptions of the layered syntactic foams lie in the ranges of those of their components, i.e. U1, U2 and U3. The yield strength increases slightly from 100 MPa to 116 MPa in the double-CM syntactic foams D1-D4, with an increasing layer number. The yield strengths for the triple-CM syntactic foams, T1, T2 and T3, are 100, 95 and 102 MPa, respectively. The specific energy absorptions of D1, D2, D3 and D4 are 29, 33.1, 33.6 and 34.8 J/g, respectively, and the specific energy absorptions of T1, T2 and T3 are 26.5, 27.6 and 31.7 J/g, respectively. The apparent Young's modulus of D1, D2, D3 and D4 are 2.7, 3.3, 3 and 2.5 GPa, respectively, and the apparent Young's modulus of T1, T2 and T3 are 2.4, 3.1 and 2.5 GPa, respectively.

It is noted that although both double- and triple-CM syntactic foams contain layers with different yield stresses, they all show only one yield point. This is probably because the layers in the layered AMSFs have low ratios of layer height to sample diameter. The ratio for a CM L layer, which is the softest, ranges from 0.17 to 0.5 in the double-CM foams, D1-D5, and is 0.33

in the triple-CM foams, T1-T3. Low height-to-diameter ratios can reduce the barrelling effect and therefore increase the yield strength of the layer, especially for the weak layer L. The bonding of the weak layer L to the stronger layer S or M at the boundaries can also provide extra strength for the weak layer L due to constrained compression. The coordinated deformation makes the individual layers with different strengths act the same way as the uniform syntactic foams and have similar compression stress-strain curves.

Table 4.2 *Characteristic compressive properties of layered AMSFs*

Specimen	Yield stress (MPa)	Apparent Young's modulus (GPa)	Specific energy absorption (J/g)
T1	100	2.4	26.5
T2	95	3.1	27.6
T3	102	2.5	31.7
D1	100	2.7	29.0
D2	104	3.3	33.1
D4	109	3	33.6
D5	116	2.5	34.8

4.2.3 Quasi-static loading response of mixed syntactic foams

Figure 4.9 shows the compressive response of fully mixed syntactic foam M2 (50% L/50% S) and partly mixed syntactic foam P2 (L - 50%L/50%S - S - 50%L/50%S - L). It seems the mixed syntactic foams have larger stress drops in compression than the layered syntactic foams. An example is the drop at the strain range of 0.33-0.43 in P2, which is caused by cracks emerging during compression.

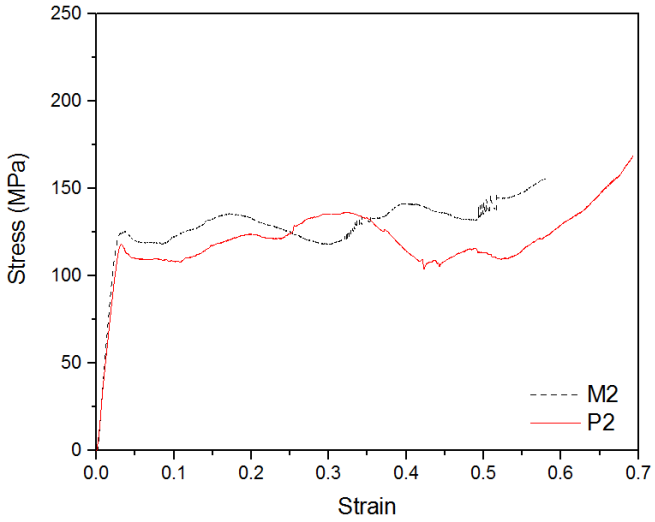

Figure 4.9 *Quasi-static compressive stress-strain curves of mixed AMSFs*

Table 4.3 shows the characteristic compressive properties of the two mixed foams. The increase in yield strength, and accordingly specific energy absorption, in mixed foams can be explained by the effect of mixing large CMs with small CMs. The dispersion of small CMs in the interstices between large CMs strengthens the matrix in the mixed syntactic foams.

Table 4.3 *Characteristic compressive properties of mixed AMSFs*

Specimen	Yield stress (MPa)	Apparent Young's modulus (GPa)	Specific energy absorption (J/g)
M2	126	4.4	39.4
P2	118	4	37.2

4.3 Impact loading response

4.3.1 Impact loading response of uniform syntactic foams

4.3.1.1 Impact stress evolution

Figure 4.10 shows the typical impact stress-time traces of the uniform syntactic foams U1, U2 and U3 under different impact energy levels. The peak stress values for these samples are

listed in Table 4.4. The impact stress represents the stress pulse produced by the impact of the drop-weight on the cubical specimen. It was calculated by dividing the real time impact load by the cross-sectional area of the specimen. In general, the stress response evolves in an oscillation way. In most cases, the stress-time curves can be divided into three regions, a linear elastic region, an oscillating plateau region, and a densification region. Densification region is defined as the region where the impact stress increase significantly after the sample is densified. For convenient comparison between samples, a nominal strain of 0.5 can be considered as the start of densification.

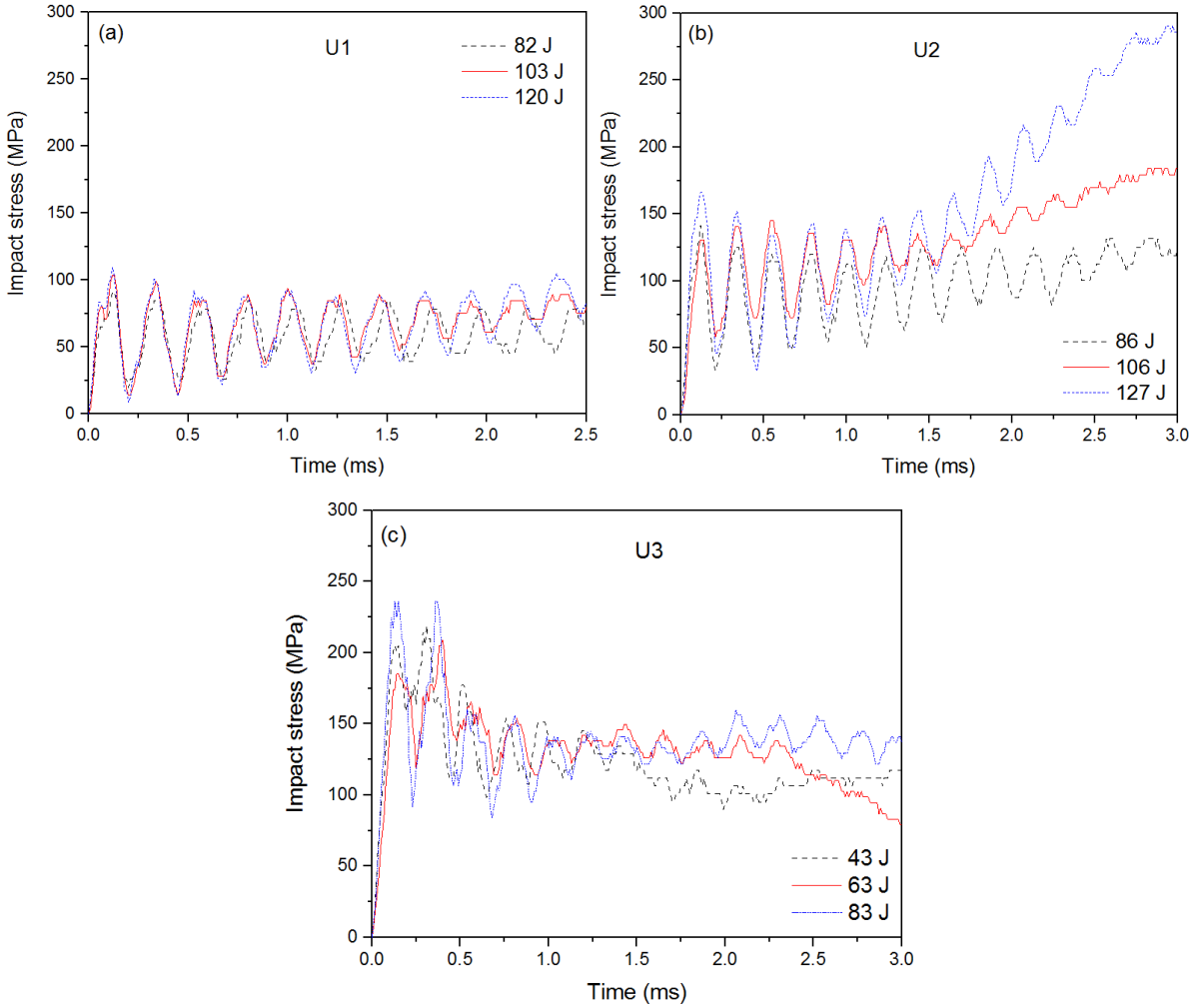

Figure 4.10 *Stress-time traces of uniform ASMFs (a) U1, (b) U2 and (c) U3 at three different impact energy levels in drop-weight test*

Table 4.4 *Peak stress, maximum strain, densification time and specific energy absorption in impact test of uniform AMSFs under different impact energy levels*

Sample	Impact energy (J)	Peak stress (MPa)	Maximum strain	Time to reach densification (ms)	Specific energy absorption (J/g)
U1	82	92	0.6	2.8	26.8
	103	103	0.7	2.5	31
	120	109	0.8	2.1	28.5
U2	86	141	0.45	-	40
	106	131	0.55	2.6	46
	127	166	0.7	2	43
U3	43	205	0.25	-	20.5
	63	185	0.33	-	31
	83	236	0.4	-	42

In U1 (L), the maximum peak stress appears at the end of the elastic region, i.e., at the first impact oscillation. The impact peak stress of each subsequent oscillation decreases gradually. The oscillation amplitude also decreases with the impact process. At the end stage of impact, between 1.75 ms and 2.5 ms, the increase of impact stress under an impact energy of 120 J indicates the start of densification. In U2 (M), a similar trend is shown, with the maximum peak stress at beginning, plateau region in the middle and densification region at the end. In U3 (S), the peak stress is significantly higher at the beginning and drops dramatically in the plateau region. The impact stress keeps dropping at the end of impact due to brittle fracture. In all three samples, the average impact stress in each oscillation is similar to the stress under quasi-static loading, although the peak stress is significantly higher than the average stress. Besides, the impact stress increases slightly with impact energy.

It is noted that the stress oscillations in all the uniform foam samples have almost the same time period of about 0.2-0.25 ms, although they contain different types of CMs and are tested under different impact conditions. Johnson (1972) pointed out that impact loading creates elastic wave as well as plastic wave inside the sample. The speeds of these waves are determined by the elastic and plastic moduli of the syntactic foam, which can be determined from the quasi-static stress-strain curve in the elastic and plastic deformation stages, respectively. When the waves hit the top or bottom side of the sample, the impact stress shows an oscillation. Because samples U1, U2 and U3 have a similar plastic modulus, the oscillation time period is similar according to the impact wave theory.

4.3.1.2 Impact strain evolution

Figure 4.11 shows the typical impact strain-time traces of the uniform syntactic foams U1, U2 and U3 under different impact energy levels. The maximum strain values for these samples are listed in Table 4.4. The impact strain represents the relative amount of deformation of the sample caused by the moving impact hammer. It was calculated by dividing the real-time displacement of the impact hammer by the height of the specimen, which was measured from the image captured by a high-speed camera. In general, the strain response evolves according to impact energy and impact velocity, with higher impact energy leading to higher strain.

In U1 (L), the impact hammer travels with small amount of velocity loss as the impact energy is significantly higher than the energy needed to densify the sample. This leads to an almost linear relation between strain and time. In comparison, U2 (M) has a two-stage strain-time

evolution. The strain increases linearly with time in the beginning and then the slope decreases due to the loss of impact hammer velocity, because U2 consumes more energy to densify. U3 (S) shows three stages in strain-time evolution: linear region, decreasing slope region and constant strain region. U3 has the highest strength and specific energy absorption among the three uniform foams, so it absorbs the impact energy more quickly. At any of the three impact energy levels, 43 J, 63 J and 83 J, the impact hammer stopped before full densification of the syntactic foam occurred.

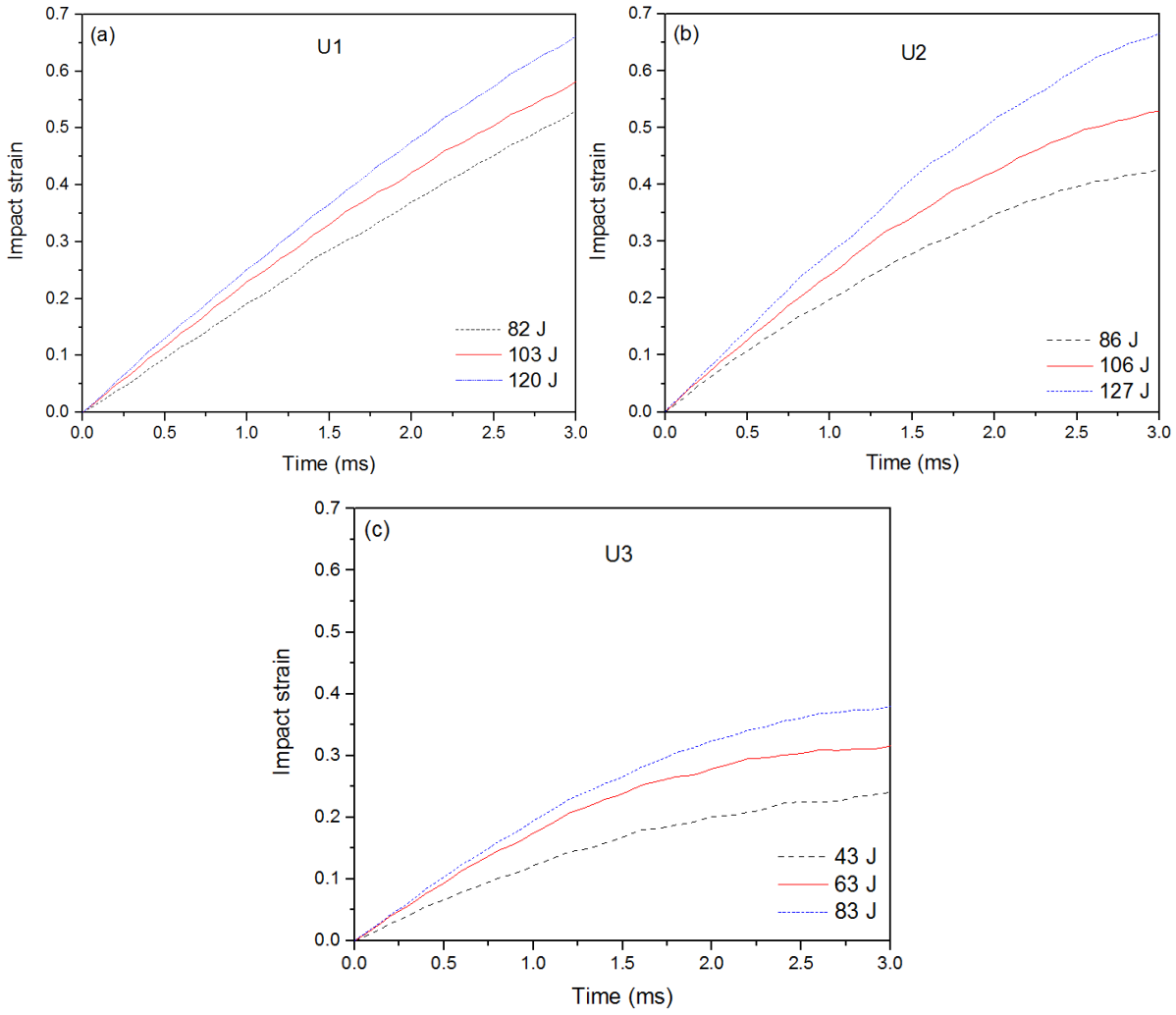

Figure 4.11 *Strain-time traces of uniform ASMFs (a) U1, (b) U2 and (c) U3 at three different impact energy levels in drop-weight test*

4.3.1.3 Impact velocity evolution

Figure 4.12 shows the typical impact velocity-time traces of the uniform syntactic foams U1, U2 and U3 under different impact energy levels. The impact velocity is the velocity of the impact hammer measured by a high speed camera. In general, the impact velocity evolves according to energy absorption in the syntactic foam, with higher energy absorption leading to lower impact velocity.

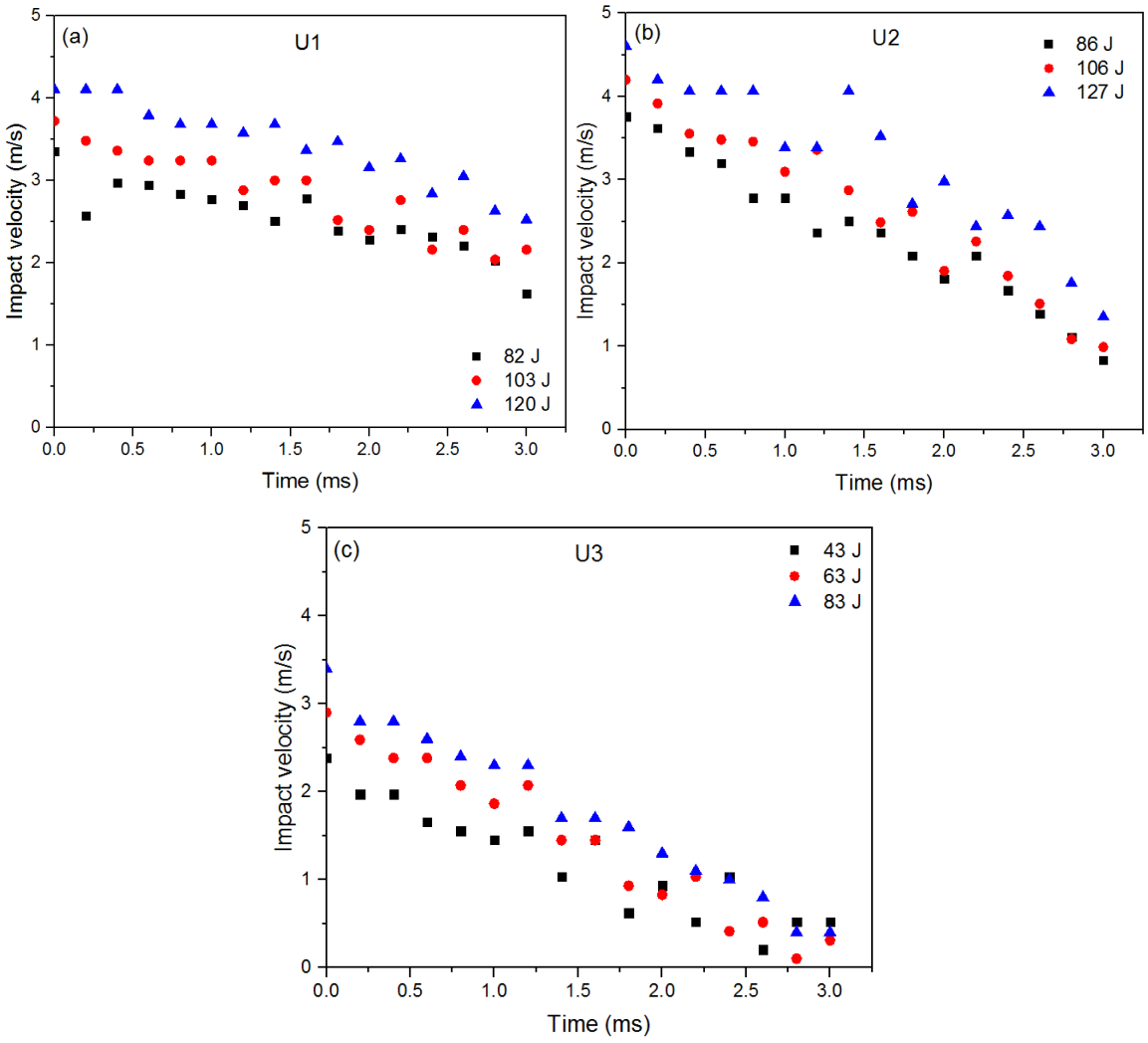

Figure 4.12 *Velocity-time traces of uniform ASMFs (a) U1, (b) U2 and (c) U3 at three different impact energy levels in drop-weight test*

All syntactic foams, U1-U3, show a generally decreasing velocity with time, indicating the energy absorption process. There is an approximately linear relation between velocity and

time. Nevertheless, some oscillations are shown in the results. The oscillations are due to the velocity measurement method used in this work. In the measurements, the evolution of velocity was acquired by a high speed camera with an interval of 0.2 ms per frame by tracking a specific point on the hammer.

4.3.1.4 Impact energy absorption evolution

Figure 4.13 shows the typical impact energy absorption-time relations for the uniform syntactic foams U1, U2 and U3 under different impact energy levels. The specific energy absorption values for these samples are listed in Table 4.4. The impact energy absorption represents the energy absorbed by the sample due to deformation. Neglecting energy loss caused by friction and temperature change of the sample during impact, all kinetic energy loss of the impact hammer can be assumed to be absorbed by the syntactic foam. The impact energy absorption was therefore calculated as initial kinetic energy minus kinetic energy of the impact hammer at each time point, i.e., the kinetic energy loss of the impact hammer. Therefore, the energy absorption response evolves according to the impact velocity response. The energy absorption increases with decreasing impact velocity.

All uniform syntactic foams, U1-U3, show an increasing energy absorption with time, as the kinetic energy of hammer is absorbed by the specimen. The evolution of energy absorption also shows oscillations, due to the velocity oscillations. In U1 (L) and U2 (M), energy absorption increases steadily until the sample is densified, as the impact energy is higher than the sample's energy absorption capacity. At 86 J, the energy absorption in U2 increases more

slowly at the end of impact (2.5-3 ms), because this impact energy is just enough to densify the specimen. In U3 (S), energy absorption stops increasing before full densification under all three impact energy levels, because all the impact energy has been absorbed before the sample is densified.

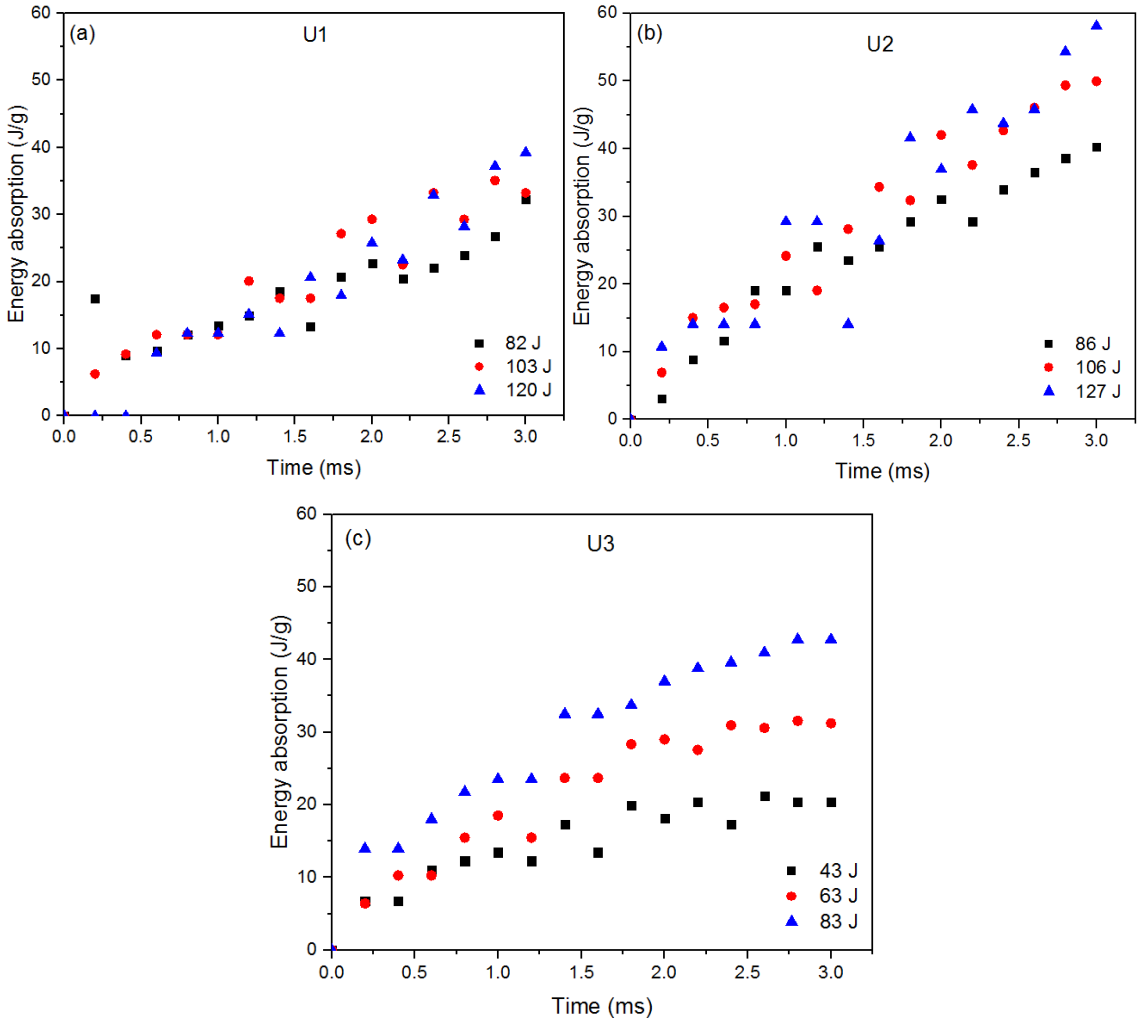

Figure 4.13 *Energy absorption-time relations for uniform ASMFs (a) U1, (b) U2 and (c) U3 at three different impact energy levels in drop-weight test*

It is noted that all the syntactic foams, U1, U2 and U3, absorb more energy in impact than in quasi-static loading at the same strain. For example, Sample U2 absorbs 46.3 J/g at a nominal densification strain of 0.5 under an impact energy of 106 J and at an impact velocity of 2.61 m/s, while the specific energy absorption of U2 under quasi-static loading is 27.3 J/g, as shown

in Table 4.1. This is because impact loading generates impact waves, which lead to higher impact stress than quasi-static loading.

4.3.1.5 Impact deformation sequence

Figures 4.14, 4.15 and 4.16 show the typical first 5 frames from the images, acquired by a high speed camera, of the uniform syntactic foams U1, U2 and U3 during impact under different impact energy levels. The 5 frames represent the times at 0, 0.2, 0.4, 0.6 and 0.8 ms, as the time interval between two frames is 0.2 ms. Impact loading causes higher peak stress than quasi-static loading, especially at the beginning. These frames can reveal the effect of such high peak stresses on the deformation and fracture of the sample.

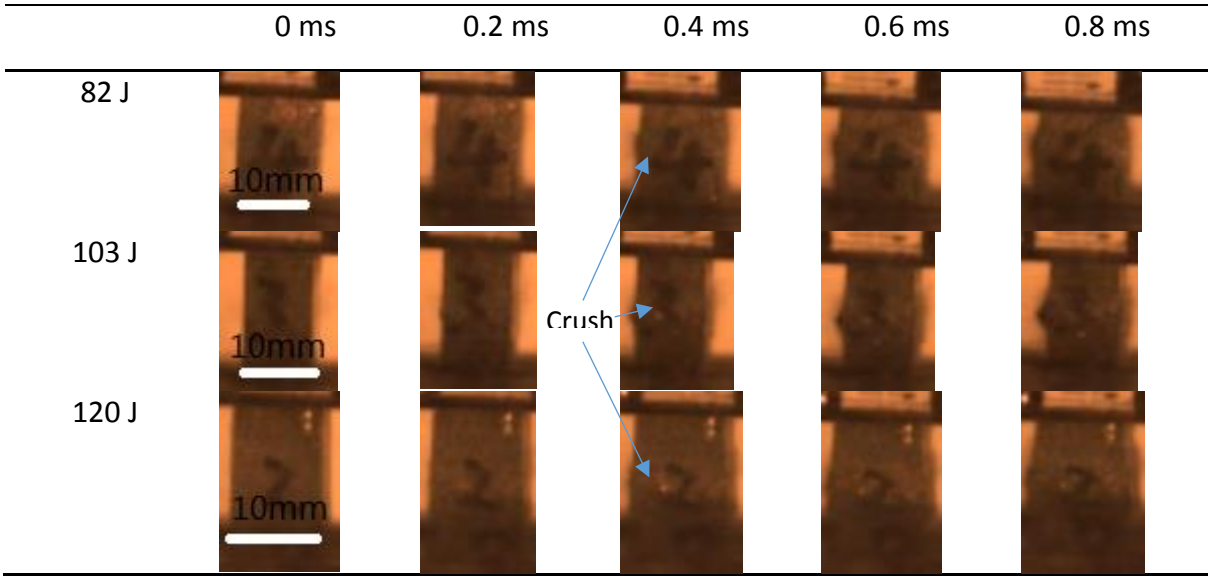

Figure 4.14 *First 5 frames acquired during impact of U1 under different impact energy levels*

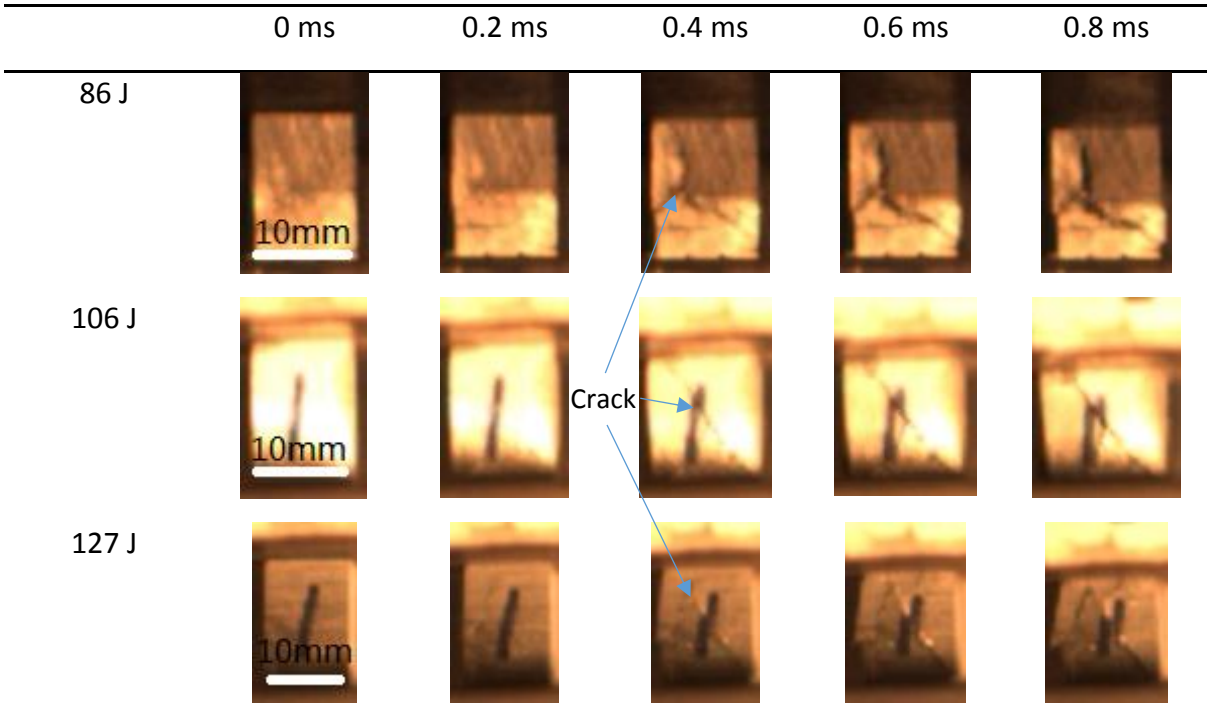

Figure 4.15 *First 5 frames acquired during impact of U2 under different impact energy levels*

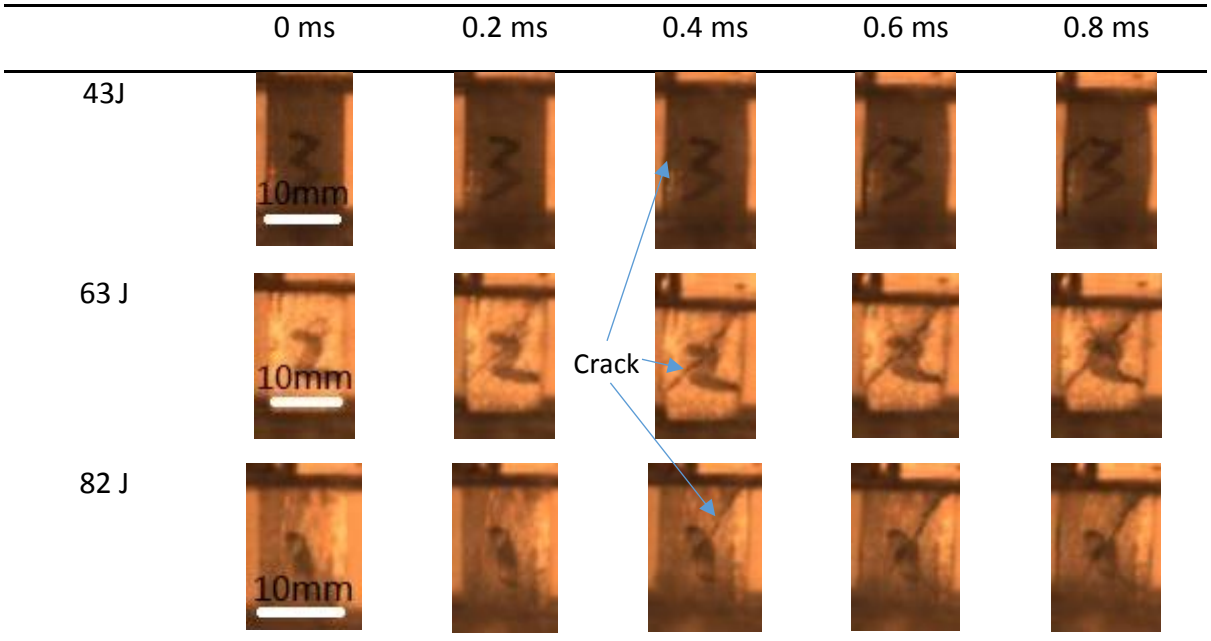

Figure 4.16 *First 5 frames acquired during impact of U3 under different impact energy levels*

Three different types of deformation were observed under impact. First, ductile deformation, where the syntactic foam is crushed layer by layer. This was observed in U1 (L) under all the three impact energy levels. Second, brittle fracture, where the sample cracks at the beginning

stage of impact and propagates through the whole sample. U2 (M) at all three impact energy levels and U3 (S) at 63 J and 82 J showed this type of fracture. Some samples showed one crack (e.g., U2 under 106 J), while others had X-shaped cracks (e.g., U3 under 63 J). Third, ductile-brittle fracture, where the deformation is a combination between ductile deformation and brittle fracture. U3 under 43 J is an example, where a partial crack appeared in the middle of the sample.

4.3.2 Impact loading response of layered syntactic foams

4.3.2.1 Impact stress evolution

Figures 4.17 and 4.18 show the typical impact stress-time traces of double-CM syntactic foams (D1-D6) and triple-CM syntactic foams (T1-T3), respectively, under different impact energy levels. The peak stress values for these samples are listed in Table 4.5. To study the effect of impact direction, T1 (L-M-S) was impacted from both directions and was designated as Ti-up when impacted from the L layer side or T1-down when impacted from the S layer side. The stress response of layered syntactic foams is similar to uniform syntactic foams and evolves in an oscillation manner. In most cases, the stress-time curves can be divided into three regions, a linear elastic region, an oscillating plateau region, and a densification region. For the cases where the impact energy is insufficient for full densification, like T3 40 J and 59 J, the stress drops at the end of the impact process.

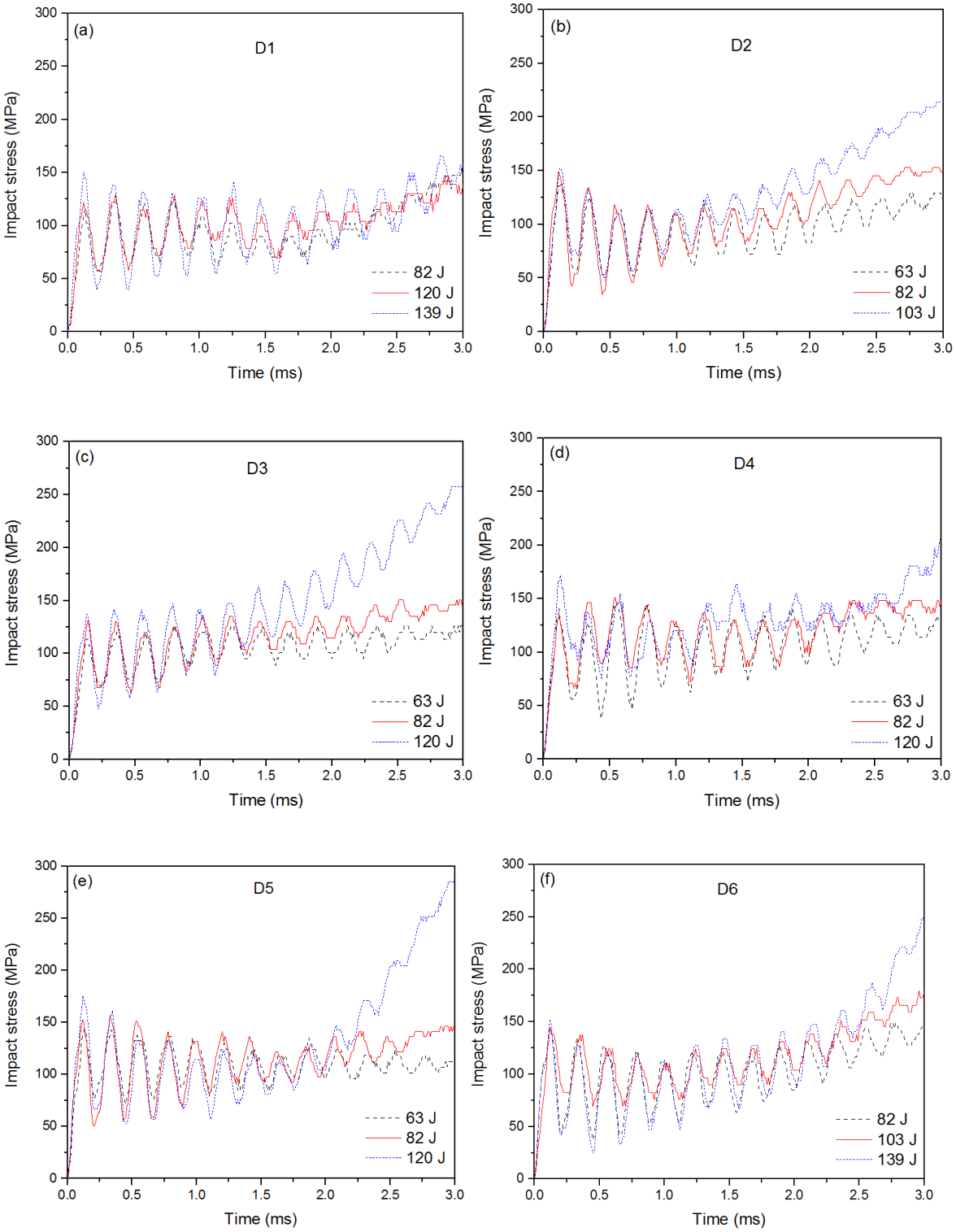

Figure 4.17 *Stress-time traces of double-CM layered ASMFs: (a) D1, (b) D2, (c) D3 (d) D4, (e) D5 and (f) D6 in drop-weight test at three different impact energy levels*

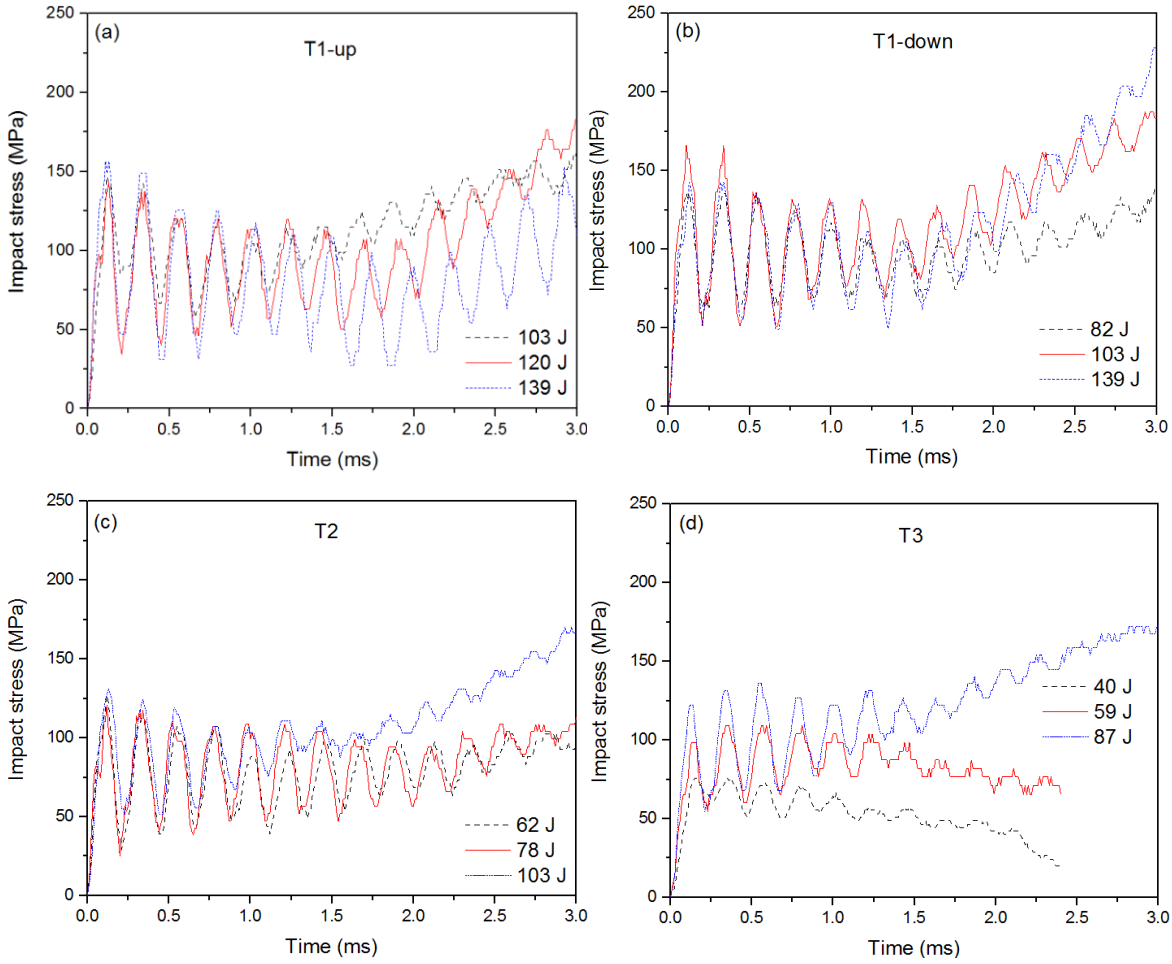

Figure 4.18 *Stress-time traces of triple-CM layered ASMFs: (a) T1-up, (b) T1-down, (c) T2 and (d) T3 in drop-weight test at three different impact energy levels*

Table 4.5 *Peak stress, maximum strain, densification time and specific energy absorption in impact test of layered AMSFs under different impact energy levels*

Sample	Impact energy (J)	Peak stress (MPa)	Maximum strain	Time to reach densification (ms)	Specific energy absorption (J/g)
D1	82	120	0.55	3	33
	120	115	0.75	2.2	35
	139	150	0.8	2	40
D2	63	137	0.5	3.2	31
	82	148	0.55	2.5	36
	103	152	0.6	2.3	39
D3	63	118	0.5	3.4	31
	82	130	0.55	3	34
	120	137	0.7	2.4	45
D4	63	142	0.5	3.4	31
	82	133	0.55	3	37
	120	170	0.7	2.4	40

D5	63	143	0.45	-	31
	82	151	0.55	3	39
	120	175	0.75	1.9	42
D6	82	144	0.6	2.6	35
	103	145	0.67	2.3	42
	139	151	0.8	1.7	39
T1-up	103	147	0.65	2.3	28
	120	146	0.75	2	30
	139	154	0.8	1.9	27
T1-down	82	132	0.57	2.8	30
	103	142	0.7	2.1	29
	139	165	0.8	1.9	33
T2	62	125	0.4	-	31
	78	119	0.5	3.5	31
	103	130	0.6	3	43
T3	40	76	0.15	-	20
	59	97	0.32	-	28
	87	124	0.5	3.5	35

In D1 (L-S), all three samples were densified at about 2 ms, with the impact peak stress increasing with the impact energy increased from 82 J to 120 J and then to 139 J. In D2 (L-S-L), the peak stress is similar among the three impact energy levels, 63 J, 82 J and 103 J. However, the impact stress after densification under 103 J is significantly higher than that at 63 J and 82 J. In D3 (S-L-S), the peak stress also increases with increasing impact energy. After densification at about 1.5 ms, the impact stress under 120 J is much higher than that under lower impact energies. In D4 (L-S-L-S), the peak stress under 120 J is significantly higher than that under 63 J and 82 J. In D5 (L-S-L-S-L), the impact stress under 120 J is extremely high after densification at 1.75 ms, reaching 280 MPa at the end. Such high impact stress (> 250 MPa) is also shown in D6 (S-L-S-L-S) under 139 J.

In T1 (L-M-S), the maximum peak stress appears at the end of the elastic region, i.e. at the first impact oscillation. The impact peak stress of each subsequent oscillation decreases

gradually. The oscillation amplitude also decreases with the impact process. The increase of impact stress at about 2 ms in the late stage of impact indicates the start of densification. Comparing Figs. 4-18(a) and (b) shows that switching the side of sample under impact loading has little effect on the behaviour. T2 (S-M-L) shows a similar trend, with peak stress appearing at the beginning, followed by plateau and then densification regions. The impact stress-time traces under 62 J and 78 J are similar, while the impact stress in the densification region under 103 J is significantly higher. Unlike in quasi-static loading, where strain is evenly distributed across the sample, impact loading causes uneven strain distribution in the sample. Some parts of the sample may be densified while other parts are not densified and even not strained. This is especially evident in layered syntactic foams where the layers have different yield stresses. Soft layers can densify before strong layers and the densified part can result in a significantly higher impact stress. In T3 (M-L-S), impact energies of 40 J and 59 J are not sufficient to densify the specimen and the impact process terminates before densification. The impact stress drops in the last stage, instead of increasing.

In layered syntactic foams, each oscillation in the impact stress-time traces has a similar period time of 0.2-0.25 ms, which is similar to uniform syntactic foams. The oscillation represents the propagation of impact waves inside the sample (the effect of such impact waves will be discussed in Chapter 5). The quasi-static compression results showed that the layered syntactic foams have a similar plastic modulus as the uniform syntactic foams. Therefore, the oscillation period time is also similar.

4.3.2.2 Impact strain evolution

Figures 4.19 and 4.20 show the typical impact strain-time traces of the double- and triple-CM layered syntactic foams, respectively, under different impact energy levels. In general, the strain evolves according to impact energy and impact velocity, with higher impact energy leading to higher strain. Similar as in uniform syntactic foams, slight oscillation is also shown in strain-time evolution in some specimens.

The effect of impact energy on densification time (the time to reach 0.5 strain) and maximum strain can be seen in Table 4.4. In double-CM AMSFs D1-D6, it generally takes about 60-80 J and 2-3 ms to densify the specimen. More impact energy leads to shorter time to reach densification and larger maximum strain. Comparisons among D1 (L-S), D2 (L-S-L), D4 (L-S-L-S) and D5 (L-S-L-S-L) show that more layers lead to smaller maximum strain, indicating more energy absorption capacity. In the triple-CM AMSF T1-up, impact hammer travels with a small amount of velocity loss, as the impact energy level is higher than the energy needed to densify the sample. There is an almost linear relation between strain and time. The impact process ends at 0.6-0.7 strain after sample is densified. T1-down shows a similar trend, confirming that impact direction does not matter. Comparison among T1 (L-M-S), T2 (M-L-S) and T3 (L-S-M) shows that it takes about 80 J to densify the specimens.

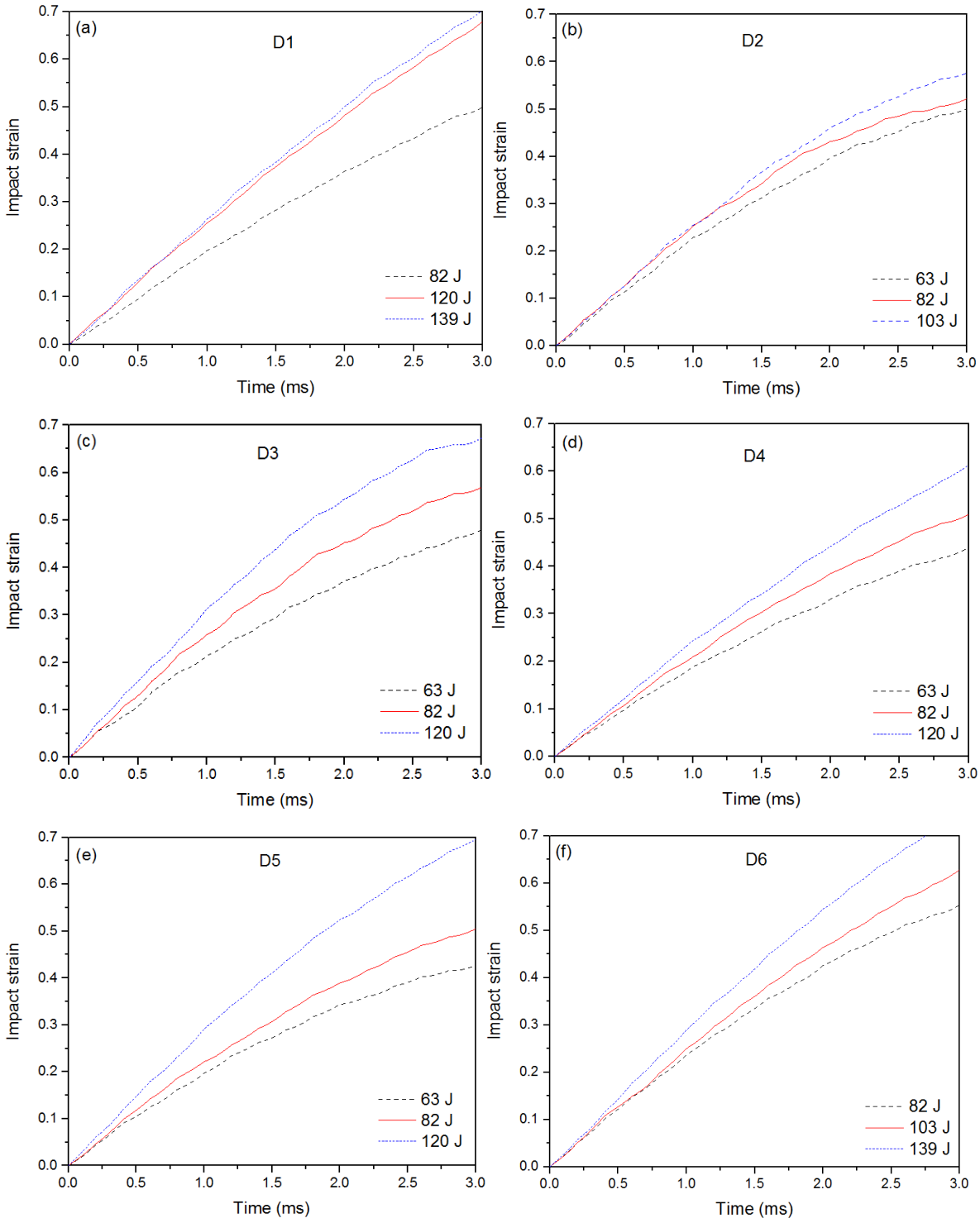

Figure 4.19 *Strain-time traces of double-CM layered ASMFs: (a) D1, (b) D2, (c) D3 (d) D4, (e) D5 and (f) D6 in drop-weight test at three different impact energy levels*

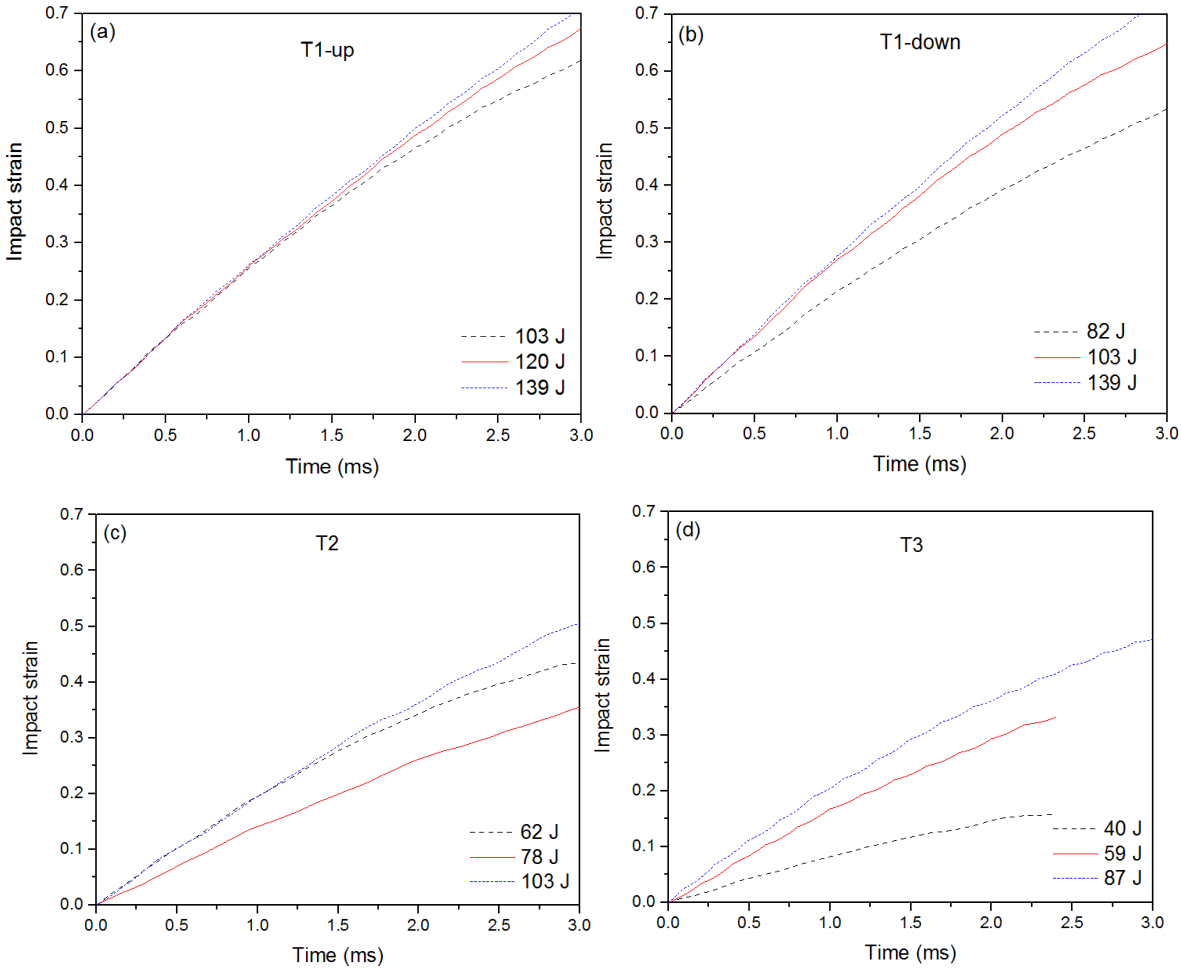

Figure 4.20 *Strain-time traces of triple-CM layered ASMFs: (a) T1-up, (b) T1-down, (c) T2 and (d) T3 in drop-weight test at three different impact energy levels*

4.3.2.3 Impact velocity evolution

Figures 4.21 and 4.22 show the typical impact velocity-time traces of the double-CM syntactic foams D1-D6 and triple-CM syntactic foams T1-up, T1-down, T2 and T3 under different impact energy levels, respectively. The impact velocity is the velocity of the impact hammer measured by a high speed camera. In general, the impact velocity evolves according to energy absorption in the syntactic foam, with higher energy absorption leading to lower impact velocity. Similar to uniform syntactic foams, double- and triple-CM syntactic foams show a generally decreasing velocity with time, indicating the energy absorption process. There is an

approximately linear relation between velocity and time. Nevertheless, some oscillations are shown in the results, which are characteristic in impact.

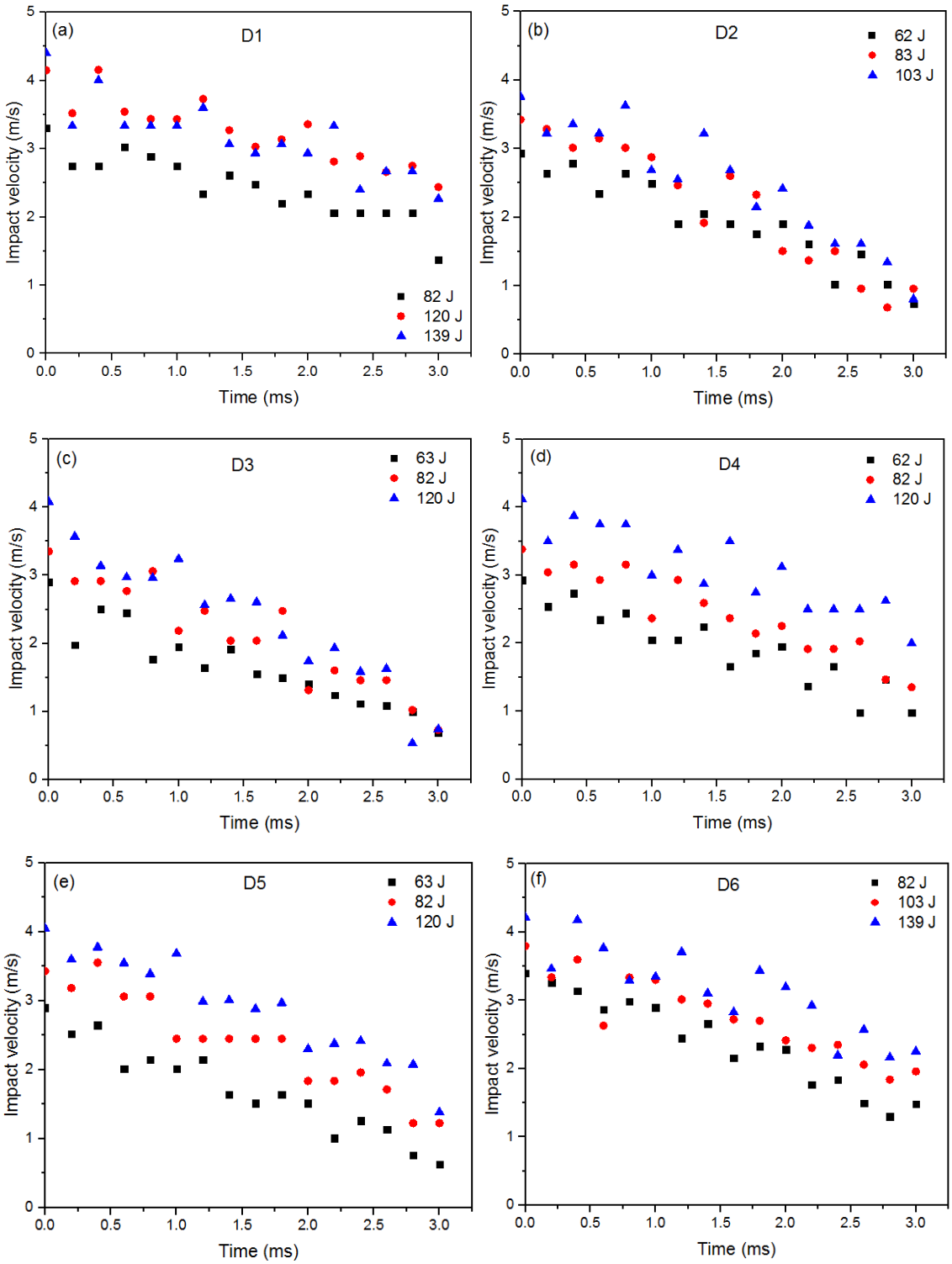

Figure 4.21 *Velocity-time traces of double-CM layered ASMFs (a) D1, (b) D2, (c) D3 (d) D4, (e) D5 and (f) D6 in drop-weight test at three different impact energy levels*

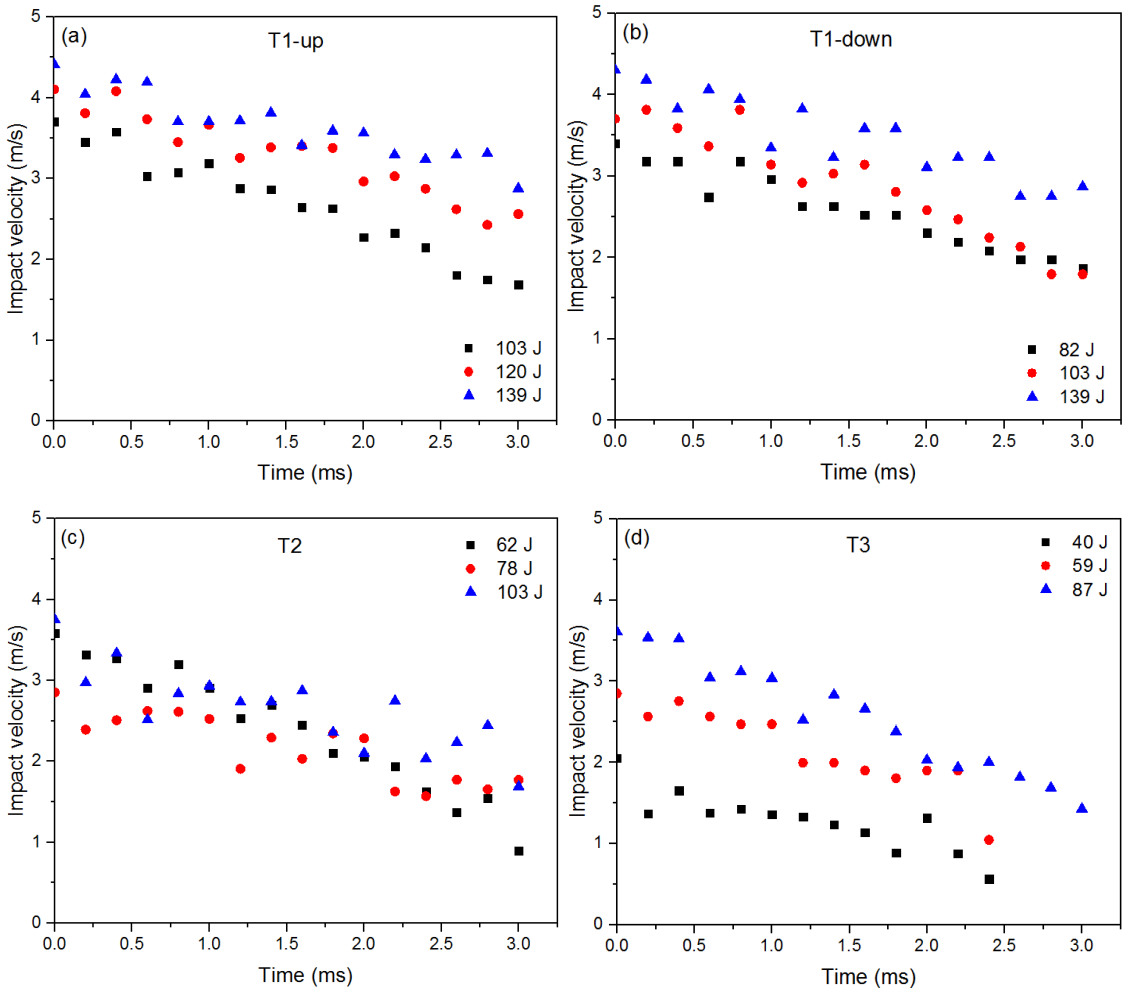

Figure 4.22 *Velocity-time traces of triple-CM layered ASMFs (a) T1, (b) T2, (c) T3 and (d) T4 in drop-weight test at three different impact energy levels*

4.3.2.4 Impact energy absorption evolution

Figures 4.23 and 4.24 show the typical impact energy absorption-time relation for the double-CM syntactic foams D1-D6 and triple-CM syntactic foams T1-T3 under different impact energy levels. Similar to uniform syntactic foams, double-CM syntactic foams show an increasing energy absorption with time and with decreasing impact velocity. A higher impact energy level generally leads to a higher energy absorption in all the double-CM specimens. A similar trend is shown in triple-CM layered syntactic foams. All three samples, T1 (L-M-S), T2 (M-L-S) and T3 (L-S-M), had similar energy absorption, indicating that layer order has no effect on

energy absorption capacity. Besides, energy absorption of the triple-CM layered syntactic foams is slightly lower than the average of their constituent layers. All double- and triple-CM syntactic foams absorb more energy under impact loading than under quasi-static loading at the same strain, due to increased stress caused by the impact waves, as explained in the case of uniform syntactic foams.

The relation between specific energy absorption and impact energy can also be seen in Table 4.4. Generally, specific energy absorption increases with increasing impact energy in both double- and triple-CM AMSFs. The number and order of layers have no significant effect on the specific energy absorption.

4.3.2.5 Impact deformation sequence

Figures 4.25-4.34 show the typical first 5 frames from the images, acquired by a high speed camera, of each of the double- (D1-D6) and triple-CM (T1-T3) syntactic foams under different impact energy levels. As in uniform syntactic foams, three different types of deformation were observed in the layered syntactic foams: ductile, brittle and ductile-brittle deformation. In double-CM syntactic foams, a sample consisting of several thin layers leads to brittleness with lower impact energy than a sample with fewer thick layers. Similar with double-CM AMSFs, L is also ductile and S is brittle In triple-CM syntactic foams, cracks generally emerge in brittle S layers while the ductile L layers remain ductile, regardless of layer order. Increasing impact energy generally increases the sample's tendency of brittle deformation.

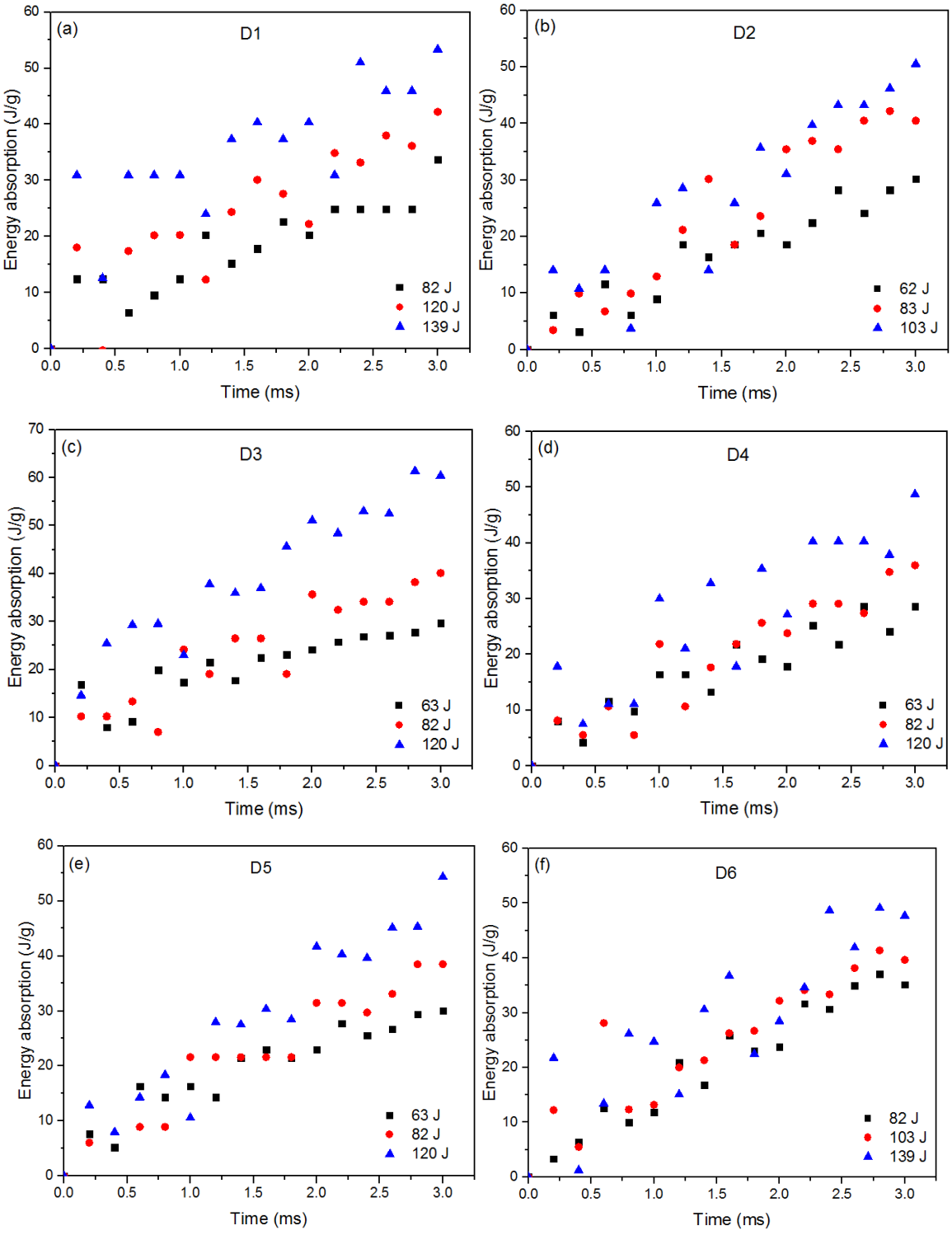

Figure 4.23 *Energy absorption-time traces of double-CM layered ASMFs (a) D1, (b) D2, (c) D3 (d) D4, (e) D5 and (f) D6 in drop-weight test at three different impact energy levels*

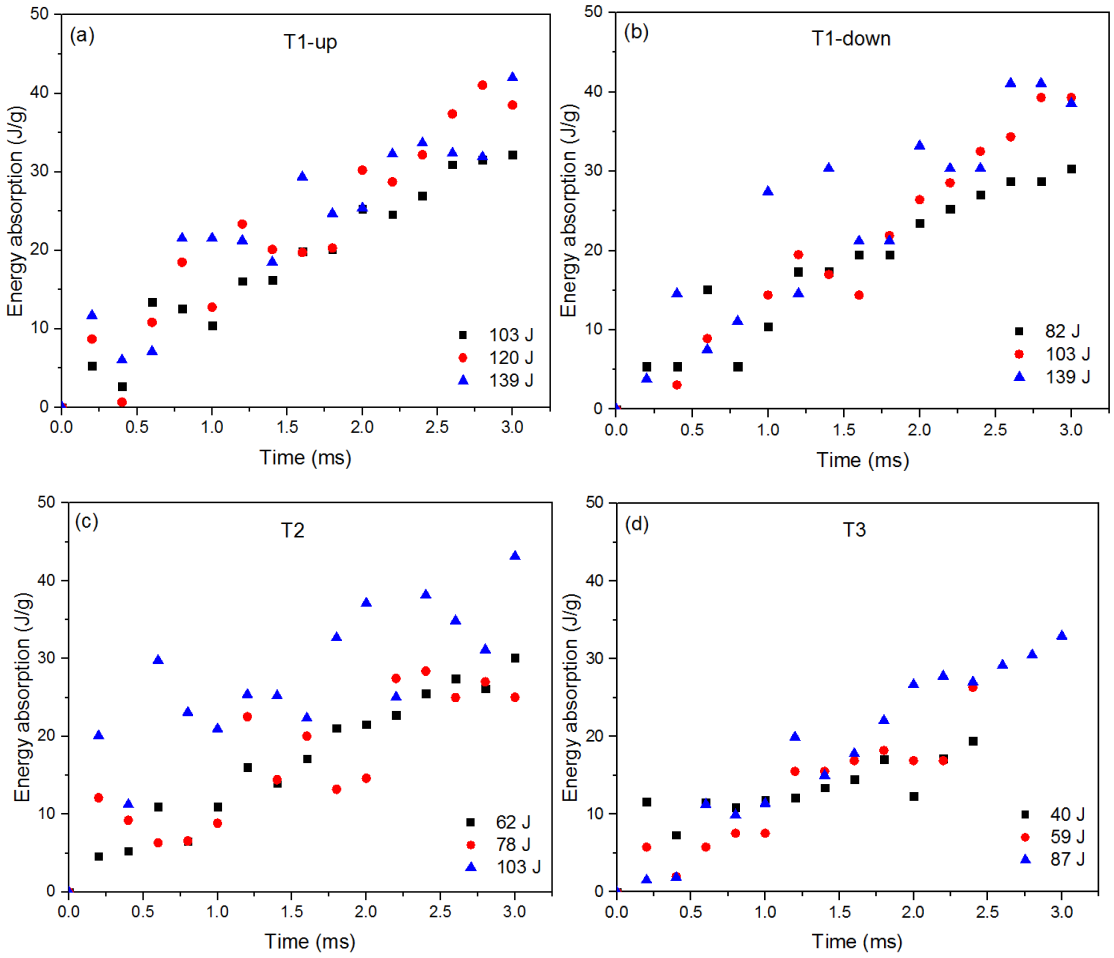

Figure 4.24 *Energy absorption-time traces of triple-CM layered ASMFs (a) T1, (b) T2, (c) T3 and (d) T4 in drop-weight test at three different impact energy levels*

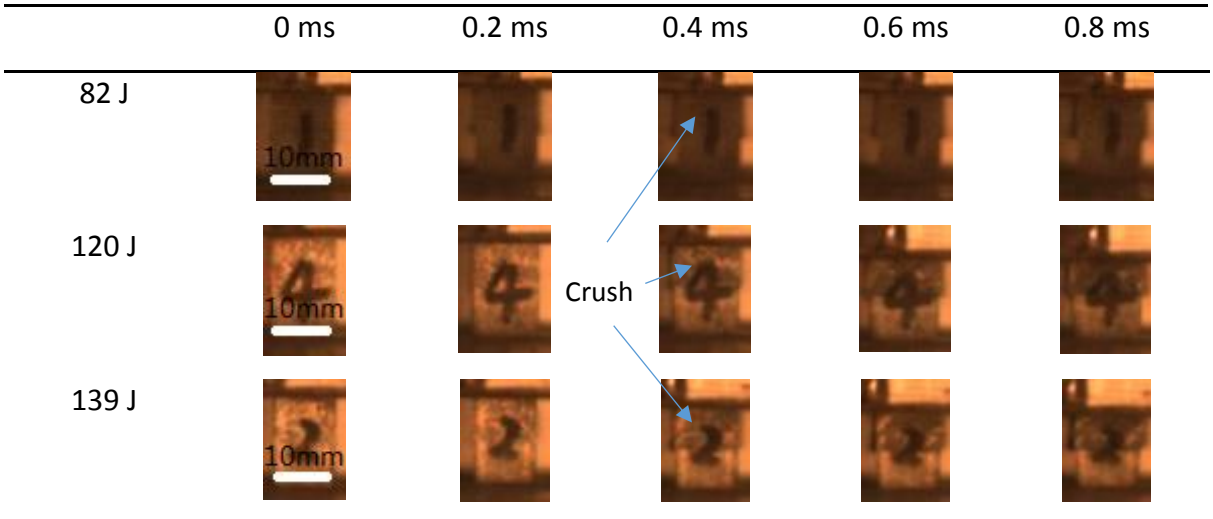

Figure 4.25 *First 5 frames acquired during impact of double-CM layered syntactic foam D1 under different impact energy levels*

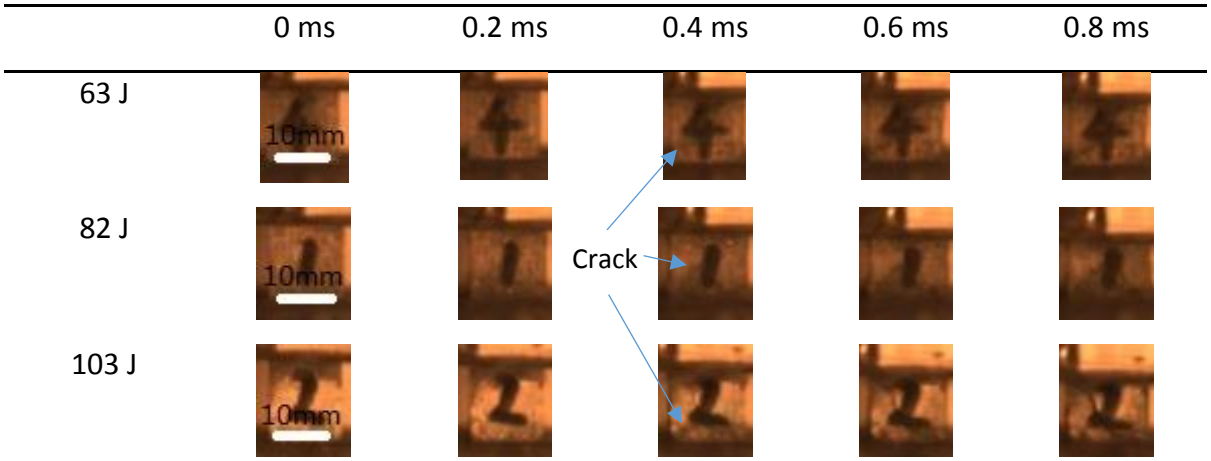

Figure 4.26 *First 5 frames acquired during impact of double-CM layered syntactic foam D2 under different impact energy levels*

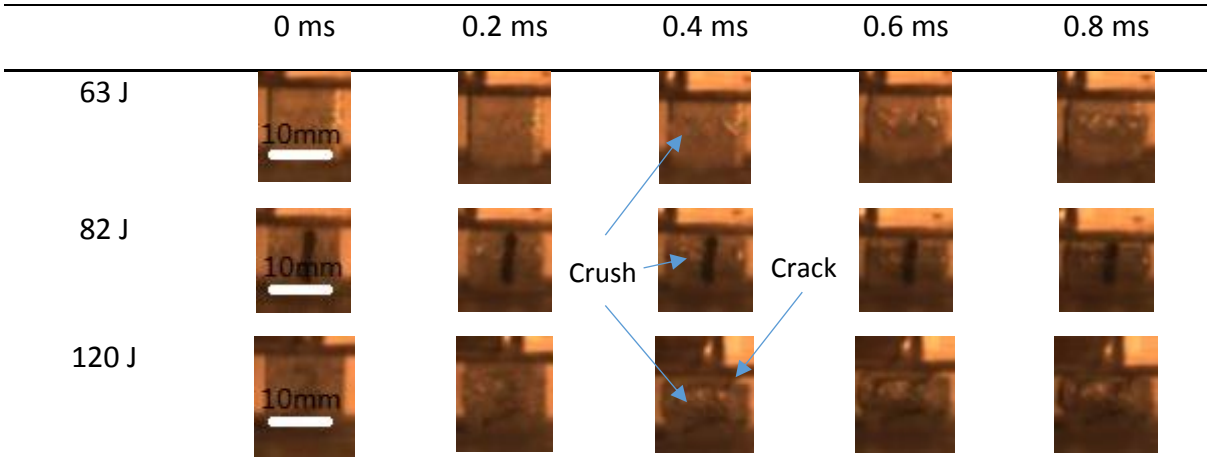

Figure 4.27 *First 5 frames acquired during impact of double-CM layered syntactic foam D3 under different impact energy levels*

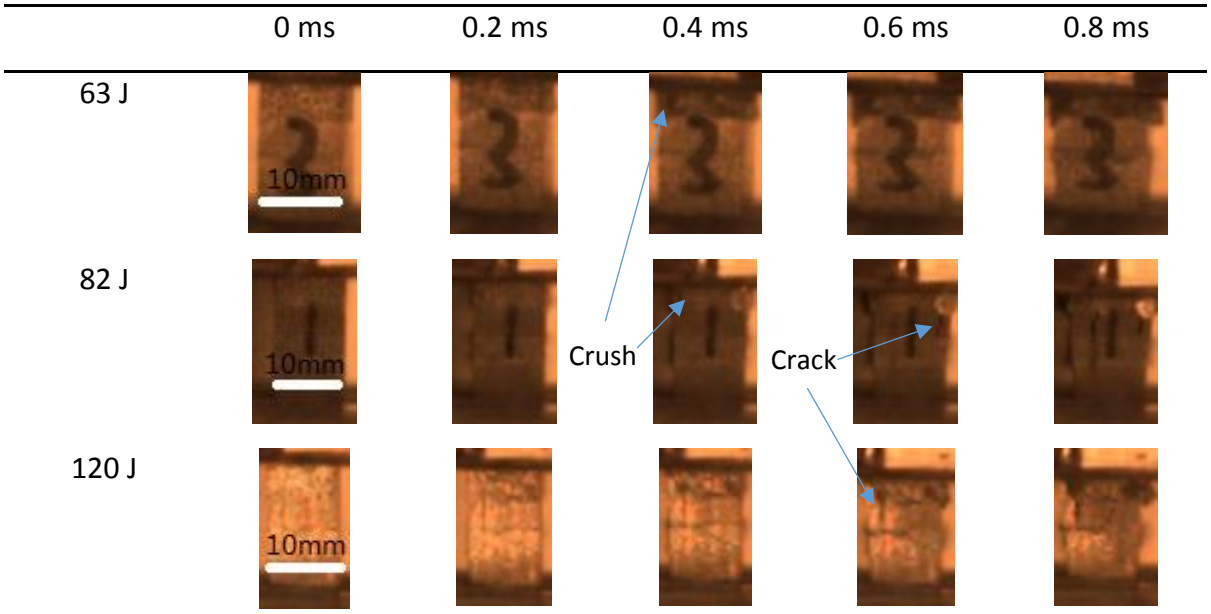

Figure 4.28 *First 5 frames acquired during impact of double-CM layered syntactic foam D4 under different impact energy levels*

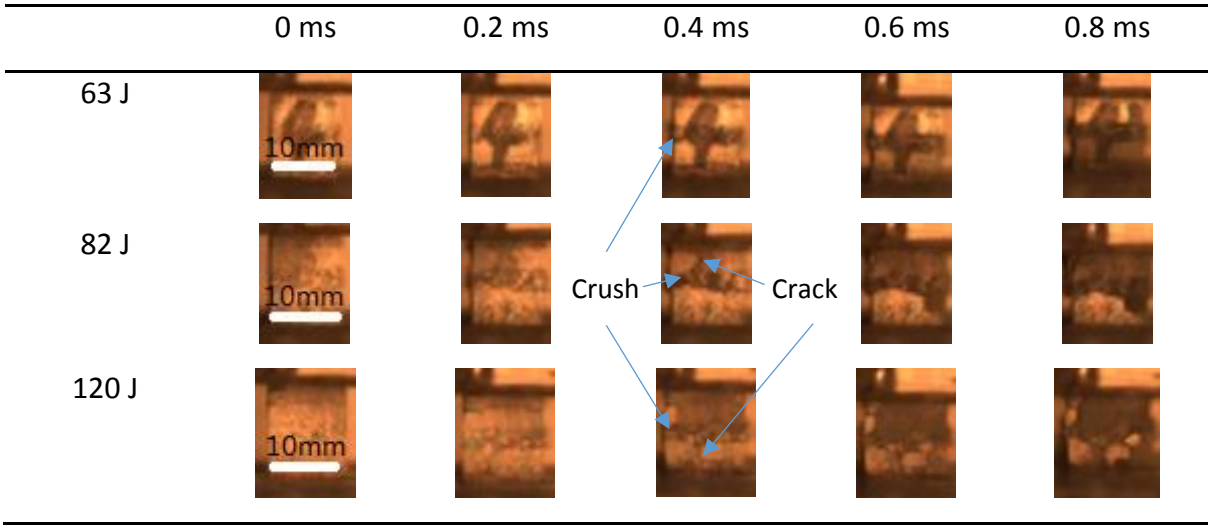

Figure 4.29 *First 5 frames acquired during impact of double-CM layered syntactic foam D5 under different impact energy levels*

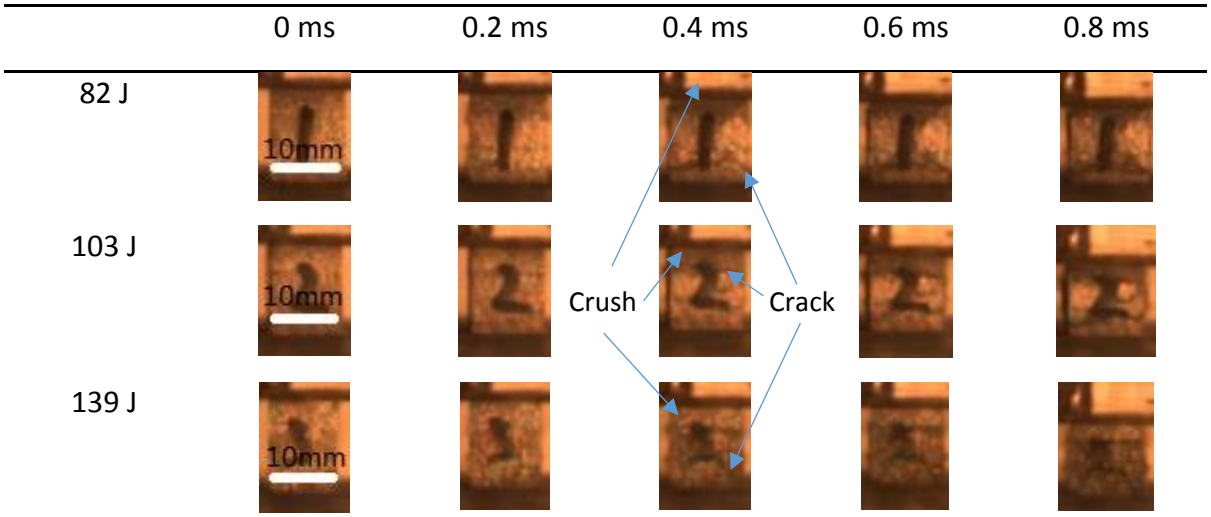

Figure 4.30 *First 5 frames acquired during impact of double-CM layered syntactic foam D6 under different impact energy levels*

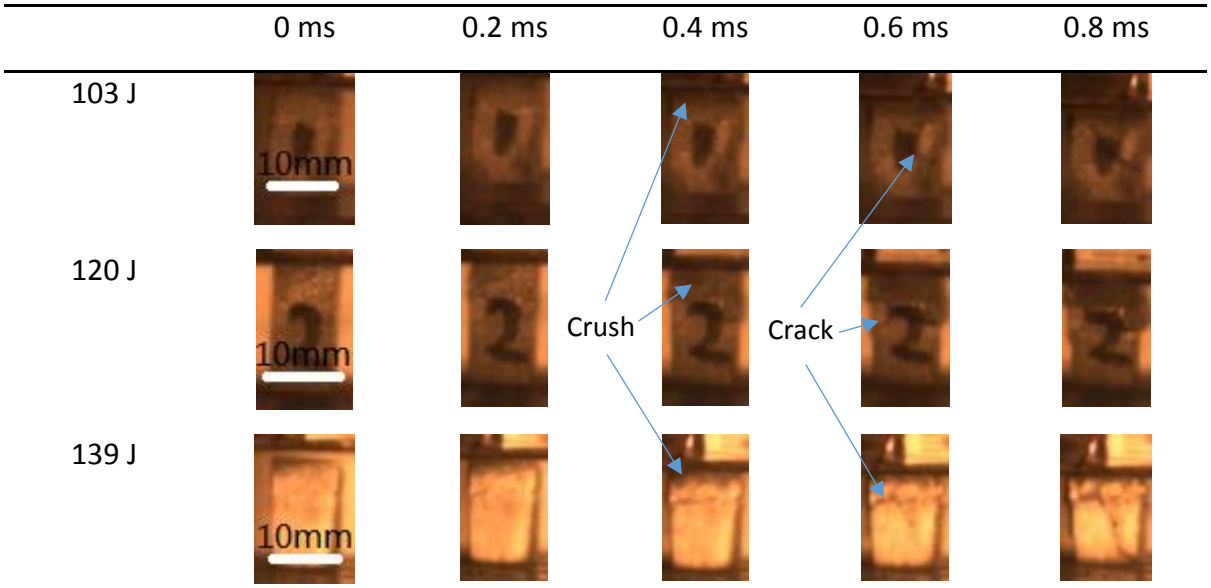

Figure 4.31 *First 5 frames acquired during impact of triple-CM layered syntactic foam T1-up under different impact energy levels*

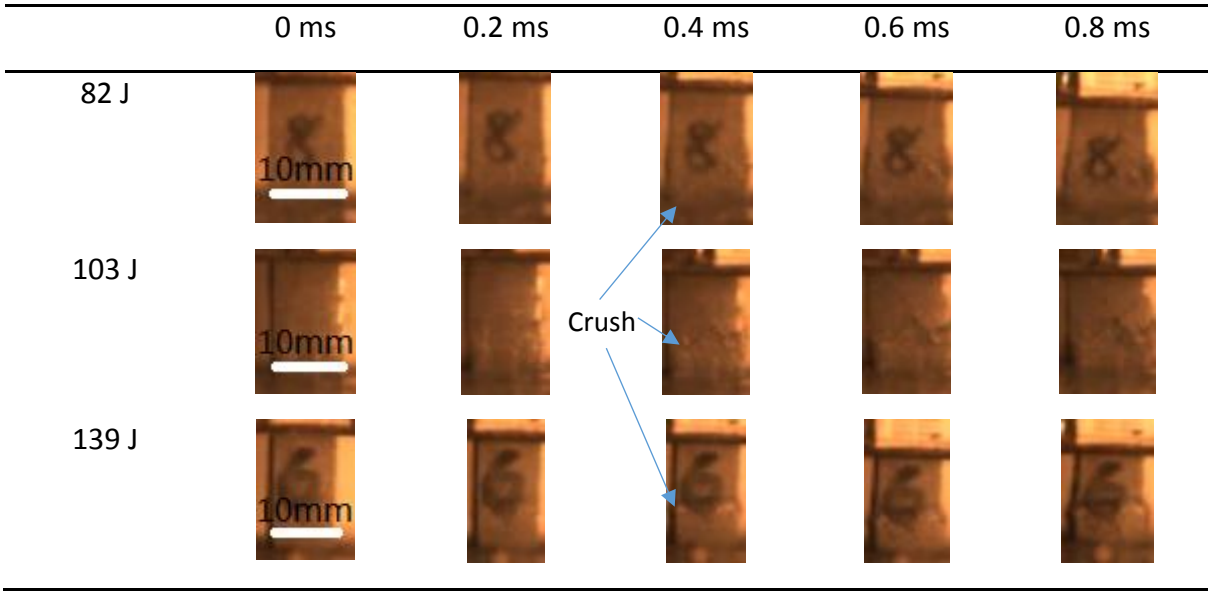

Figure 4.32 *First 5 frames acquired during impact of triple-CM layered syntactic foam T1-down under different impact energy levels*

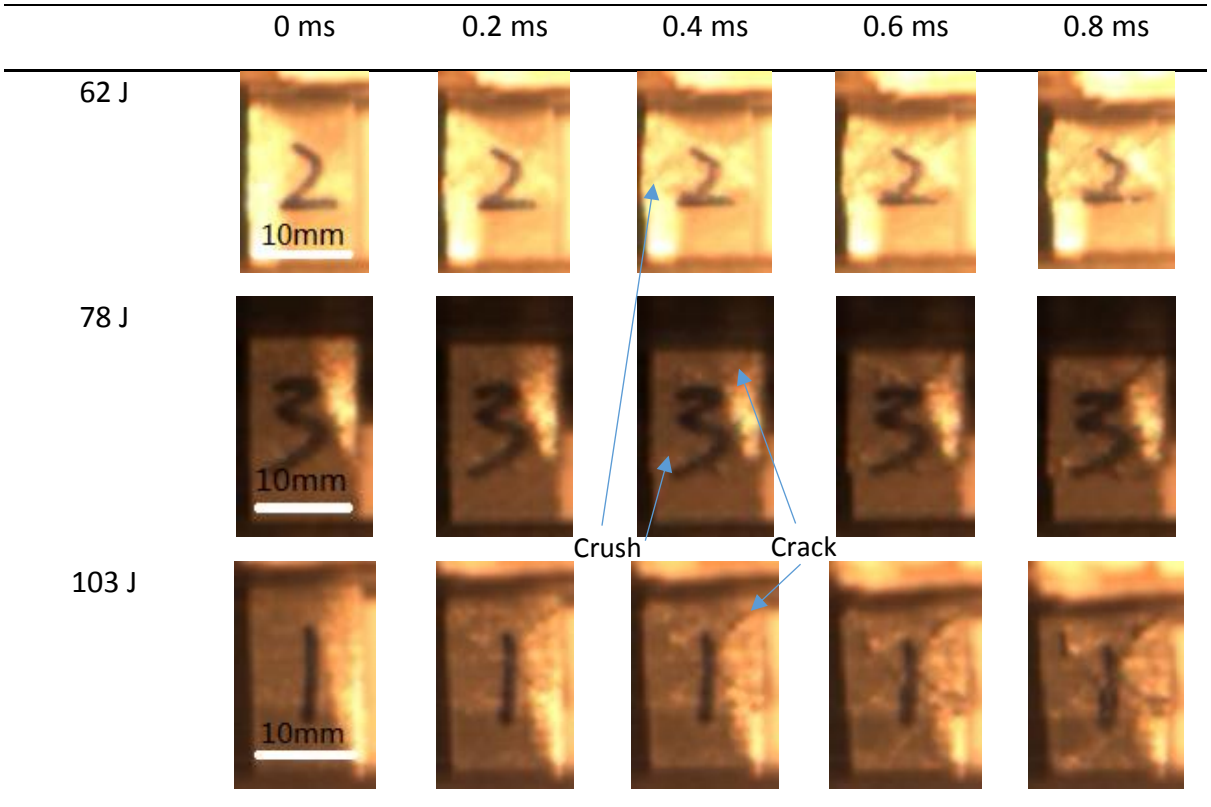

Figure 4.33 *First 5 frames acquired during impact of triple-CM layered syntactic foam T2 under different impact energy levels*

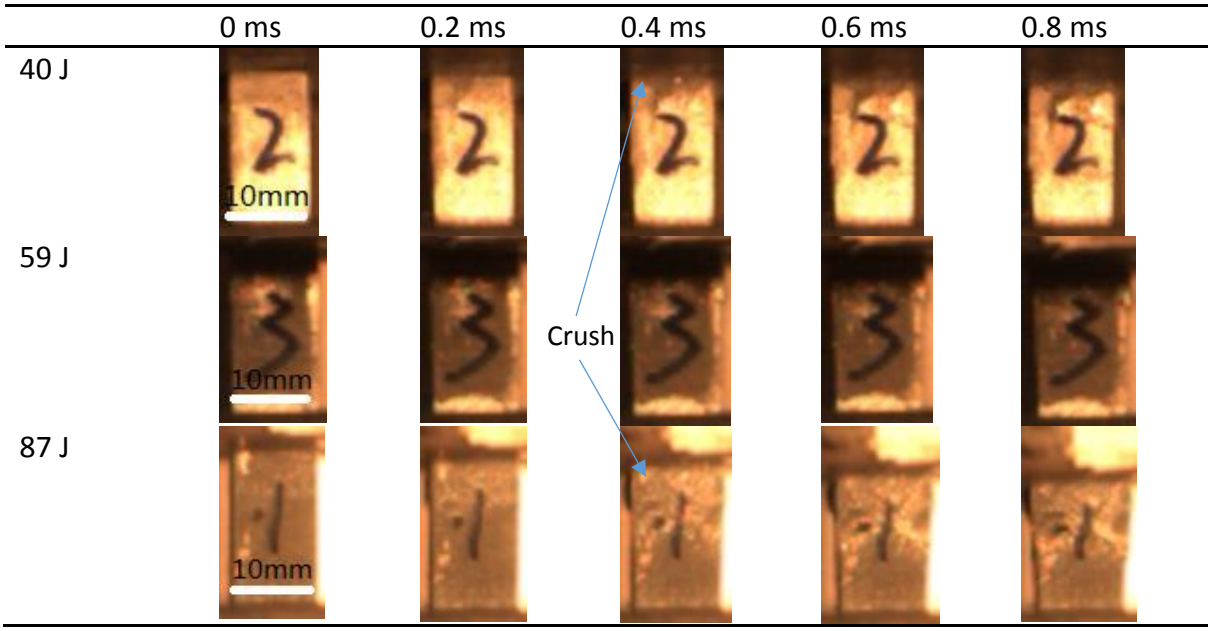

Figure 4.34 *First 5 frames acquired during impact of triple-CM layered syntactic foam T3 under different impact energy levels*

4.3.3 Impact loading response of mixed syntactic foams

4.3.3.1 Impact stress

Figures 4.35 and 4.36 show the typical impact stress-time traces of the fully mixed syntactic foams M1-M3 and partly mixed syntactic foams P1-P3 under different impact energy levels, respectively. The peak stress values for these samples are listed in Table 4.6. In M1 (25% L/75% S), the maximum peak stress appears at the end of the elastic region, i.e., at the first impact oscillation. Both the impact peak stress and the oscillation amplitude of each subsequent oscillation decrease gradually and level off near the end stage of impact. The sample was not densified at all three impact energy levels. In M2 (50% L/50% S), similar trend is shown under impact energy levels of 43 J and 63 J, where the samples were not densified. Under an impact energy of 82 J, densification occurred and then the stress increased. In M3 (75% L/25% S), stress also increased after densification. Partly mixed AMSFs P1-P3 had similar behaviour as fully mixed AMSFs, with increasing stress after densification.

Table 4.6 *Peak stress, maximum strain, densification time and specific energy absorption in impact test of mixed AMSFs under different impact energy levels*

Sample	Impact energy (J)	Peak stress (MPa)	Maximum strain	Time to reach densification (ms)	Specific energy absorption (J/g)
M1	43	200	0.3	-	23
	63	204	0.4	-	31
	82	211	0.5	3.5	41
M2	43	194	0.28	-	21
	63	201	0.34	-	31
	82	209	0.46	-	39
M3	43	130	0.33	-	18
	63	162	0.48	-	30
	82	172	0.6	2.7	25
P1	22	153	0.16	-	10
	43	196	0.35	-	21
	82	204	0.6	2.7	35
P2	43	136	0.28	-	21
	63	138	0.4	-	30
	83	175	0.46	-	41
P3	43	158	0.32	-	22
	63	205	0.4	-	31
	82	229	0.45	-	40

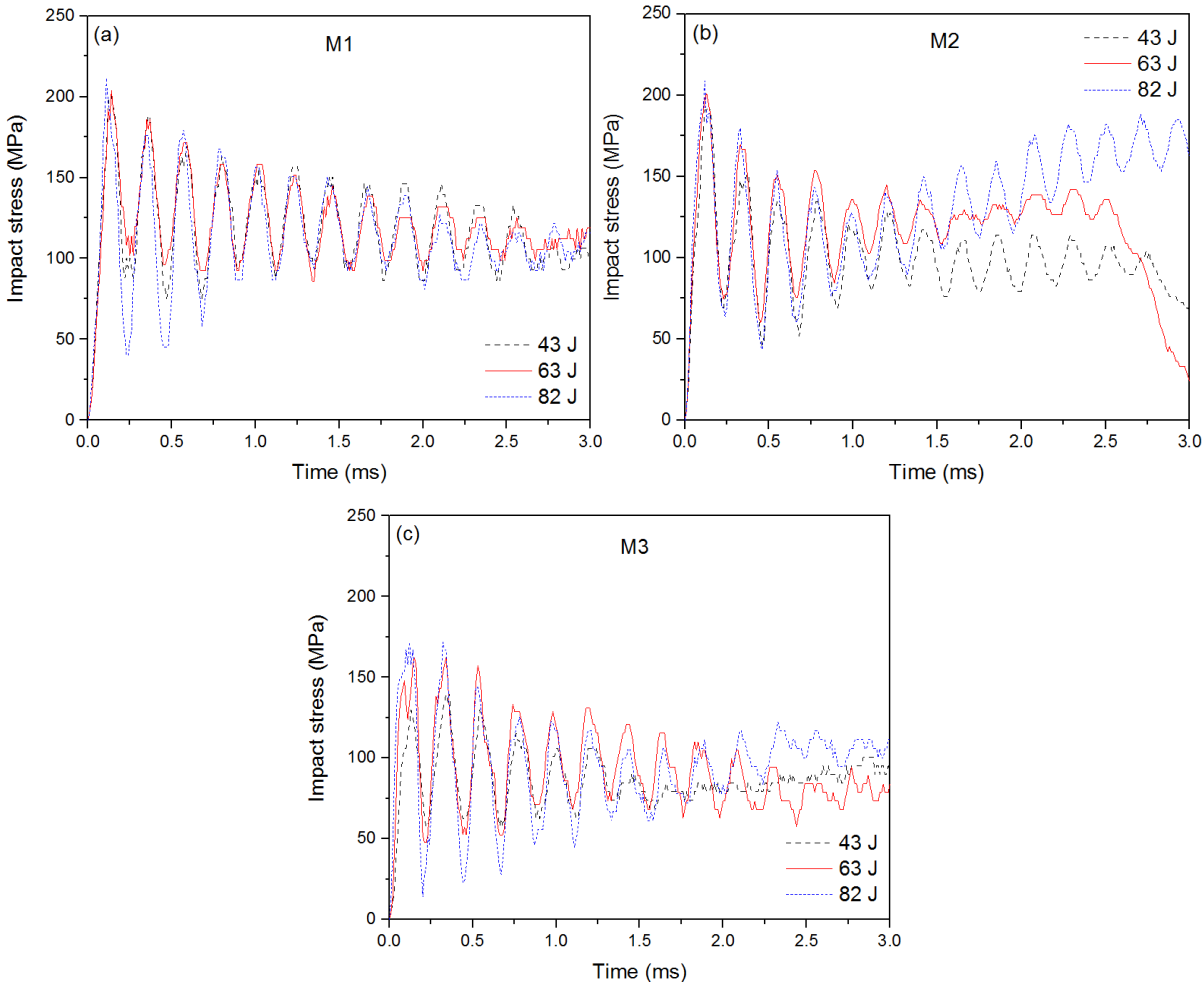

Figure 4.35 *Stress-time traces of fully mixed ASMFs (a) M1, (b) M2 and (c) M3 in drop-weight test at three different impact energy levels*

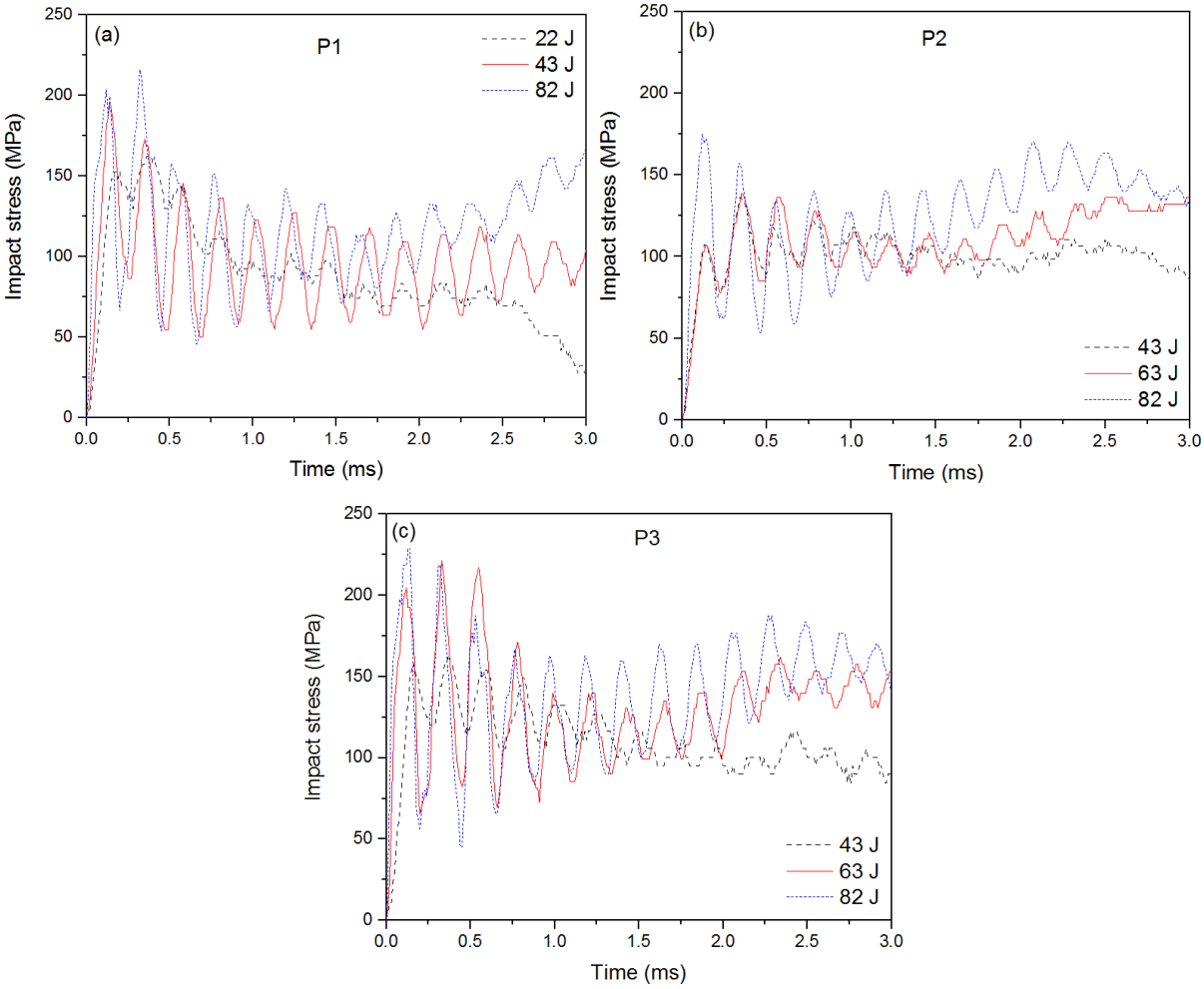

Figure 4.36 *Stress-time traces of partly mixed ASMFs (a) P1, (b) P2 and (c) P3 in drop-weight test at three different impact energy levels*

4.3.3.2 Impact strain

Figures 4.37 and 4.38 show the typical impact strain-time traces of the fully mixed syntactic foams M1-M3 and partly mixed syntactic foams P1-P3 under different impact energy levels, respectively. The maximum strain values for these samples are listed in Table 4.6. Generally, higher impact energy leads to higher impact strain. In M1 (25% L/75% S), the maximum impact strains are lower than 0.5 and the specimens are not densified under all three impact energy levels. In M2 (50% L/50% S), M3 (75% L/25% S) and the partly mixed AMSFs P1-P3, the specimens are not densified under 43 J and 63 J and barely densified under 82 J.

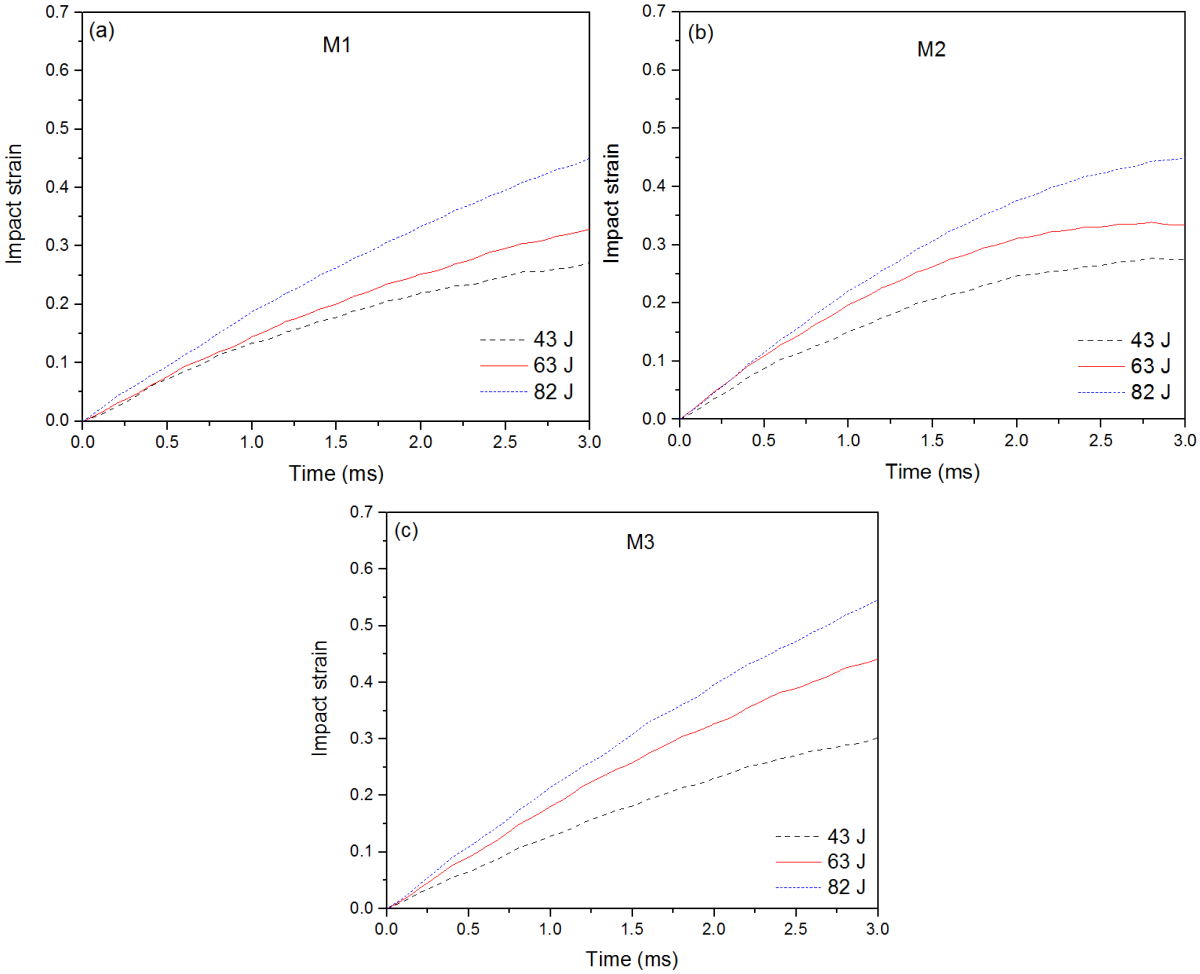

Figure 4.37 *Strain-time traces of fully mixed ASMFs (a) M1, (b) M2 and (c) M3 in drop-weight test at three different impact energy levels*

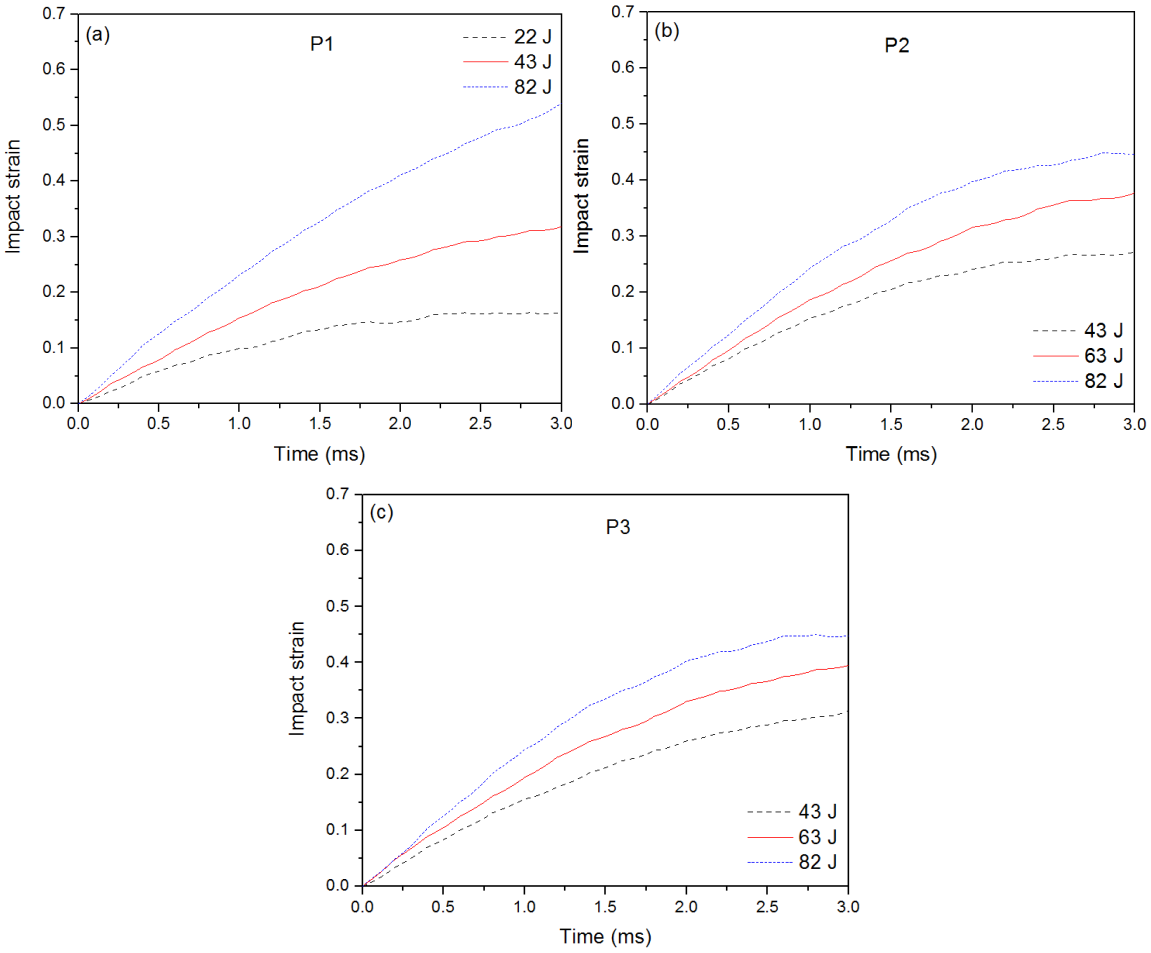

Figure 4.38 *Strain-time traces of partly mixed ASMFs (a) P1, (b) P2 and (c) P3 in drop-weight test at three different impact energy levels*

4.3.3.3 Impact velocity

Figures 4.39 and 4.40 show the typical impact velocity-time traces of the fully mixed syntactic foams M1-M3 and the partly mixed syntactic foams P1-P3 under different impact energy levels, respectively. Similar to uniform and layered samples, both fully and partly mixed syntactic foams show a generally decreasing velocity with time, with an approximately linear relation.

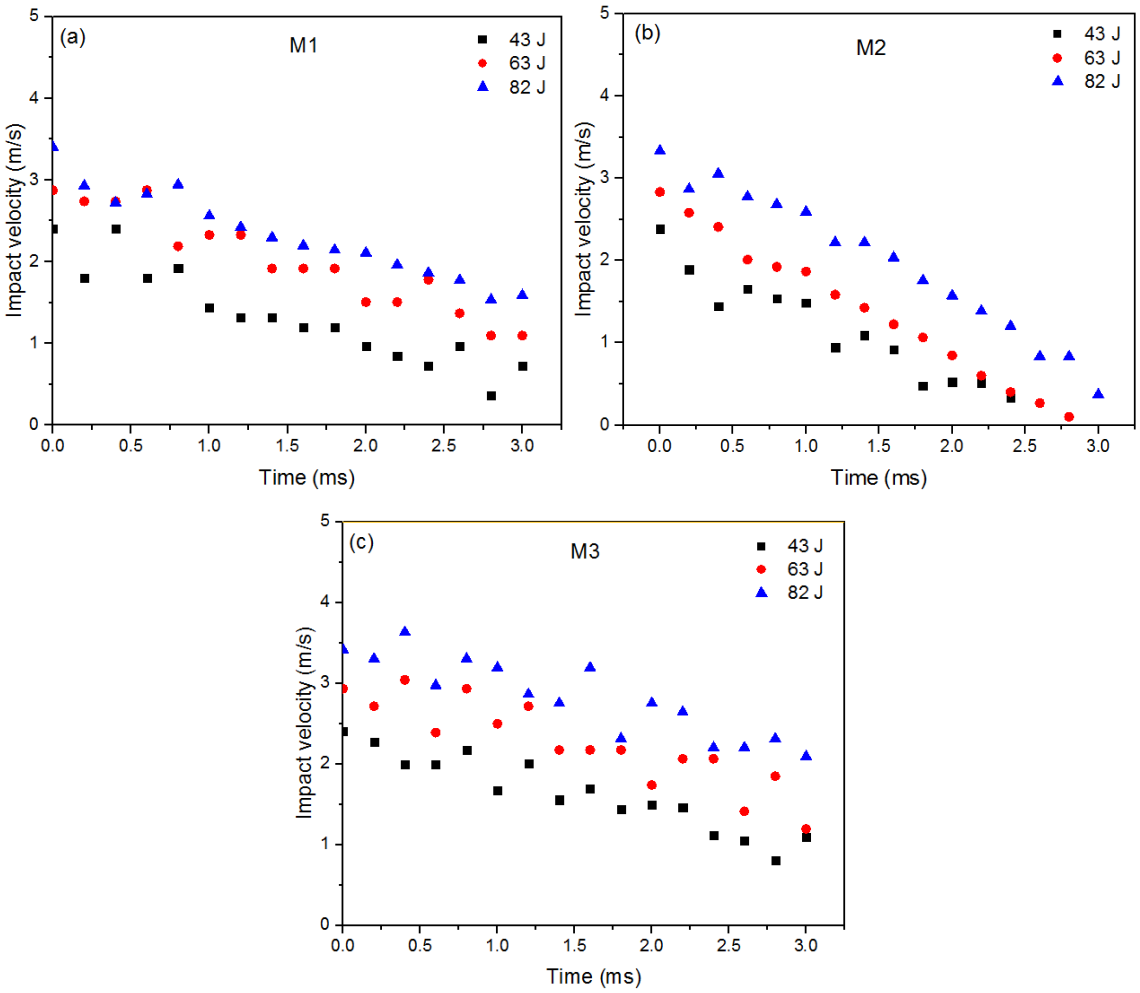

Figure 4.39 *Velocity-time traces of fully mixed ASMFs (a) M1, (b) M2 and (c) M3 in drop-weight test at three different impact energy levels*

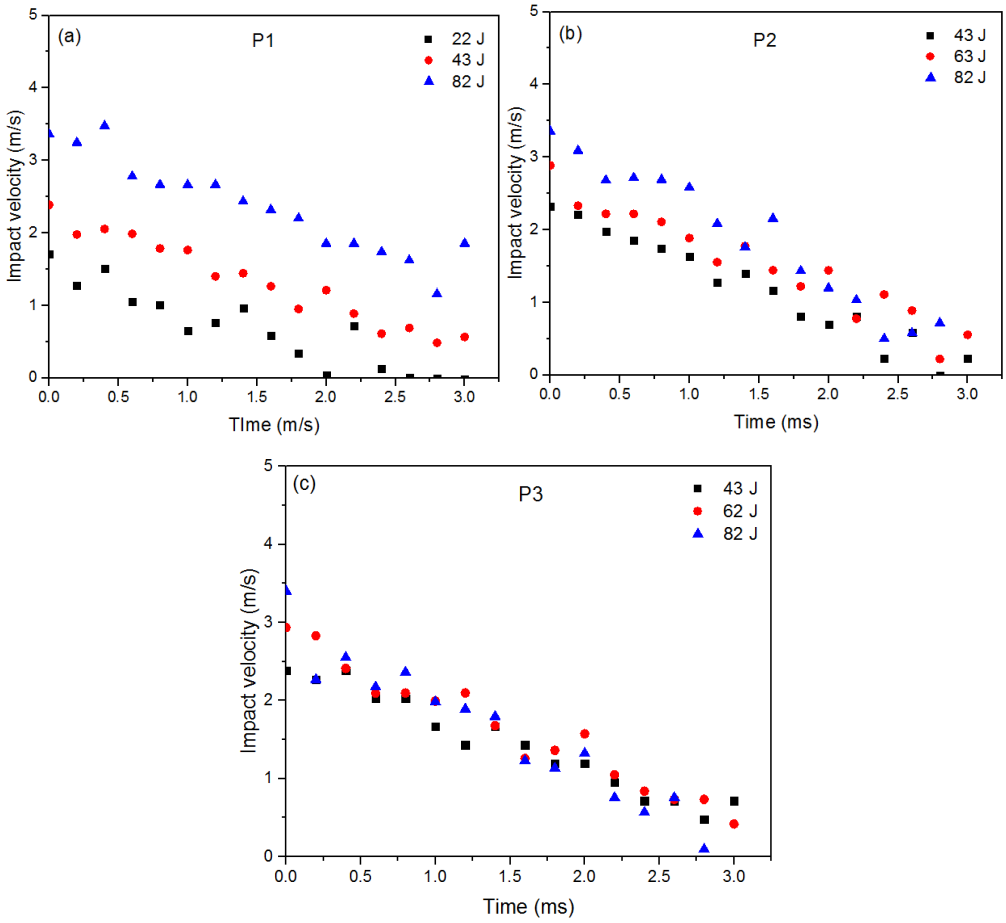

Figure 4.40 *Velocity-time traces of partly mixed ASMFs (a) P1, (b) P2 and (c) P3 in drop-weight test at three different impact energy levels*

4.3.3.4 Impact energy absorption

Figures 4.41 and 4.42 show the typical impact energy absorption-time relations for the fully mixed syntactic foams M1-M3 and partly mixed syntactic foams P1-P3 under different impact energy levels. The specific energy absorption values for these samples are listed in Table 4.6. Same as uniform and layered syntactic foams, the energy absorption response corresponds to the impact velocity response and increases with decreasing impact velocity. In M1 (25% L/75% S) and M2 (50% L/50% S), impact energy is all absorbed before densification under 43 J and 63 J. The specimens are just densified under the impact energy of 82 J. The M3 (75% L/25% S) specimens are not densified under all three impact energy levels. In all partly mixed

samples P1-P3, impact energy is absorbed before densification under all impact energy levels. Similar to uniform syntactic foams, mixed syntactic foams absorb more energy in impact than in quasi-static loading at the same strain.

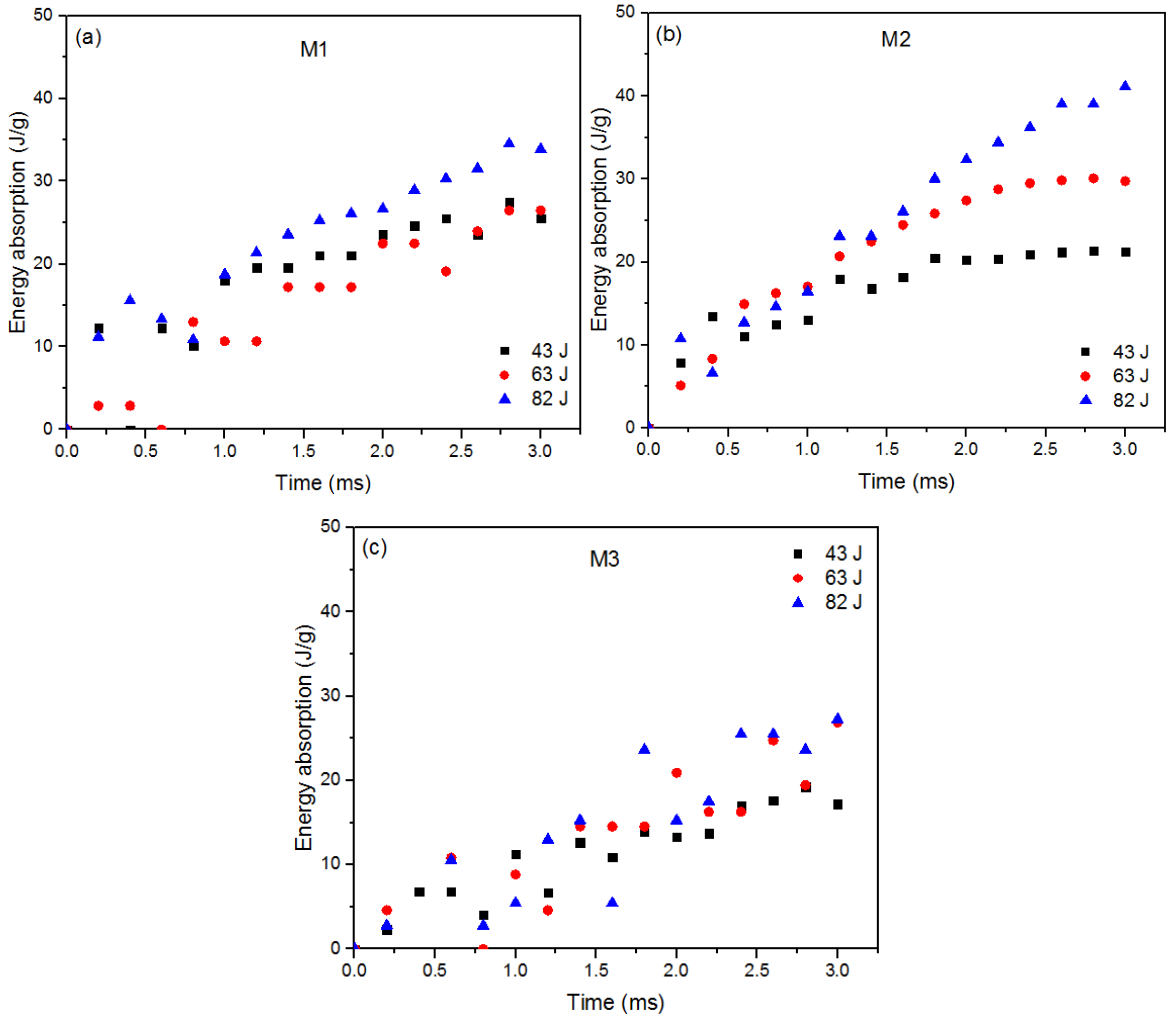

Figure 4.41 *Energy absorption-time traces of fully mixed ASMFs (a) M1, (b) M2 and (c) M3 in drop-weight test at three different impact energy levels*

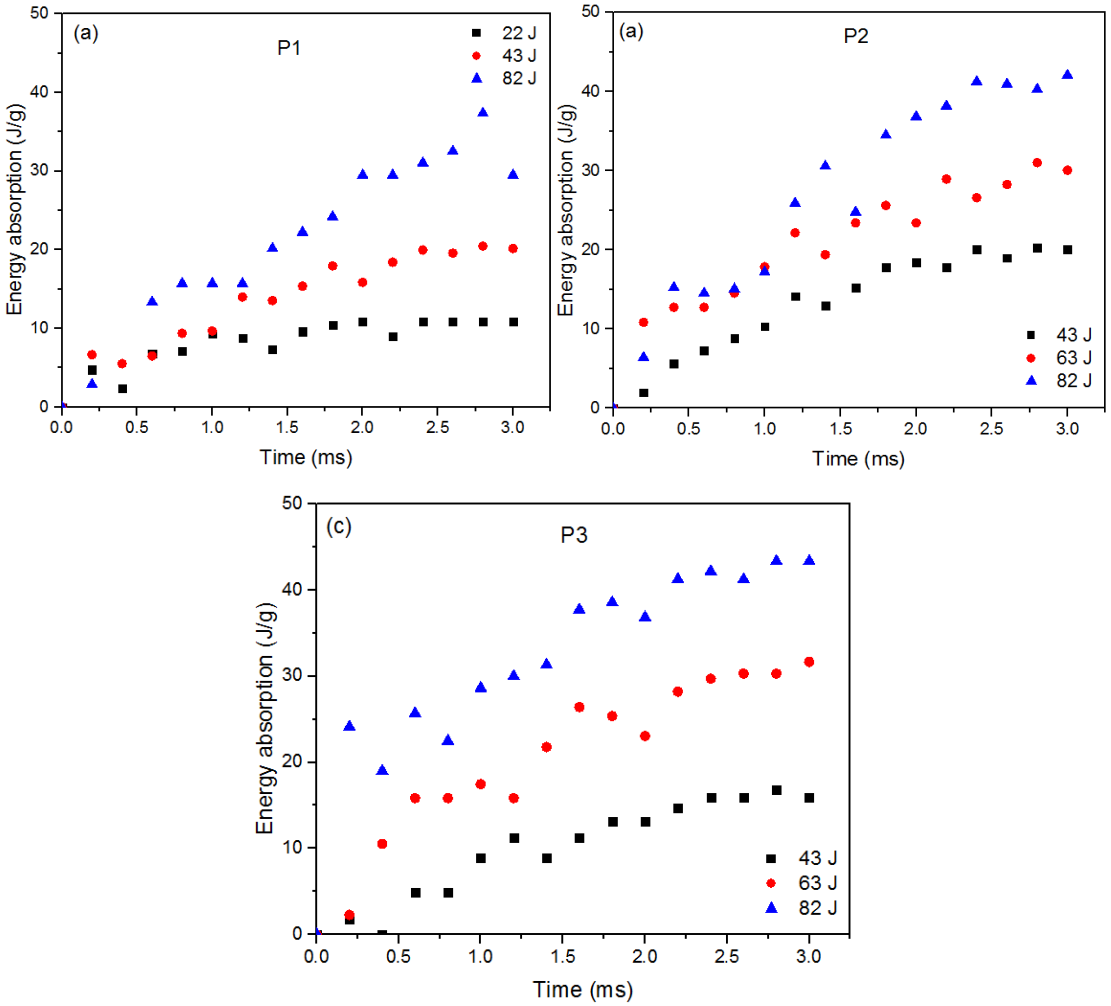

Figure 4.42 *Energy absorption-time traces of partly mixed ASMFs (a) P1, (b) P2 and (c) P3 in drop-weight test at three different impact energy levels*

4.3.3.5 Impact deformation

Figures 4.43-4.48 show the first 5 frames from images, acquired by a high speed camera, of fully mixed syntactic foams M1-M3 and partly mixed syntactic foams P1-P3 during impact under different impact energy levels. Similar to uniform and layered syntactic foams, three different fracture types were observed, with higher impact energy leading to brittle fracture and lower impact energy leading to ductile deformation. Ductile deformation was characteristic of crushing, while brittle fracture was in the form of crack propagation. Both crushing and cracking were observed in ductile-brittle deformation.

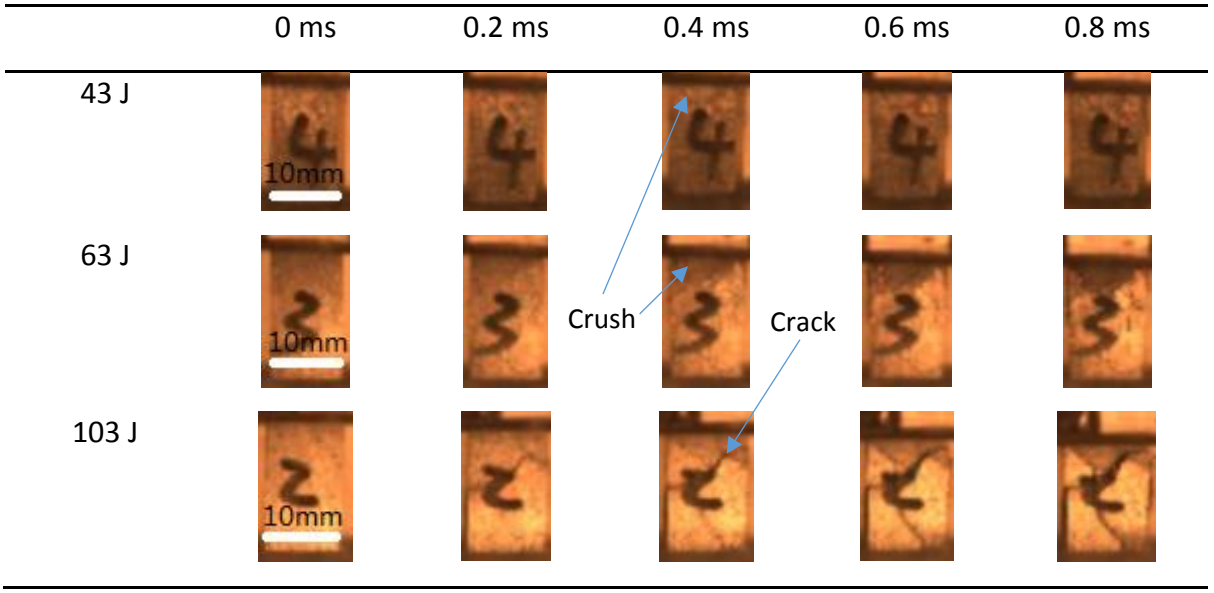

Figure 4.43 *First 5 frames acquired during impact of fully mixed syntactic foam M1 under different impact energy levels*

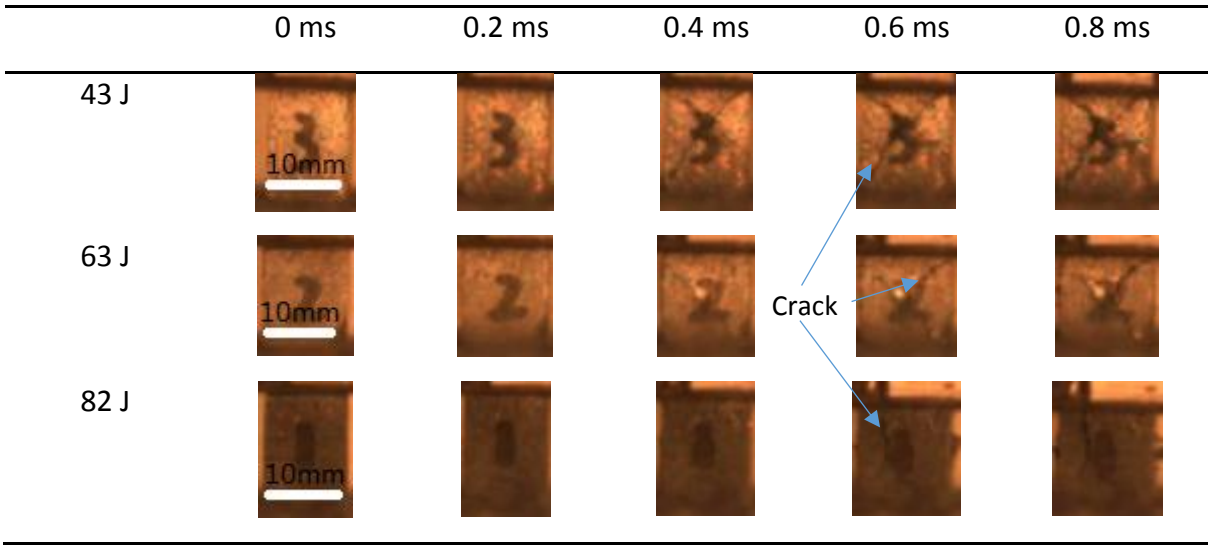

Figure 4.44 *First 5 frames acquired during impact of fully mixed syntactic foam M2 under different impact energy levels*

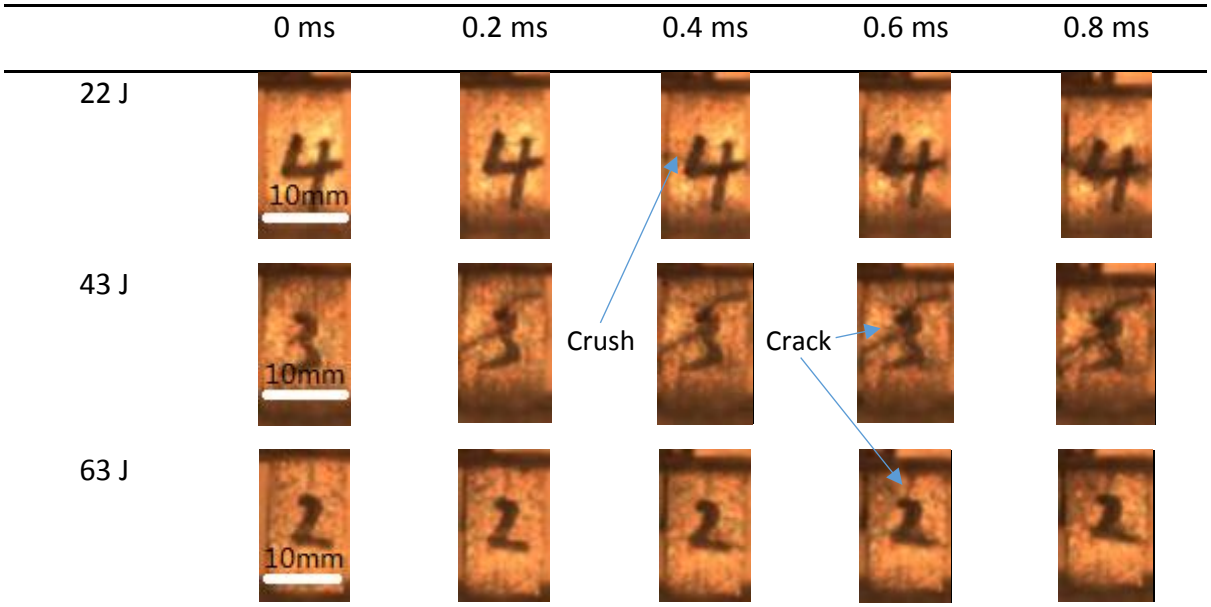

Figure 4.45 *First 5 frames acquired during impact of fully mixed syntactic foam M3 under different impact energy levels*

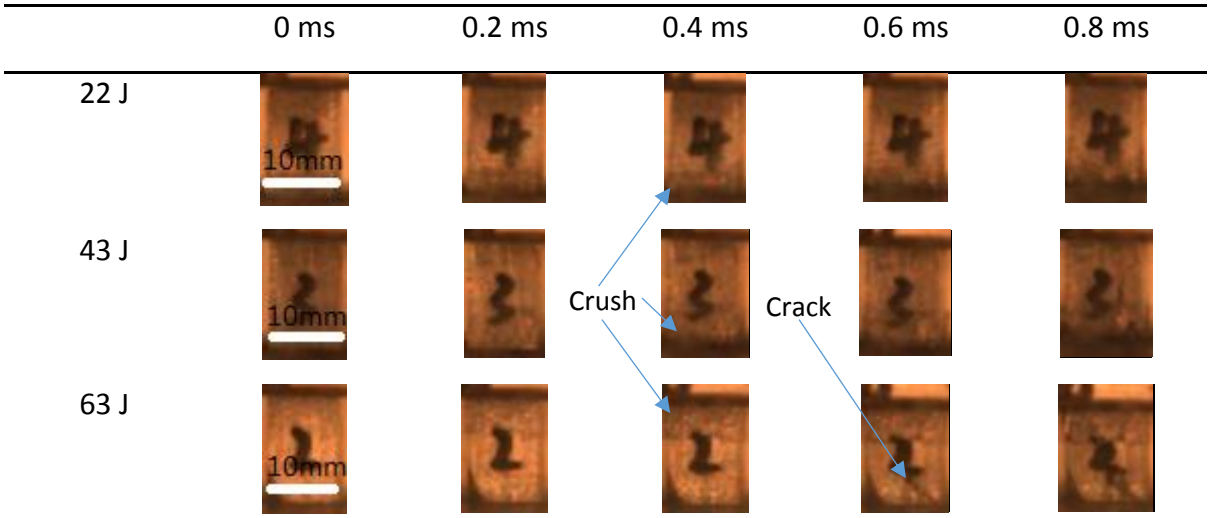

Figure 4.46 *First 5 frames acquired during impact of partly mixed syntactic foam P1 under different impact energy levels*

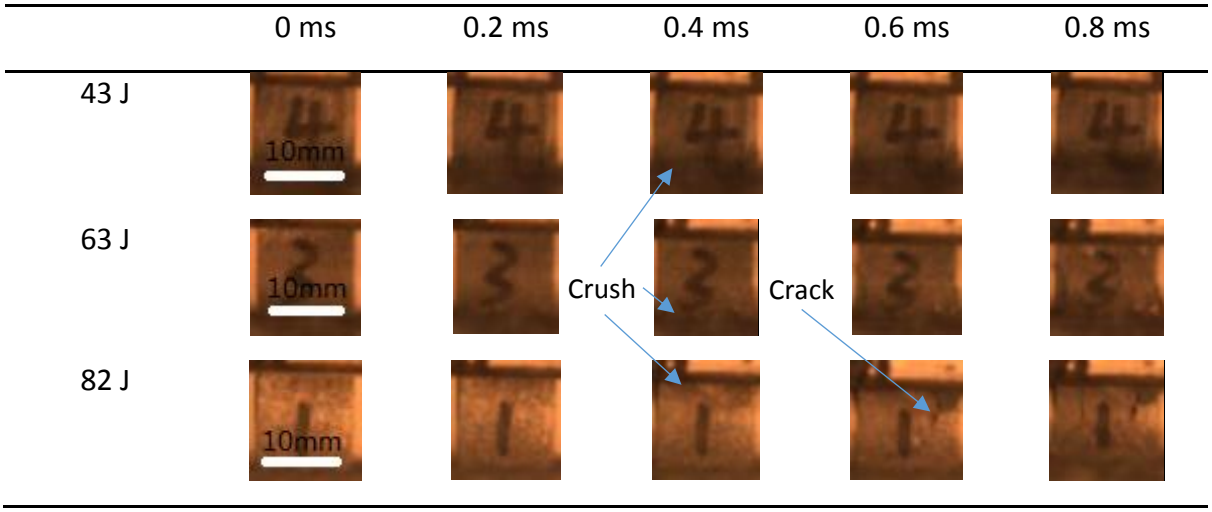

Figure 4.47 *First 5 frames acquired during impact of partly mixed syntactic foam P2 under different impact energy levels*

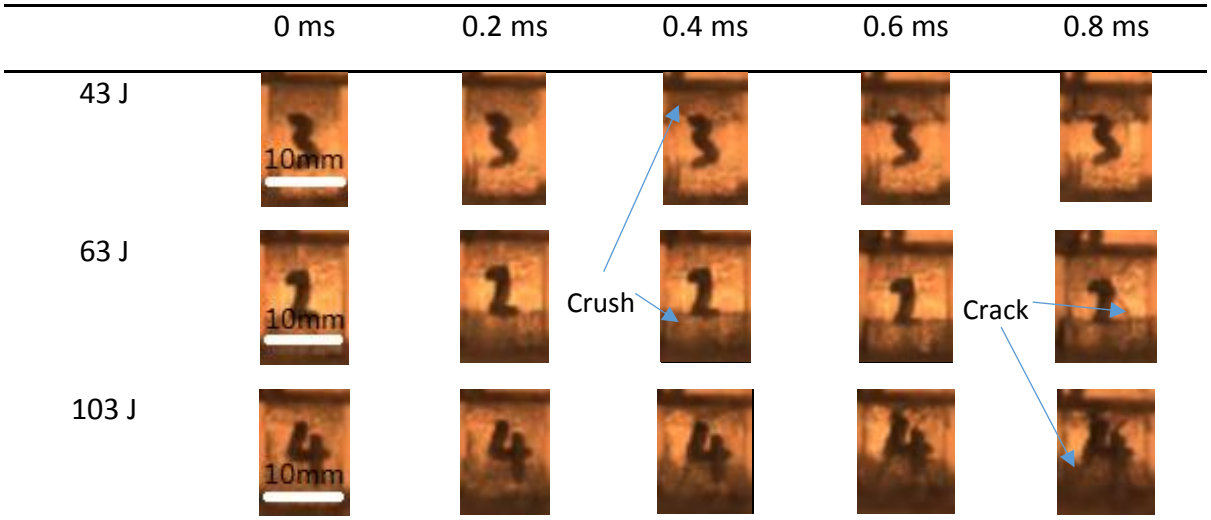

Figure 4.48 *First 5 frames acquired during impact of partly mixed syntactic foam P3 under different impact energy levels*

Chapter 5 Analytical modelling based on Impact Wave Propagation

This chapter presents an analytical model to estimate the stress-strain evolution in both uniform and layered AMSFs under impact loading. Based on impact theory (Johnson, 1972) on impact waves in materials, the inertia stress evolution in the AMSFs is simulated and the contact stress as a function of impact hammer velocity is calculated. Comparison between the sum of the predicted inertia stress and contact stress and the measured impact stress is carried out to evaluate the validity of the model. The model is used to explain the experimental results, including the high peak stress, the stress fluctuation, the effect of impact mass and velocity and the effect of impact direction.

5.1 Introduction to Impact Theory and analytical model

Impact loading generates movement of particles in materials (Johnson, 1972). Such movement includes elastic movement and plastic movement. The particles in materials do not move simultaneously, they move in sequence. The front of the movement of the particles, i.e. the boundary between the particles moved and the particles not yet moved, is defined as impact wave. There are elastic wave and plastic wave. The speed of particles and stress in the specimen remain unchanged until the impact wave has passed. When impact wave hits the edge of the specimen, it bounces back into the specimen. A new cycle starts every time impact wave bounces. Impact wave front represents the boundary between particles moved and particles not yet moved, or sudden change in speed and stress due to the impact wave.

Fig. 5.1 shows schematic diagrams of impact wave propagation. After an impactor hits the specimen (Fig. 5.1 (a)), an elastic wave c_0 and a plastic wave c_1 are generated. The region passed by c_0 is stressed elastically, the region passed by c_1 is deformed plastically, and the region passed by neither remains static, as shown in Fig. 5.1 (b). When the elastic wave hits the bottom of specimen after a time of h_0/c_0, the plastic wave is still in the middle of the sample due to a lower speed, as shown in Fig. 5.1 (c) and (d). Afterwards, the elastic wave bounces back and turns into a plastic wave (Fig. 5.1 (e)). Now there are two plastic waves with opposite directions. If the speed of elastic wave is significantly higher than the speed of plastic wave, the time the elastic wave takes to travel to the bottom is negligible. It can be assumed that two plastic waves are generated simultaneously from both ends of the specimen. It takes a time of h_0/c_1 for each plastic wave to reach the other end of the specimen, as shown in Fig. 5.1. (f). After the two plastic waves reach the ends, they bounce back in a new cycle with similar behaviour.

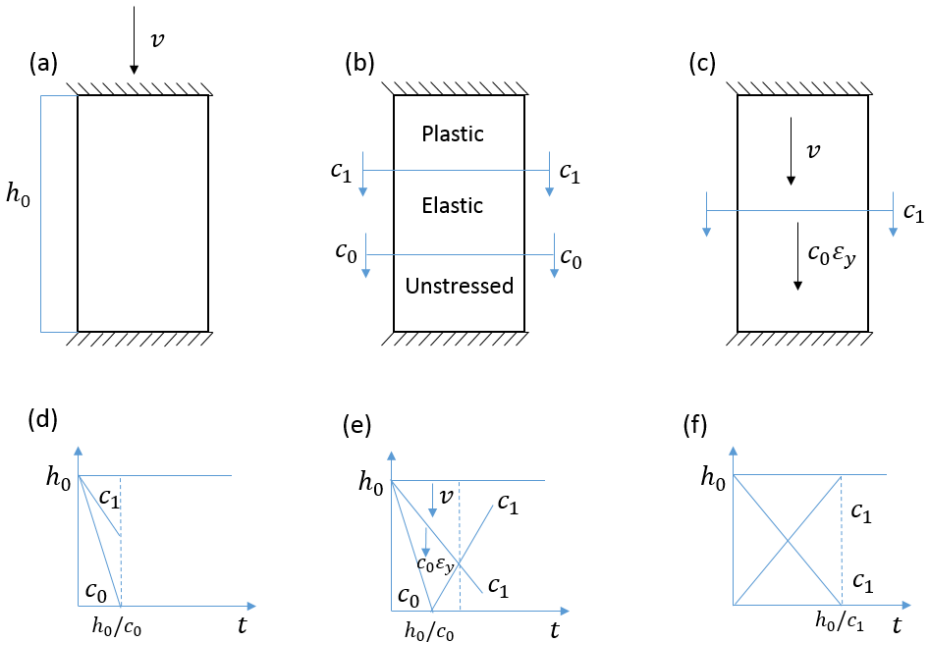

***Figure** 5.1 Schematic diagrams of impact wave propagation: (a) impact loading on specimen, (b) elastic and plastic wave generated, (c) elastic wave hitting the bottom, (d) wave propagation when elastic wave hits the bottom, (e) wave propagation when two plastic waves meet, (f) simplification wave propagation in two plastic waves*

5.2 Impact wave-based analytical model for AMSF

When a projectile or hammer impacts a specimen, it accelerates the specimen and thus generates inertia forces in the specimen (Pham *et al.* 2018). Meanwhile, a contact force is generated at the impact end, where the hammer contacts the specimen, due to the acceleration of the hammer. Rieder and Mindess (1998) showed that there is a difference between the contact force and the force measured at the base of the specimen. They recommended that the impact force should be measured at the base of specimens and this suggestion was adopted by a previous study (Xu *et al.* 2012). The impact force in this study was measured by a load cell placed at the base of the specimen and is termed as base force. The base force is equal to the contact force plus the sum of the inertia forces. In this work, the inertia force is calculated based on Johnson's theory (1972) while the contact force is calculated from the velocity change of the impact hammer.

5.2.1 Model formulation

Let us consider an AMSF specimen with an initial height h_0, situated on a frictionless flat rigid die and subjected to compression by an upper die of mass M, moving with an initial speed v_0, as shown in Fig. 5.2 (a). Based on the compressive stress-strain curves of the AMSF specimens in Chapter 4, the AMSF can be assumed to be an ideal elastic-linear strain-hardening material with yield stress σ_y, elastic modulus E and plastic modulus P, as shown schematically in Fig. 5.2. According to the impact theory (Johnson, 1972), impact loading creates an elastic wave c_0 and a plastic wave c_1 in the specimen; these two waves propagate inside the specimen as shown in Fig. 5.2 (b). The speeds of elastic and plastic waves are:

$$c_0 = \sqrt{\frac{E}{\rho}}; c_1 = \sqrt{\frac{P}{\rho}} \tag{5.1}$$

where ρ is the density of the specimen, which changes in the case of a porous material as plastic deformation proceeds.

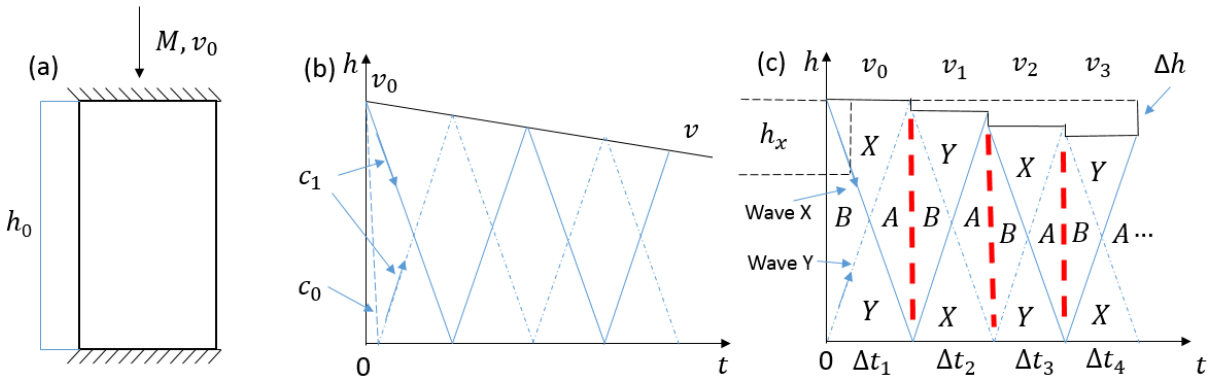

Figure 5.2 *Impact waves inside an AMSF specimen under impact, (a) schematic of impact, (b) impact wave and impact velocity evolution, and (c) simplified impact wave evolution model*

All the AMSF specimens in this work have a similar elastic modulus *E* (≈3 GPa) and plastic modulus *P* (≈0.02 GPa), with only yield stress σ_y being different (60 – 120 MPa). For simplicity, we can assume that the elastic modulus and plastic modulus are constant and independent of the specimens. The elastic modulus *E* is significantly higher than the plastic modulus *P*. As a consequence, the elastic wave speed, c_0, is nearly one order of magnitude higher than the plastic wave speed, c_1. We can neglect the time the elastic wave travels from the top to the bottom of the specimen and assume that two plastic waves emerge simultaneously from both sides of the specimen at the outset of impact.

Stress-strain evolution in the specimen is a result of the propagation of the two plastic waves, designated as wave X and wave Y, as shown in Fig. 5.2 (c). In each cycle when the two waves travel from one end to the other, four different stress zones can be identified in the specimen:

before the waves pass (zone B), passed by wave X (zone X), passed by wave Y (zone Y) and after both waves passed (zone A). The stresses in these four zones can be determined from the yield stress of the material, the elastic wave speed, the plastic wave speed and the impact velocity, using a set of equations well defined by the Johnson's theory. When the waves reach the end of the specimen, they bounce back and travel to the other end. The same four zones can be identified in this new cycle, each accompanied by a stress increase. This process is repeated for a number of cycles until the impact energy is consumed and the impact velocity, or hammer velocity, is reduced to zero.

An explicit analytical solution of the stress evolution during impact is only possible if the impact velocity remains constant. In practical impact tests, however, the impact velocity decreases with time as the kinetic energy of the hammer is gradually absorbed by the AMSF specimen. Fortunately, the plastic wave speed ($c_1 \approx$ 108 m/s) is significantly higher than the impact velocity ($v_0 \approx$ 1.7-4.3 m/s). We can neglect the change in impact velocity and the change in strain within one cycle when the plastic waves travel from one end to the other and assume a step change in the impact velocity and a step change in the strain from one cycle to the next. The wave propagation process can be split into discrete steps, marked as time periods Δt_1, Δt_2, Δt_3, etc., as shown in Fig. 5.2c. Each step represents one cycle and corresponds to plastic waves traveling the specimen length from one end to the other. While the impact velocity, specimen length, density, stress and strain change from one cycle to the other, they are considered constant within each cycle and can be calculated analytically.

5.2.2 Stress-strain evolution inside the specimen

Up to three stress zones are produced in the specimen at any one time with the propagation of the waves, namely zone X, zone Y and the middle zone, as shown in Fig. 5.2c. The middle zone is designated as zone B before the two plastic waves pass and as zone A after both waves have passed. In zone B, a stress equal to the yield stress of the specimen is produced instantly when the elastic wave travels from top to bottom. In zone X, an additional stress is generated by the plastic wave X. Similarly, an additional stress is generated by the wave Y in zone Y, but with a different magnitude from zone X due to different wave direction to the impact. In zone A, a cumulative additional stress is generated by the two plastic waves. When each wave bounces back at the top or bottom edge of the specimen, it creates a stress increment. As a result, the stress in each zone is increased successively in the following cycles of wave propagation.

Based on the impact theory for the constant impact velocity case (Johnson, 1972), the stresses in the different zones in the first cycle of wave propagation can be expressed as follows:

$$\begin{cases} \sigma_{X(1)} = \sigma_y \left(1\text{-}\frac{c_1}{c_0}\right) + \rho_0 c_1 v_0 = \sigma_y \left(1\text{-}\sqrt{\frac{P}{E}}\right) + \sqrt{\rho_0 P} v_0 \\ \sigma_{Y(1)} = \sigma_y \left(1\text{+}\sqrt{\frac{P}{E}}\right) \\ \sigma_{B(1)} = \sigma_y \\ \sigma_{A(1)} = \sigma_y + \sqrt{\rho_0 P} v_0 \end{cases} \tag{5.2}$$

where σ_X, σ_Y, σ_B and σ_A are the stresses in zones X, Y, B and A, respectively, ρ_0 is the initial density of the specimen before any plastic deformation, and the subscript 1 in brackets indicates the first cycle in the time period Δt_1.

Taken into account the change in impact velocity between adjacent cycles, the stress in each zone in the current cycle of wave propagation is increased by a fixed amount from the previous cycle and can be obtained as follows:

$$\sigma_{z(n)} = \sigma_{z(n-1)} + \sqrt{\rho_{n-1} P} v_{n-1} \tag{5.3}$$

where *z* designates the zone, i.e., X, Y, A or B, the subscript *n* in brackets indicates the n^{th} cycle of wave propagation, (*n-1*) indicates the previous cycle, ρ_{n-1} is the density of the specimen in the previous cycle and v_{n-1} is the impact velocity in the previous cycle. *n* can also be understood as the number of times each plastic wave has travelled through the full length of the specimen forwards and backwards.

According to the idealised mechanical behaviour of the AMSFs shown in Fig. 5.3, the strain in each zone can be easily obtained from the stress by:

$$\varepsilon_z = \frac{\sigma_z - \sigma_y}{P} \tag{5.4}$$

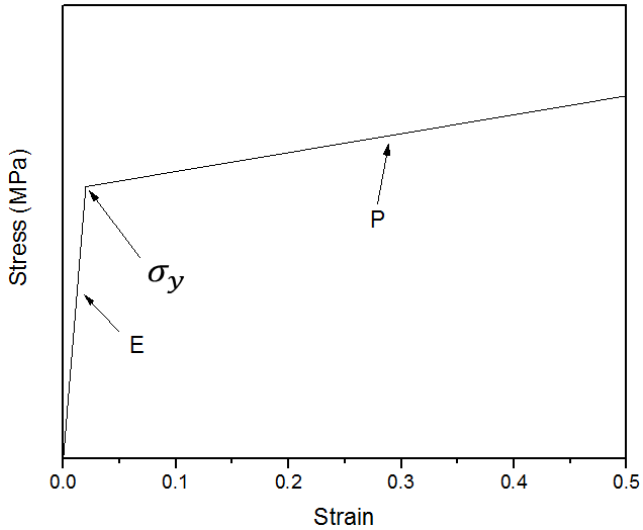

Figure 5.3 *Idealised mechanical behaviour of AMSFs, indicating yield stress σ_y, elastic modulus E and plastic modulus P*

where ε_z and σ_z are the strain and stress in zone *z*, with *z* being X, Y, B or A. The strain in each zone is manifested in a displacement, which depends on the size of the zone. The total strain of the specimen at any time can be calculated from the cumulative displacements from all the zones present at this particular time by:

$$\begin{cases} \varepsilon = \frac{h_X\varepsilon_X + h_Y\varepsilon_Y + h_B\varepsilon_B}{h_0} & (0 \le t \le \frac{\Delta t}{2}) \\ \varepsilon = \frac{h_X\varepsilon_X + h_Y\varepsilon_Y + h_A\varepsilon_A}{h_0} & (\frac{\Delta t}{2} < t < \Delta t) \end{cases} \tag{5.5}$$

where h_X, h_Y, h_B and h_A, are the unstrained heights of each zone, ε_X, ε_Y, ε_B and ε_A are the strains of zones X, Y, B and A, respectively, *h* is the height of the specimen in the current cycle, *t* is the time of wave propagation from the onset of the current cycle, and Δt is the duration of the current cycle. The heights of the respective zones change with time in each cycle as follows:

$$\begin{cases} h_X = h_Y = c_1 t;\ h_B = h - 2c_1 t & (0 \le t \le \frac{\Delta t}{2}) \\ h_X = h_Y = h - c_1 t;\ h_A = 2c_1 t - h & (\frac{\Delta t}{2} < t < \Delta t) \end{cases} \tag{5.6}$$

The height of the specimen, *h*, the density of the specimen, ρ, the duration of the wave propagation cycle, Δt, and the impact velocity, *v*, change from cycle to cycle. The change in the height of the specimen between two successive cycles is the distance travelled by the hammer, so the height of the specimen in the current cycle can be calculated from the height in the previous cycle by:

$$h_n = h_{n-1} - v_{n-1}\Delta t_{n-1} \tag{5.7}$$

The duration, or time period, of the wave propagation cycle is simply:

$$\Delta t_{n-1} = \frac{h_{n-1}}{c_{1(n-1)}} = h_{n-1}\sqrt{\frac{\rho_{n-1}}{P}} \tag{5.8}$$

The decrease in impact velocity is due to the kinetic energy of the hammer being consumed by the plastic deformation of the AMSF specimen. In each cycle, the energy conversion can be expressed by:

$$\frac{1}{2}Mv_{n-1}^2 - \frac{1}{2}Mv_n^2 = A\left(\frac{\sigma_{B(n-1)}+\sigma_{A(n-1)}}{2}\right)v_{n-1}\Delta t_{n-1} \tag{5.9}$$

where *A* is the cross sectional area of the specimen. The left hand side of Eq. (5.9) is the kinetic energy loss of the hammer in a cycle. The right hand side is the energy absorbed by the plastic deformation in the cycle, which is equal to the product of the force and displacement in the specimen. It should be noted that the stress in the specimen in a cycle is not constant but changes from σ_B at the beginning to σ_A at the end of the cycle, so the average stress is used in determining the energy absorbed.

Re-arranging Eq. (5.9) gives the impact velocity of the current cycle as:

$$v_n = \sqrt{v_{n-1}^2 - \frac{A\left(\sigma_{B(n-1)}+\sigma_{A(n-1)}\right)v_{n-1}}{M}} \tag{5.10}$$

As the plastic deformation of a porous material is associated with the collapse of pores, the cross sectional area of the specimen does not change when the height of the specimen changes during plastic deformation. The density of the specimen is therefore inversely proportional to specimen height and can be calculated by:

$$\rho_n = \rho_{n-1}\frac{h_{n-1}}{h_n} \tag{5.11}$$

5.2.3 Base stress based on inertia stress and contact stress

When a specimen is subjected to the impact of a hammer on the top, as shown in Fig. 5.2 (a), a contact stress is generated on the top of the specimen by the hammer and an inertia stress

is induced inside the specimen due to the elastic and plastic waves. There is a difference between the contact stress at impact and the stress transmitted through the specimen to the base (Rieder et al., 1998). The transmitted stress exerted on the supporting base, or base stress, is the sum of the contact stress, σ_c, and the total inertia stress, σ_i:

$$\sigma_b = \sigma_c + \sigma_i \tag{5.12}$$

The contact stress occurring at the hammer-specimen interface is proportional to the deceleration and can be estimated from the velocity change of the impact hammer by:

$$\sigma_c = \frac{M}{A}\frac{\Delta v}{\Delta t} \tag{5.13}$$

where Δv is the velocity change between two adjacent cycles, which can be calculated from Eq. (5.10), and Δt is the cycle time, which can be calculated from Eq. (5.8).

The inertia stress is caused by the moving particles in the specimen. The moving particles are confined to the zones behind the plastic waves, i.e., zones X and Y only. Neither of the two plastic waves has reached zone B and the two opposing waves have both passed zone A, so the particles in zones B and A are stationery. Therefore, the inertia stress is the sum of the height-weighted stresses in zones X and Y, relative to the initial specimen height. Given that the heights of zones X and Y are symmetric, the total inertia stress is:

$$\sigma_i = \frac{h_X(\sigma_X+\sigma_Y)}{h_0} \tag{5.14}$$

5.2.4 Considerations for layered AMSFs

In the layered AMSFs, the individual layers (L, M and S) have a very similar density and plastic modulus, so the plastic waves in these individual layers have nearly the same propagation velocity. Consequently, the impact wave propagation in layered AMSF structures consisting of different layers is the same as that in homogeneous AMSF structures. The plastic waves in a layered AMSF specimen also propagate through the whole length of the specimen and reverberate in a cyclic manner, as shown in Fig. 5.2 (c). However, the individual layers (L, M and S) in a layered AMSF specimen have different yield stresses and will experience different stresses and therefore have different strains during impact. The amounts of plastic deformation in the layers in each cycle are small relative to the specimen height. The ratios of the layer thicknesses can be considered to remain the same during the impact. The analytical model developed for uniform structures can be applied directly to layered structures. The contact stress, inertia stress and base stress can be calculated in the same way, except local yield stress replacing global yield stress.

5.3 Predictions and comparisons with experimental results

In this work, we have uniform AMSFs, layered AMSFs and mixed AMSFs. Experimentally, mixed AMSFs behave same way as uniform AMSFs. With same elastic modulus and plastic modulus in all layers L, M and S, mixed AMSFs are regarded same as uniform AMSFs, only different yield stress. Therefore, in this section, we only compare theoretical results and experimental results among some uniform and layered AMSFs as examples for the analytical model proposed.

5.3.1 Stress evolution predictions

The theoretical results for the evolutions of the contact stress, inertia stress and base stress in the uniform AMSFs U1 and U3, subjected to an impact energy of 80 J, are shown in Fig. 5.4 and Fig. 5.5, respectively. In the experiments, the impact stress was measured at the bottom of the specimen. It is equivalent to the base stress in Eq. (5.12), which is composed of the contact stress and the inertia stress. The contact stress is caused by the deceleration of the hammer or change of impact velocity (Eq. 5.13), which increases with time. As a consequence, the contact stress increases with time (Fig. 5.4 (a) and Fig. 5.5 (a)). The contact stress is sensitive to the yield stress of the material, hence the significant difference between specimens L and S. The inertia stress fluctuates because it is proportional to the height of zones X and Y (Eq. 5.14). In each impact cycle, it increases from zero at the outset to the maximum at the midpoint and then decreases to zero at the end of the cycle (Fig. 5.4 (b) and Fig. 5.5 (b)). This fluctuating inertia stress results in the fluctuation in the base stress and hence the experimentally measured stress. U3 has higher inertia stress than specimen L because the former has a higher yield stress.

The theoretical predictions agree reasonably well with the experimental results (Fig. 5.4 (c) and Fig. 5.5 (c)), especially for U1. The analytical model captures the key characteristics of stress fluctuation with fairly accurate predictions of time period and reasonable estimation of stress range of fluctuation. The considerable deviation in the fluctuation stress range for specimen S is due to its higher degree of brittleness. The analytical model assumes that the specimens undergo plastic deformation under impact without any fracture. In practice, micro

or macro cracks emerge during impact, especially for more brittle specimens, which can release the stress and decrease the fluctuation range.

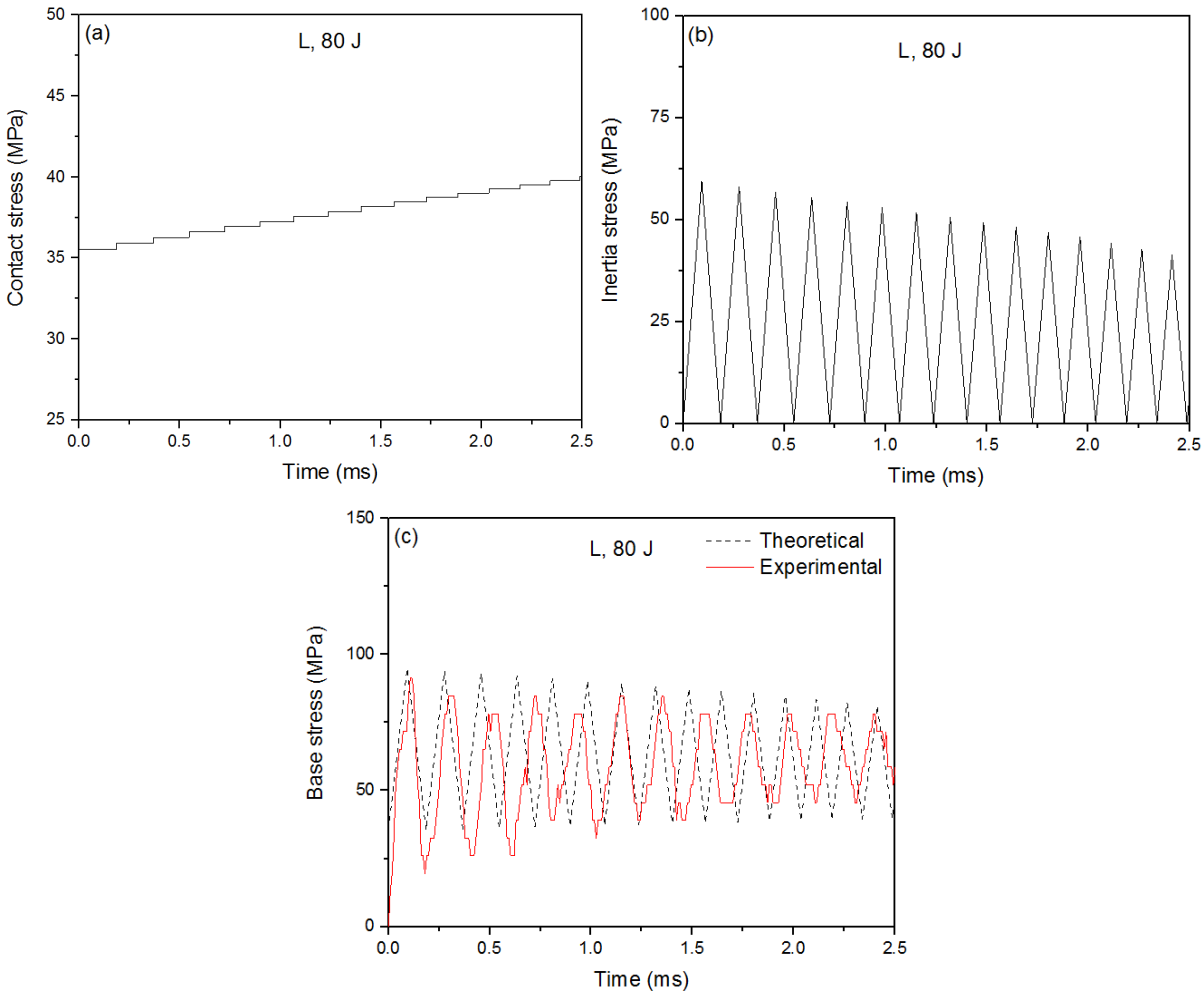

***Figure** 5.4 Theoretical stress evolutions in the uniform AMSF U1 subjected to an impact energy of 80 J: (a) contact stress, (b) inertia stress, and (c) base stress compared to experimental result*

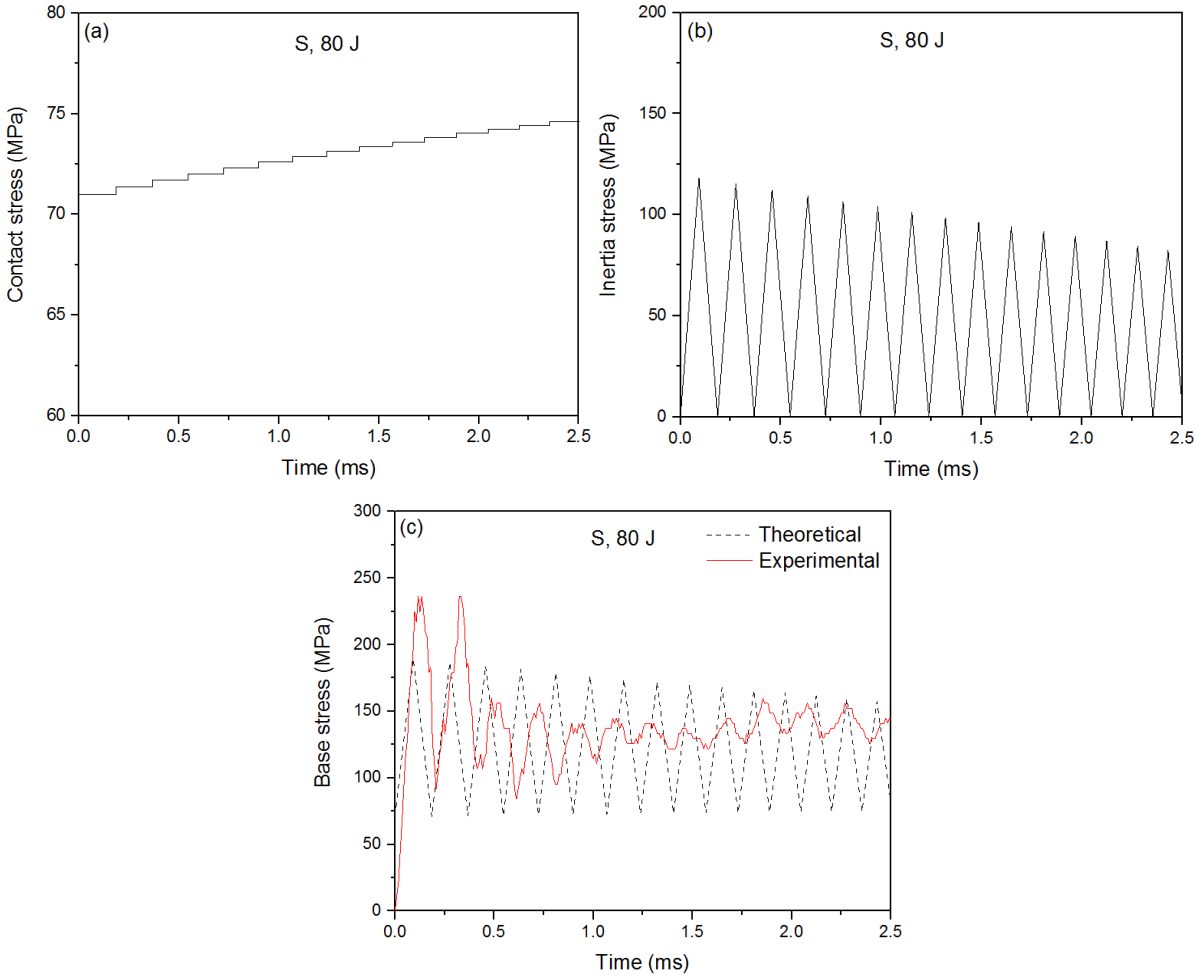

***Figure** 5.5 Theoretical stress evolutions in the homogeneous AMSF specimen S subjected to an impact energy of 80 J: (a) inertia stress, (b) contact stress, and (c) base stress compared to experimental result*

Fig. 5.6 compares the theoretical and experimental results of base stress evolutions in double-CMs layered AMSFs D1 and D2, as an example to illustrate the applications of the model to layered AMSFs. Similar as in the case of uniform AMSFs, the analytical model captures the key characteristics of stress fluctuation with fairly accurate prediction of time period of stress fluctuation and reasonable estimation of stress range of fluctuation.

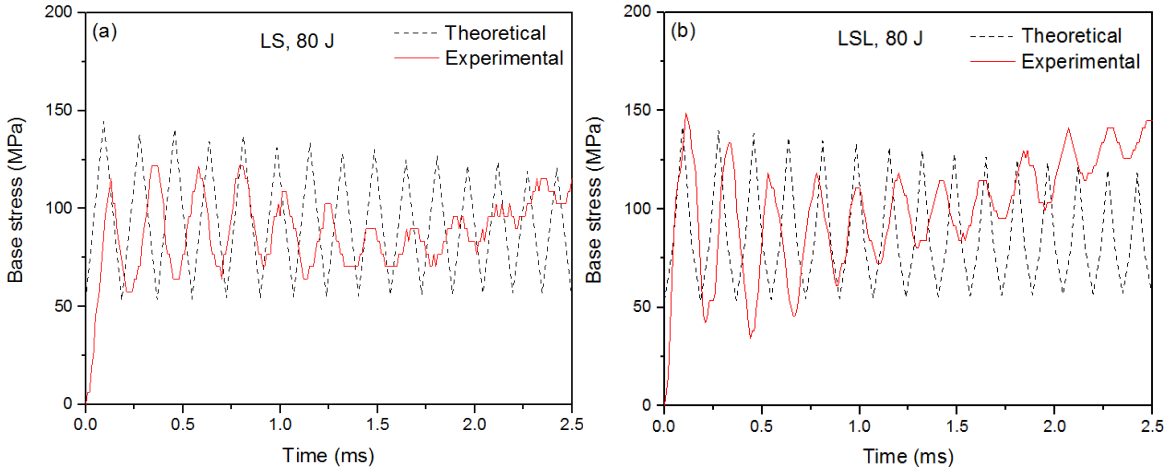

***Figure** 5.6 Theoretical and experimental base stress evolutions in layered AMSFs: (a) D1 and (b) D2*

5.3.2 Strain evolution predictions

The theoretical strain calculated in Eq. (5.5) for the uniform AMSFs U1 and U3, subjected to an impact energy of 80 J, is compared with experimental results in Fig. 5.7. Due to the higher yield stress, S consumed more energy which leads to lower impact strain. The theoretical strain fits well with the experimental strain in both L and S. The difference is in the same order as the experimental errors caused friction or damping of the equipment.

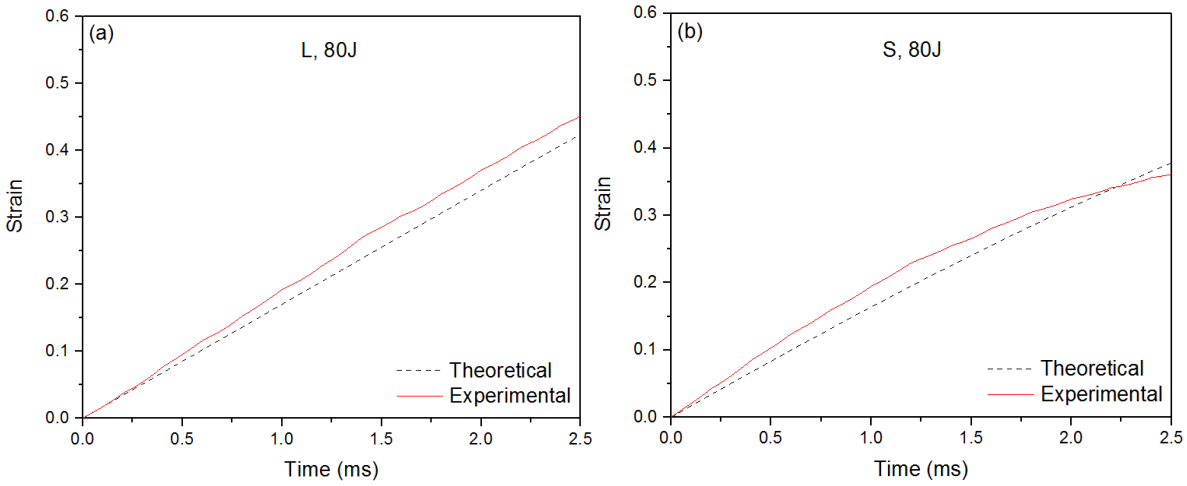

***Figure** 5.7 Theoretical and experimental strain in uniform AMSFs: (a) U1 and (b) U3*

Fig. 5.8 compares the theoretical and experimental results of strain evolutions in double-CMs layered AMSFs D1 and D2. The theoretical strain agrees well with the experimental strain in both D1 and D2.

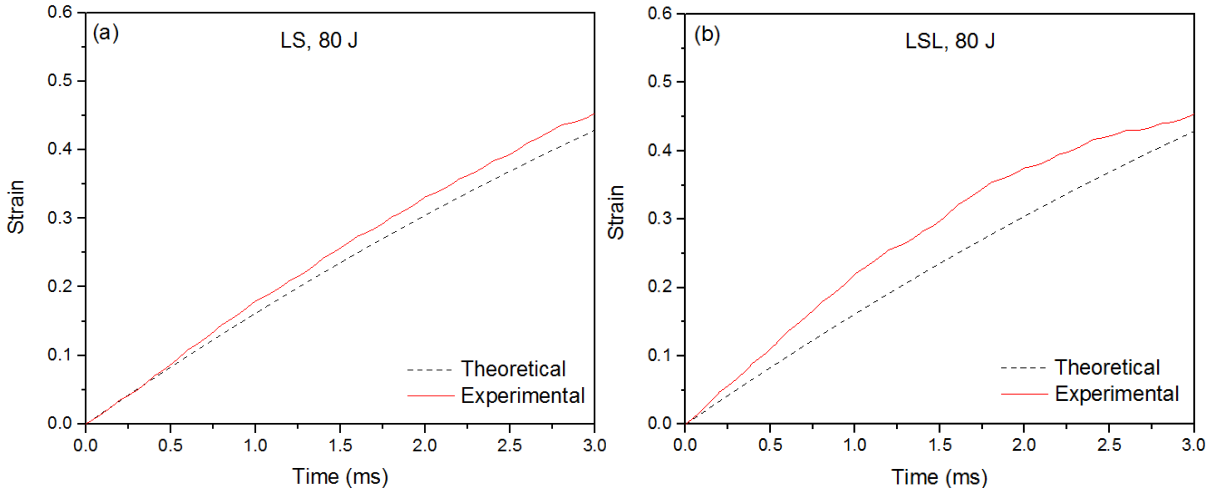

***Figure** 5.8 Theoretical and experimental strain evolutions in layered AMSFs: (a) D1 and (b) D2*

Chapter 6 Discussions

One of the chief aims of using syntactic foams is impact energy absorption. It is essential to conduct experiments to establish the ideal particle size and the ideal structure of particle distribution in the matrix for achieving this purpose. In this chapter, the effects of material parameters and loading conditions on the impact behaviour and properties of AMSFs, based on the experimental results in Chapter 4, will be discussed. The material parameters considered include ceramic microsphere size, uniform, layered and mixed structures. Impact loading conditions, including impact direction, impact velocity, impact energy and impact momentum, are considered. The impact properties considered include peak stress, energy absorption and ductility. These considerations may provide useful information for the design and selection of syntactic foams for different purposes.

6.1 Effect of microsphere size on impact properties

6.1.1 Effect of microsphere size on impact peak stress

Figure 6.1 shows the variation of impact peak stress in uniform syntactic foams under different impact energy levels, obtained from the experimental results in Chapter 4. Generally, peak stress increases with impact energy for all syntactic foams, often nearly linearly. In U1, the samples under 40 J are not densified and have lower peak stresses. The samples under 63 J and over are densified and have higher peak stresses. In U2, all samples are densified. In U3, the samples are not densified until 100 J and the densified samples have higher peak stresses than the un-densified samples.

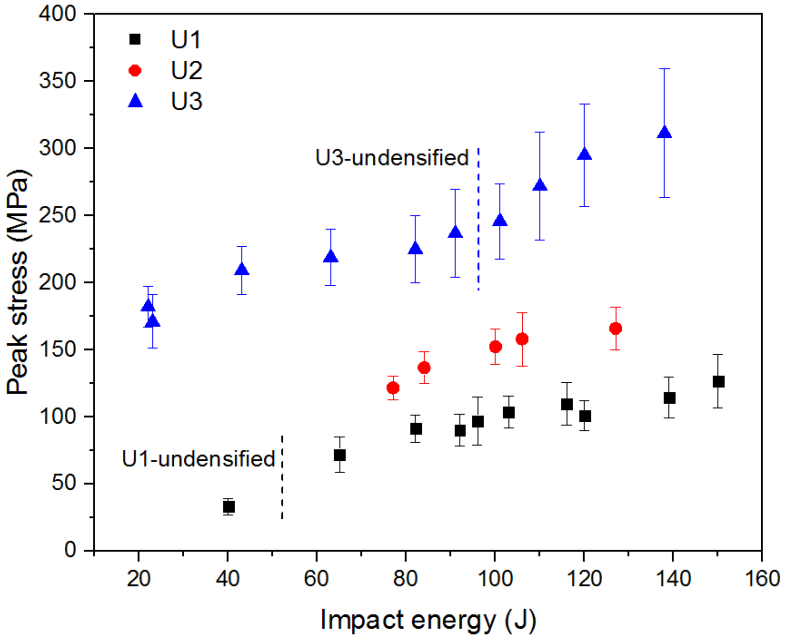

Figure 6.1 *Impact peak stress of uniform syntactic foams under different impact energy levels*

Figure 6.1 shows that peak stress clearly increases with decreasing ceramic microsphere (CM) size. U3 (70-125 μm) has the highest peak stress, U1 (250-500 μm) has the lowest and U2 (125-250 μm) lies in between. The results that small particle size leads to higher strength are consistent with relevant research for both quasi-static loading (Ahmadi et al., 2015) and impact loading (Rousseau et al., 2017). Such effects are easily explained by the fact that smaller microspheres always have greater stiffness than larger ones. Composites with large diameter inclusions have a larger mitigating effect on the imparted stress, while composites made from smaller inclusions have less attenuation, sometimes below the level provided by the matrix (Rousseau et al., 2017). The voids in syntactic foam promote multiple reflections within the specimen, resulting in scattering of the propagation wave. Such scattering also becomes a conduit for further attenuation. However, with absorption being dominated, a decrease in the volume or mass of the matrix may result in a decrease in absorption that is

more significant than the gains attained through scattering. That explains smaller inclusions lead to less attenuation.

Microsphere size also has some effect on crack propagation. Cracks can develop through the matrix, the microspheres or at the interfaces between the microspheres and the matrix. For the same volume fraction, the number of small microspheres is more than that of large microspheres. The interfacial surface, as a type of defect, is larger for small microspheres, which may lead to easier fracture. On the other hand, small microspheres, as a reinforcement, increase the barriers to crack propagation. Therefore, the strength of the bond between the microspheres and the matrix is a crucial factor. If the interfacial bond is strong enough, the strength increases with decreasing microsphere size, as observed in this study.

6.1.2 Effect of microsphere size on impact energy absorption

Figure 6.2 shows the relation between the specific impact energy absorption up to densification and impact energy in uniform syntactic foams, obtained from the experimental results in Chapter 4. It is noted that the specific impact energy absorption here is defined as the energy absorbed at the densification point for the densified samples or at the end of impact for the un-densified samples, the latter of which is basically the initial impact energy. Specific energy absorption generally increases with impact energy, rapidly for un-densified samples and more slowly for densified samples.

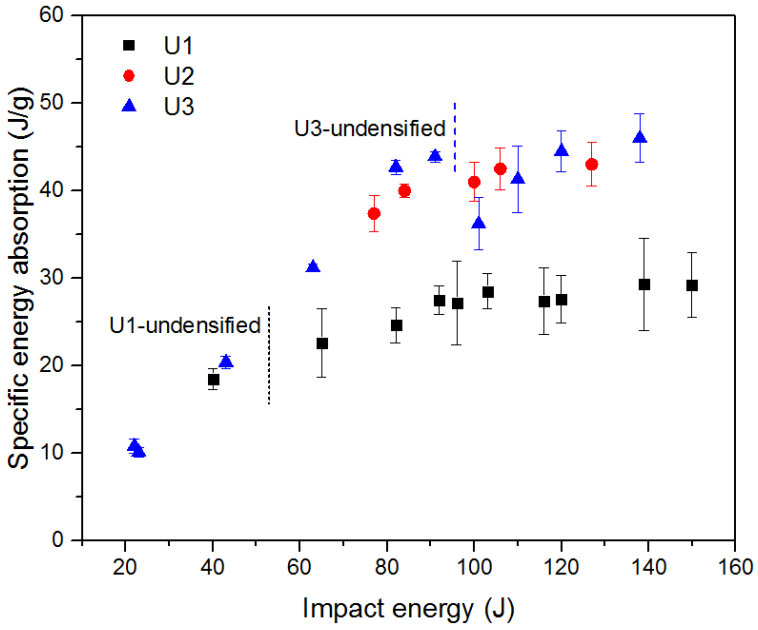

Figure 6.2 *Specific impact energy absorption of uniform syntactic foams up to densification, under different impact energy levels*

Figure 6.2 shows that U1, with the greatest CM size, has the lowest specific energy absorption, while U2 and U3 have a similar specific energy absorption. Specific energy absorption is mainly determined by plateau stress and densification strain. Since the porosity of the syntactic foams in this work is nearly the same, plateau stress is crucial in examining specific energy absorption. Normally, smaller CM size leads not only to higher peak stress, but also to higher plateau stress, assuming specimen is ductile. This explains why U2 has higher specific energy absorption than U1. However, small CMs also bring about brittleness (Tao et al., 2012). The high strength due to small CMs restricts the plastic deformation of the Al matrix, resulting in low strains before fracture. Small CMs also provide more stress concentration sites for the initiation of cracks. When a crack emerges in the plateau region, the stress decreases and so does energy absorption. This explains why U2 and U3 have a similar specific energy absorption.

6.1.3 Effect of microsphere size on impact ductility

Syntactic foams are mainly used for energy absorption purposes. Brittle fracture and cracks lead to stress drop and therefore low energy absorption as well as poor structural integrity. It is therefore important to study the ductility of AMSFs to determine the appropriate load range for each type of syntactic foams.

Figure 6.3 shows the relation between impact ductility of the uniform syntactic foams and impact energy. The nature of failure was observed from the images acquired by high speed camera during impact and classified according to the criteria described in Chapter 4. Ductile means samples are crushed, brittle means samples are cracked. The ductile (D) and brittle (B) samples are marked in the graph, while the unmarked ones are ductile-brittle (DB) samples.

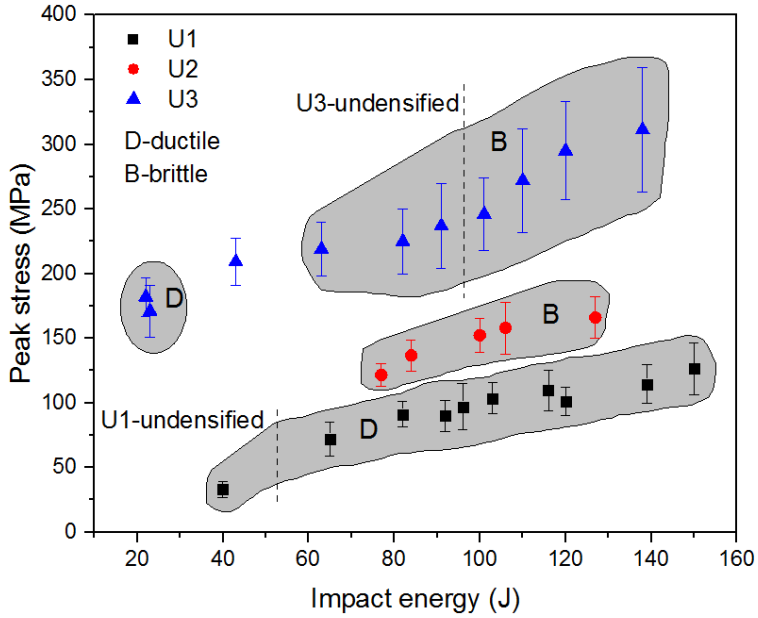

Figure 6.3 *Impact ductility of uniform syntactic foams under different impact energy levels*

As discussed before, higher impact energy leads to higher peak stress, which normally leads to more brittleness. U1 has excellent ductility, showing no cracks under impact energies from

40 J up to 150 J. It indicates that U1 can be used for a wide range of load. U2 is brittle under impact energies from 77 J to 127 J, which means the limit of impact energy for U2 to be ductile is less than 77 J. U3 is ductile at 20 J, ductile-brittle at 40 J, and brittle over 60 J. The limit of impact energy for U3 to be ductile is between 20 J and 40 J. Although U3 has a high specific energy absorption, such a high specific energy absorption cannot be fulfilled under impact loading, because cracks emerge far before densification. Despite the high energy absorption of U2 and U3, the ductility of U1 makes it more impact-tolerating.

The effect of microsphere size on ductility is due to different failure mechanisms with the evolution of stress and energy absorption (Banhart *et al*., 1999; Tao *et al*., 2012). The results in Chapter 4 showed that syntactic foams with large and weak ceramic microspheres (U1) tend to fail in a ductile manner by gradual collapse. The microspheres crumble under the compressive stress. Syntactic foams with small and strong ceramic microspheres (U2 and U3) often fail by brittle fracture with crack formation.

Plastic collapse occurs when the compressive stress exerted on the microspheres exceeds their compressive strength. The load partition between the metal matrix and the ceramic microspheres depends on the relative magnitudes of their elastic modulus, with the stiffer phase bearing a higher stress (Hull & Clyne 1996). A study (Balch & Dunand 2005) on an Al matrix syntactic foam under uniaxial compression showed that the ceramic microspheres bear significantly more stress, by a factor of two, than the matrix.

Brittle fracture of syntactic foams U2 and U3 has the characteristics of Griffith rupture for brittle solids subjected to uniaxial compression. In Griffith rupture, tensile stress concentration at the tips of one or more cracks induces fracture. Griffith rupture has two characteristic features: the fracture cracks propagate at a preferred angle of 30° to the loading direction; the compressive strength is eight times of its tensile strength (Griffith, 1924; Jayatilaka, 1979). Syntactic foams manufactured by infiltration are in effect aggregates of ceramic particles with the interstices filled with a metal network. The numerous contacts between the ceramic particles are effectively cracks, providing a favourable condition for Griffith rupture. Apart from Griffith rupture, cracks with 45° to loading direction are also developed, which is characteristic of shear fracture. The precedence between Griffith rupture and share fracture depends on the shear strength of each syntactic foam.

6.2 Effect of layered structure on impact properties

Many efforts have been made to study the properties of syntactic foams with layered structures (Kishore *et al*., 2005; N. Gupta *et al*., 2006; A. Jamil *et al*., 2017; N. Movahedi *et al*., 2019). However, the effect of layered structure on impact properties is still not well understood. In this section, the impact properties of syntactic foams with layered structures will be compared with those of uniform structures of the constituent layers.

6.2.1 Effect of layered structure on impact peak stress

Figures 6.4 and 6.5 show the relation between peak stress and impact energy in double- and triple-CM layered syntactic foams, respectively. As the double- and triple-CM layered

syntactic foams are made of layers of uniform syntactic foams U1-U3, the average peak stress of the constituent layers at each impact energy is shown for comparison purposes. As the impact energy is not exactly the same among the uniform syntactic foams, linear interpolation has been applied to obtain the average peak stress at some impact energy levels.

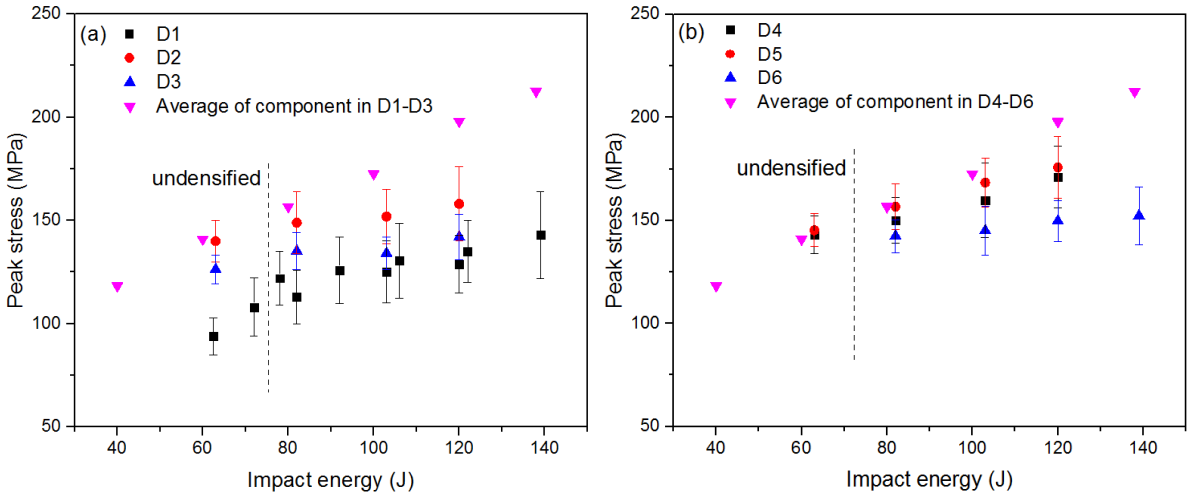

Figure 6.4 *Impact peak stress of double-CM layered syntactic foams under different impact energy levels: (a) D1-D3 and (b) D4-D6*

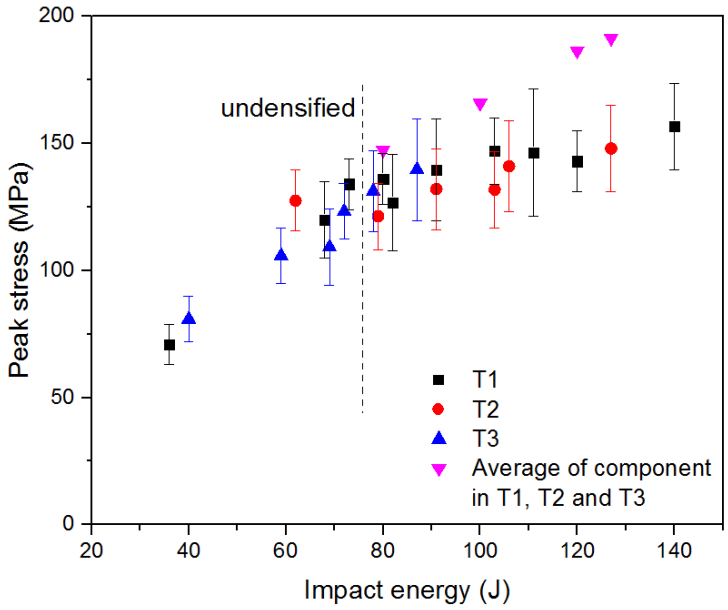

Figure 6.5 *Impact peak stress of triple-CM layered syntactic foams under different impact energy levels*

All six types of double-CM layered syntactic foams have the same components, half each of L and S layers. The only difference among the samples is the number and/or order of layers. All samples generally have lower peak stresses than the averages of their components, as shown in Figure 6.4. All samples are densified at impact energy above about 78 J and peak stress increases slightly with impact energy. The effect of number of layers is significant. D1 (two layers) has a lower peak stress than the other five types of layered syntactic foams. Its peak stress is also significantly lower than the average of the peak stresses of the components. Increasing the number of layers decreases the relative layer thickness, which reduces the barrelling effect and therefore increases the stress in each layer. The barrelling effect is especially significant in weak layer L, which mainly deforms at the beginning of impact. Therefore, the relative layer thickness of weak layer largely determines the peak stress of layered structure. Comparing D2 and D3 and comparing D5 and D6 show that the order of layers has little effect on peak stress.

All three types of triple-CM layered syntactic foams have the same components, one third each of L, M and S layers. The only difference is the order of layers. Figure 6.5 shows that, same as uniform structure, the peak stress of all the triple-CM layered syntactic foams generally increases with impact energy. All samples are densified at impact energy above about 75 J. They have a similar peak stress at each impact energy. The same behaviour among the samples confirms that order of layers has no effect on peak stress of layered syntactic foams. This is because the weaker layer in layered structures always fail before the stronger layers, regardless of relative positions. This has been confirmed by the images of the samples taken during the impact.

Figure 6.5 also shows that all the triple-CM layered syntactic foams have lower peak stresses after densification than the averages of their components. The lower impact stress than uniform syntactic foams with the same components is due the preferential initial deformation in one layer instead of the whole sample. This may provide benefits in impact energy absorption applications, where impact stress is also important. In applications as a protective material, the syntactic foam is considered safer if it has a low peak stress and is not densified after impact. If the impact energy is not totally absorbed by the syntactic foam before densification, the impact stress will increase steadily. In any case, the peak stress is exerted to the bottom of samples. A lower peak stress means that the object being protected by the syntactic foam suffers less impact force.

6.2.2 Effect of layered structure on impact energy absorption

Figures 6.6 and 6.7 show the relation between specific energy absorption and impact energy in double- and triple-CM layered syntactic foams, respectively. The average specific energy absorption of the constituent layers at each impact energy, obtained with linear interpolation wherever necessary, is shown for comparison.

All six types of double-CM layered syntactic foams (D1-D6) have similar specific energy absorptions as the averages of their components, as shown in Figure 6.6. Compared to the uniform syntactic foam U1, the proportion of L layer in D1-D6 is increased from one third to one half. As a consequence, the ductility, as well as the specific energy absorption, is improved. It can be concluded that, with the same components, a layered structure provides the same

energy absorption performance as the uniform structure but a lower peak stress on the object being protected. The structural benefit of the layered syntactic foams is that impact is directed to the soft layers at the beginning and then to the strong layers at the later stage. The former lowers the peak stress and the latter improves the energy absorption capacity.

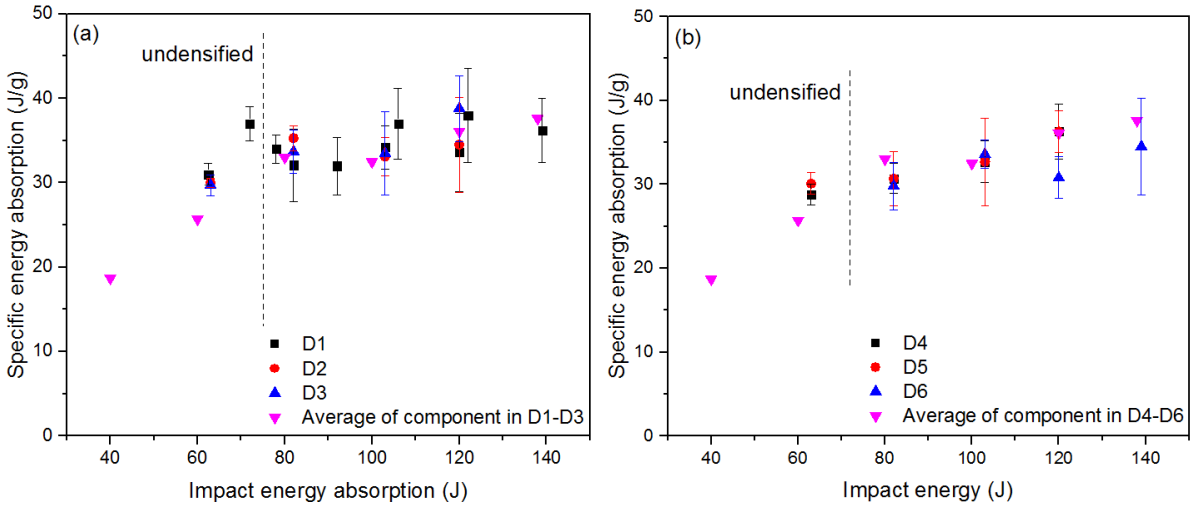

Figure 6.6 *Specific impact energy absorption of double-CM layered syntactic foams up to densification under different impact energy levels: (a) D1-D3 and (b) D4-D6*

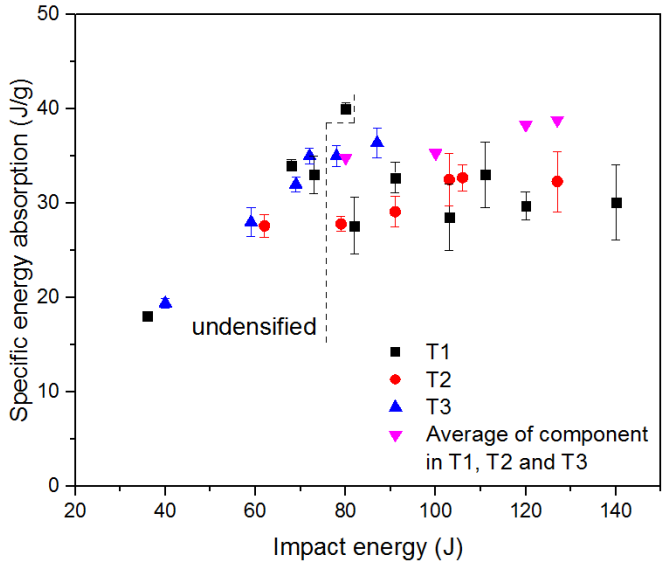

Figure 6.7 *Specific impact energy absorption of triple-CM layered syntactic foams up to densification under different impact energy levels*

The specific energy absorption values of the triple-CM layered structure are lower than the averages of their components. This is due to the brittleness of the M and S layers. The M layer (see U2) is brittle between 78 J and 127 J and the S layer (see U3) is brittle between 60 J and 140 J. Although the L layer (see U1) layer is ductile, it accounts for only one third of the sample and is insufficient to keep all sample ductile.

6.2.3 Effect of layered structure on impact ductility

Figures 6.8 and 6.9 show the relation between impact ductility and impact energy for the double- and triple-CM layered syntactic foams, respectively. It is clear that a low impact energy leads to ductile failure and a higher impact energy gradually leads to brittle failure.

Among the double-CM layered syntactic foams, D1 has excellent ductility where no cracks emerge under 140 J, which is almost twice its densification energy, 75 J. This suggests that D1 has good energy absorption performance under impact loading up to a very high impact energy. D3 is ductile under 100 J and D2, D4-D5 are ductile under 80 J. All samples have higher ductile to brittle transition impact energy than the densification energy, suggesting improved ductility due to increased proportion of L layer. The trend of ductility of the double-CM layered syntactic foams coincides with that of their peak stress shown in Figure 6.5. This confirms that the brittleness is caused by peak stress in impact loading.

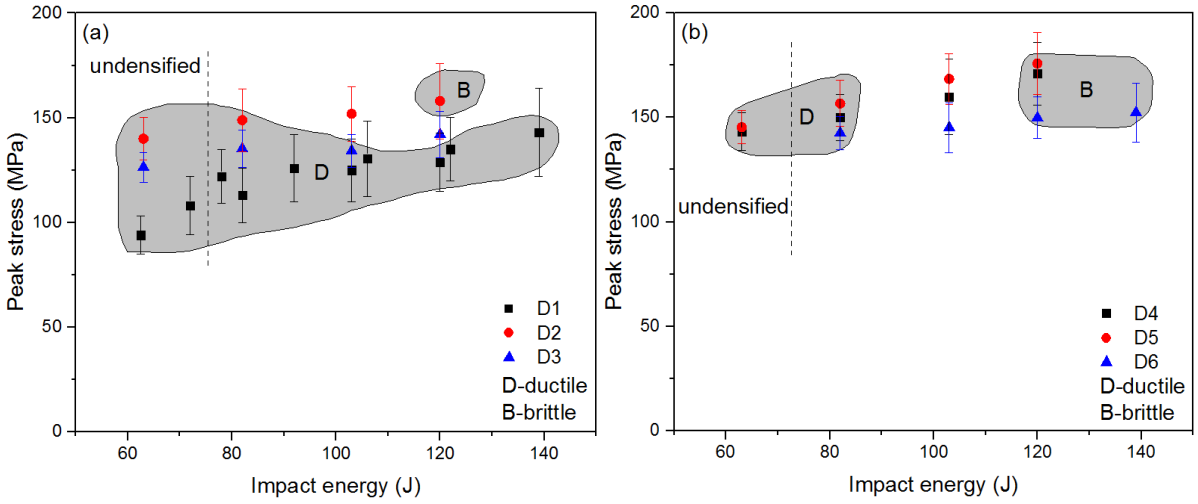

Figure 6.8 *Impact ductility of double-CM layered syntactic foams under different impact energy levels: (a) D1-D3, (b) D4-D6*

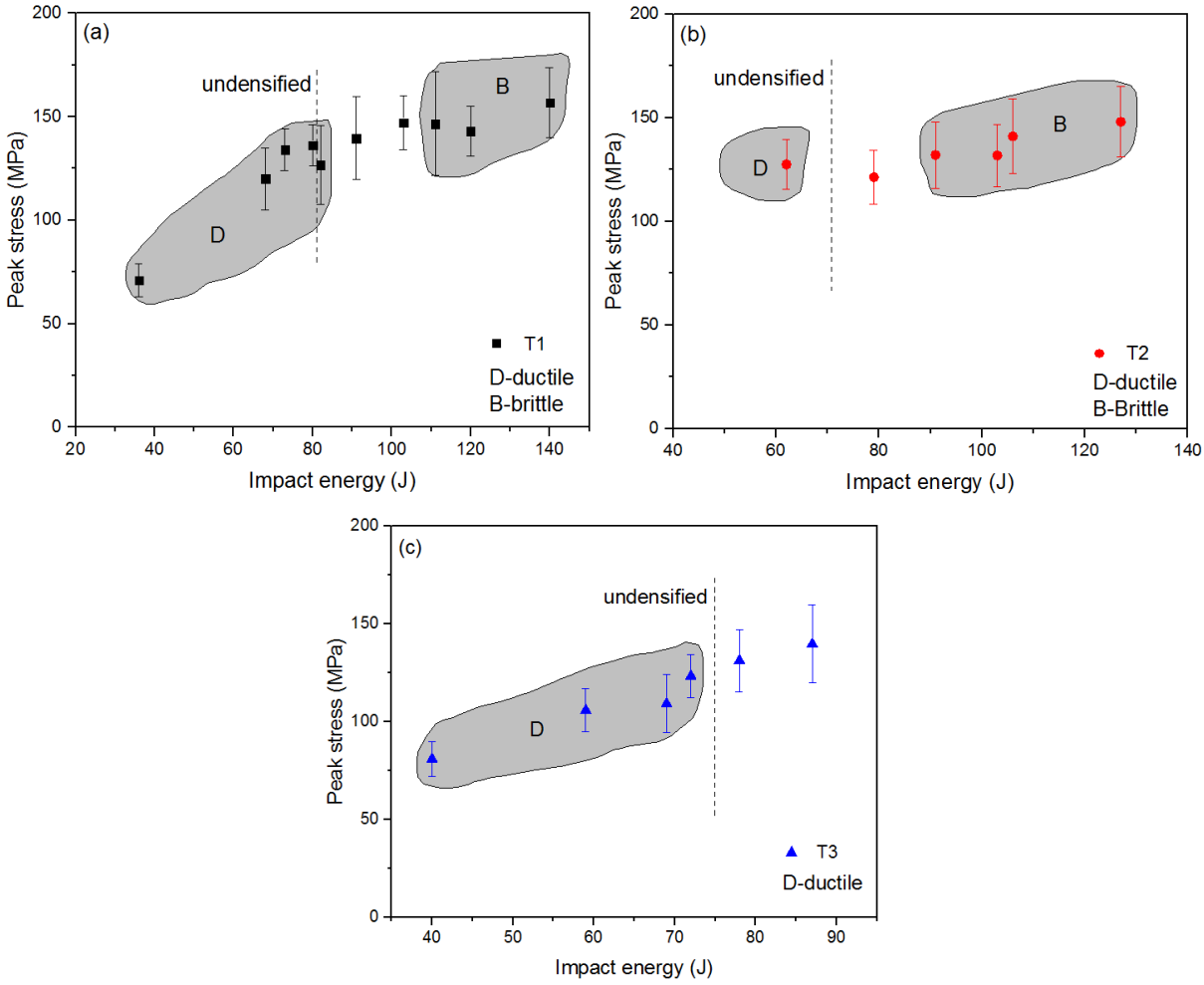

Figure 6.9 *Impact ductility of triple-CM layered syntactic foams under different impact energy levels*

All three types of triple-CM layered syntactic foams (T1-T3) are ductile before densification and the ductile to brittle transition impact energy is the same as the densification energy. As T1-T3 consist of three layers (L, M and S), it means the poor ductility of the S layer is improved and its high specific energy absorption capacity is fulfilled without the emergence of cracks. When the impact energy is higher than the densification energy, cracks emerge in all samples, which suggests that they cannot be safely used above the densification energy.

6.3 Effect of mixed structure on impact properties

6.3.1 Effect of mixed structure on impact peak stress

Figures 6.10 and 6.11 present the relation between peak stress and impact energy in fully mixed and partly mixed syntactic foams, respectively. The weighted average peak stress value of the constituent layers for each sample, calculated by rule of mixture and linear interpolation, is also listed for reference. Figure 6.10 shows that peak stress increases with impact energy. M1 is densified at an impact energy of about 90 J, while M2 and M3 are densified at about 70 J. The peak stress in M3 is lower than in M1 and M2, because it has weaker L spheres than M1 and M2.

It is shown that fully and partly mixed structures have higher peak stresses than the averages of their constituent layers. The higher peak stress can lead to poor impact ductility. Although a higher peak stress leads to an increased specific energy absorption, the energy absorption capacity cannot be fulfilled with such a poor ductility.

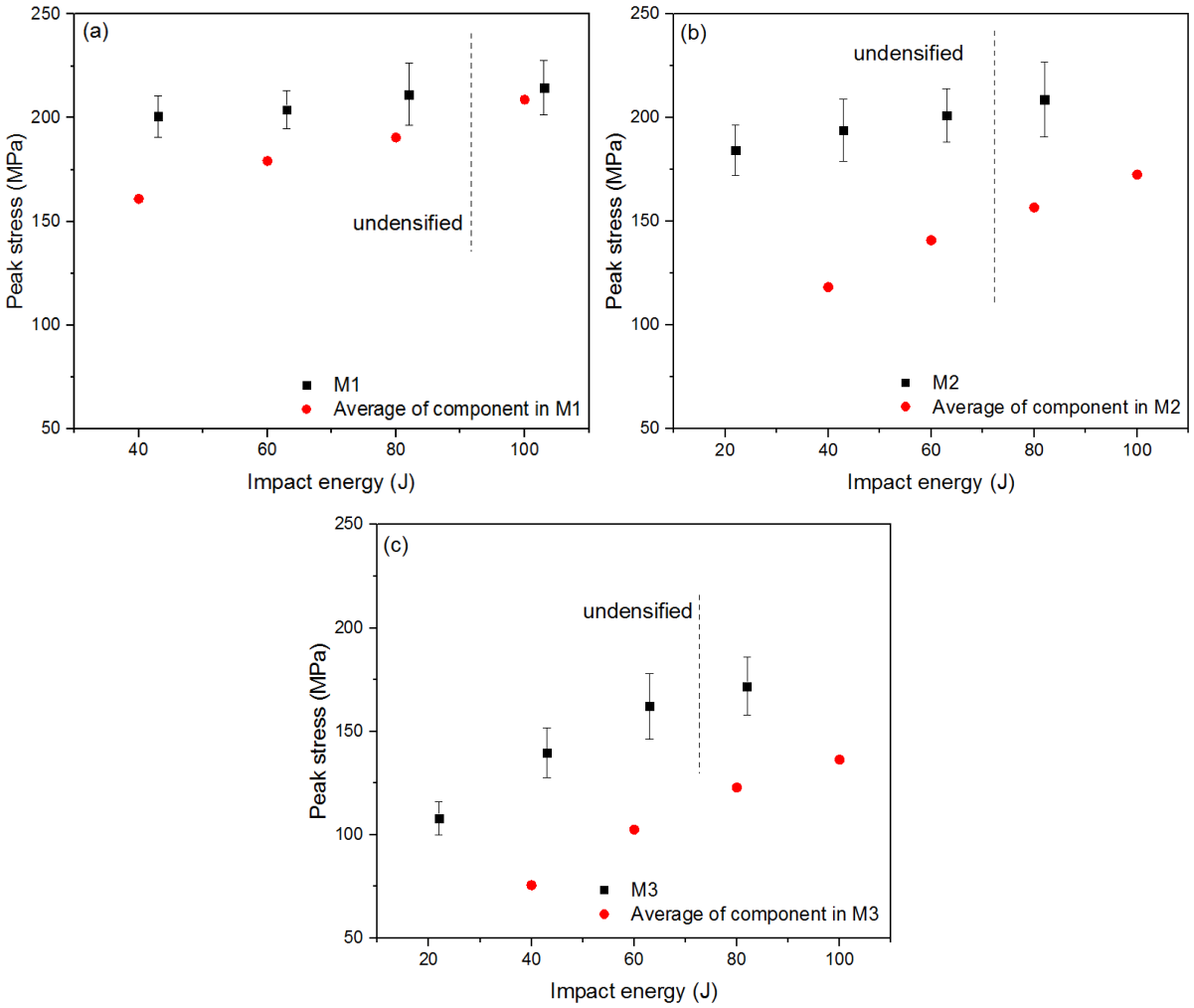

Figure 6.10 *Impact peak stress of fully mixed syntactic foams under different impact energy levels: (a) M1, (b) M2, (c) M3*

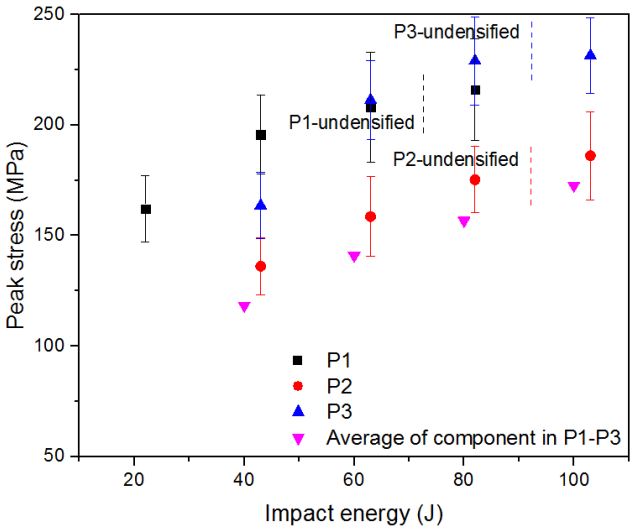

Figure 6.11 *Impact peak stress of partly mixed syntactic foams under different impact energy levels*

6.3.2 Effect of mixed structure on impact energy absorption

Figures 6.12 and 6.13 show the relation between specific energy absorption and impact energy in fully mixed and partly mixed syntactic foams, respectively. The weighted average energy absorption values calculated from their constituent layers are also shown for reference. All densified mixed syntactic foams have higher specific energy absorption values than the averages of their components, due to increased peak stresses. However, as discussed before, high energy absorption capacity is not sufficient for impact loading applications. Adequate ductility is required to keep the sample intact during impact.

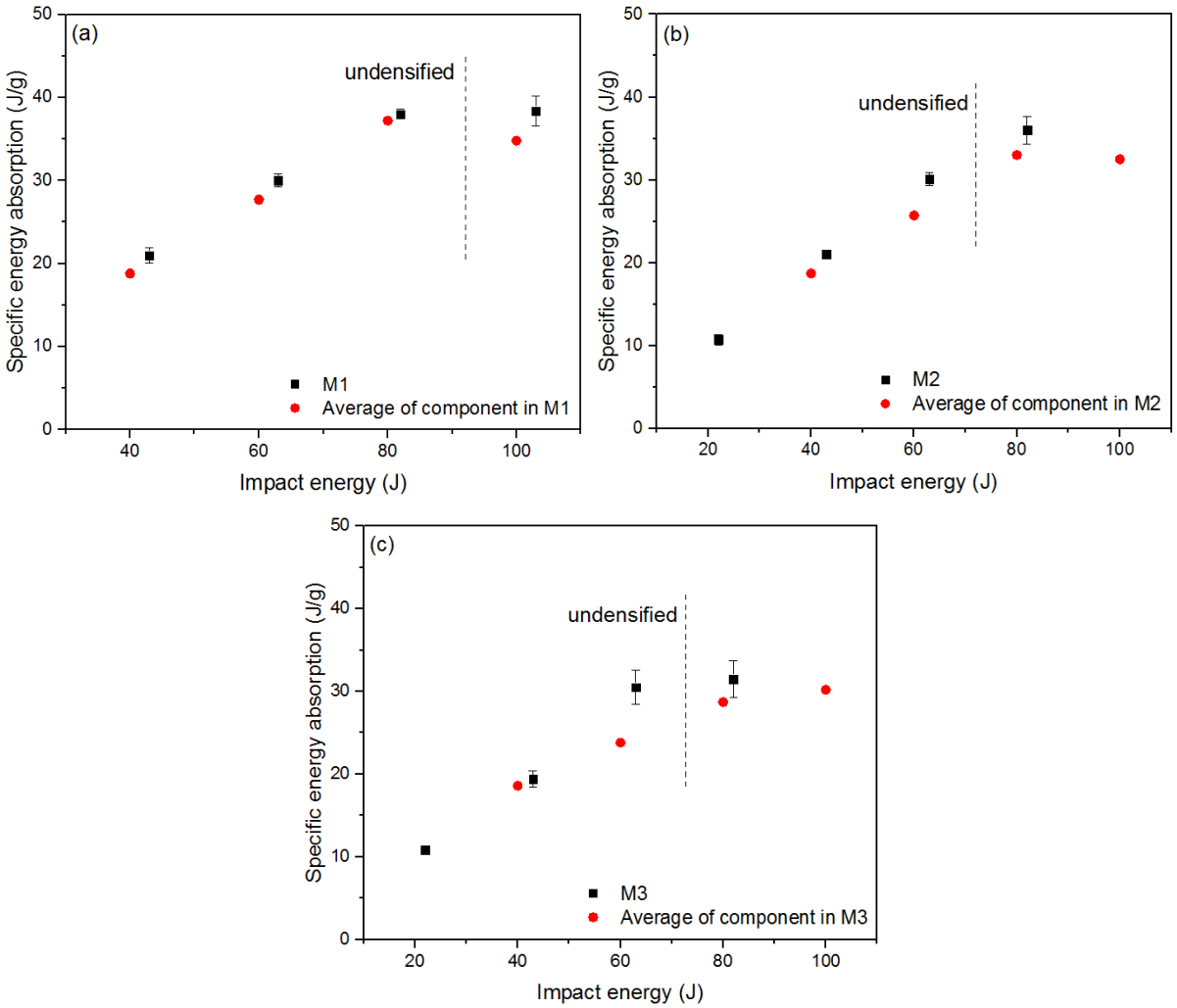

Figure 6.12 *Specific impact energy absorption of fully mixed syntactic foams under different impact energy levels: (a) M1, (b) M2, (c) M3*

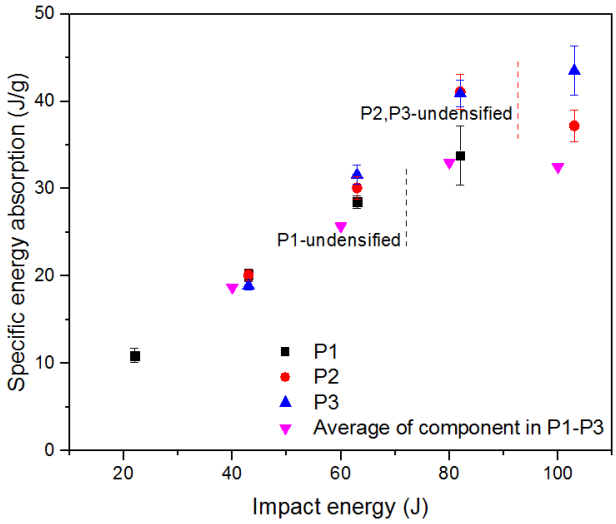

Figure 6.13 *Specific impact energy absorption of partly mixed syntactic foams under different impact energy levels*

6.3.3 Effect of mixed structure on impact ductility

Figures 6.14 and 6.15 illustrate the impact ductility of fully and partly mixed syntactic foams under different impact energy levels, respectively. M1, M2, M3, P1, P2 and P3 are ductile under an impact energy at or below 40, 20, 20, 20, 40 and 40 J, respectively. They have cracks emerging before densification, which occurs at impact energies about 70 - 90 J. Such poor ductility restricts the energy absorption process.

In summary, mixed structures, both fully mixed and partly mixed, lead to higher peak stress and higher energy absorption but lower ductility. The syntactic foams start to crack before densification. Therefore, mixed structures, at least the ones studied in this work, are not ideal for impact loading applications due to the poor ductility.

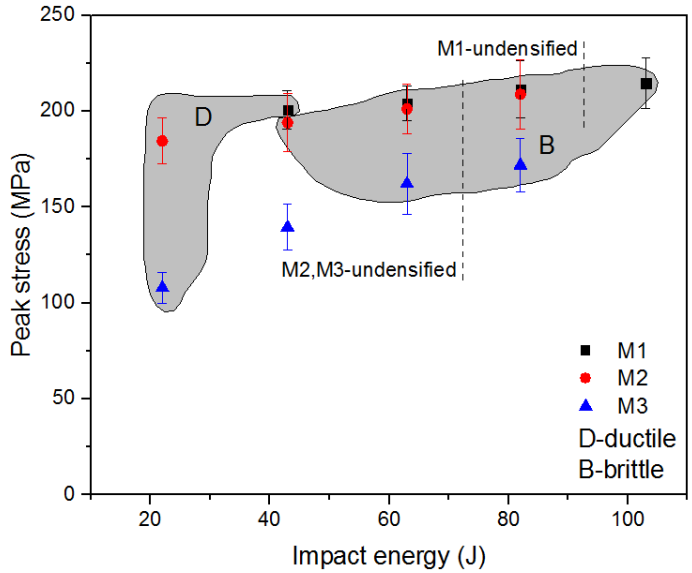

Figure 6.14 *Impact ductility of fully mixed syntactic foams under different impact energy levels*

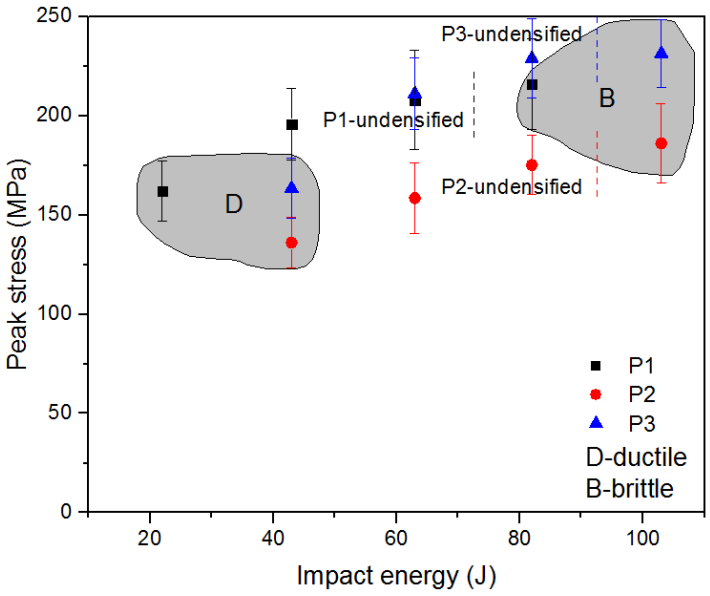

Figure 6.15 *Impact ductility of partly mixed syntactic foams under different impact energy levels*

6.4 Effect of impact loading direction on impact properties

6.4.1 Effect of loading side on impact peak stress

Figure 6.16 shows peak stress of T1-up and T1-down under different impact energy levels. It shows that the triple-CM layered syntactic foam T1 has the same peak stress when impacted from both directions. The theoretical analysis in Chapter 5 has shown that there is no real difference between the top side and bottom side of the sample during the entire impact process, although stress distribution across the sample varies with the propagation of plastic waves. The experimental results have also shown that weak layers always fail before strong layers regardless of their relative locations. This suggests that layered syntactic foams, as an impact protecting material, can have the strong layer either outside or inside and will make little difference from peak stress point of view.

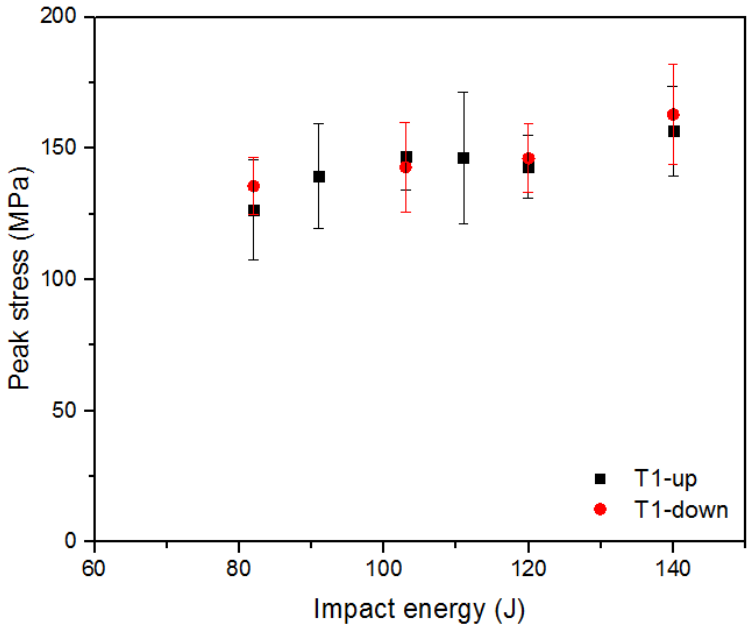

Figure 6.16 *Effect of impact direction on peak stress in triple-CM layered AMSFs under different impact energy levels*

6.4.2 Effect of loading side on impact energy absorption

Figure 6.17 shows the specific energy absorption of T1-up and T1-down under different impact energy levels. Similar to the trend in peak stress, impact direction has little effect on specific energy absorption up to densification. This is because stress evolution in T1-up and

T1-down has the same pattern. The layered syntactic foams will have a similar deformation behaviour when impacted from either direction and therefore have the same specific energy absorption capacity.

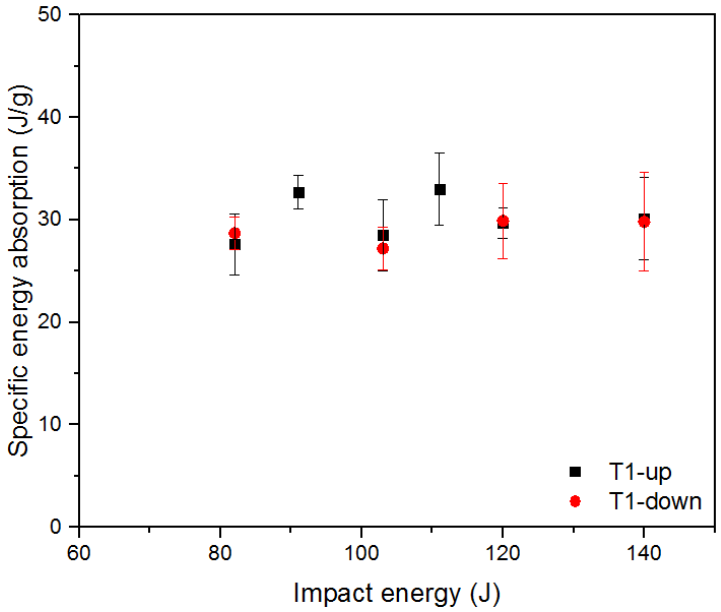

Figure 6.17 *Effect of impact direction on specific energy absorption in triple-CM layered AMSFs under different impact energy levels*

6.4.3 Effect of loading side on impact ductility

Figure 6.18 shows the impact ductility of T1-up and T1-down under different impact energy levels. It shows that the triple-CM layered syntactic foam T1 has the same ductility when impacted from both directions. It is ductile under an impact energy up to 80 J, regardless of the impact direction. It confirms that impact on different sides of the layered structure has no effect on impact ductility due to the same failure behaviour. In summary, the effect of impact direction on layered syntactic foams on peak stress, specific energy absorption and ductility is negligible, if the impact load is applied perpendicular to the layers.

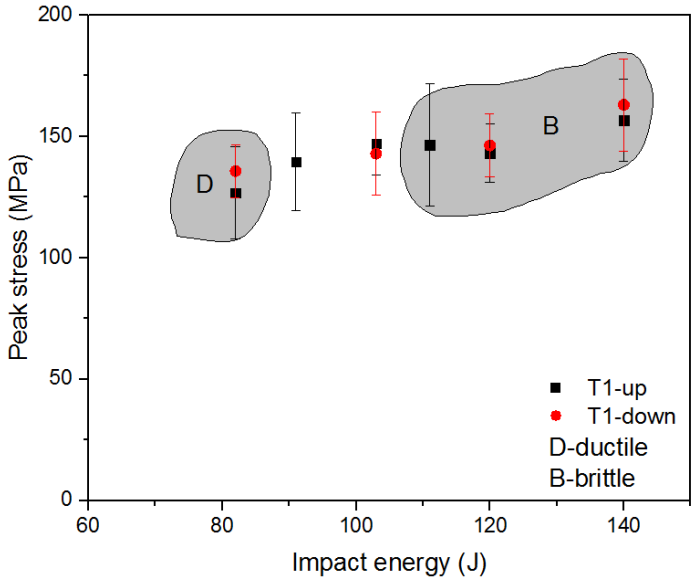

Figure 6.18 *Effect of impact direction on impact ductility in triple-CM layered AMSFs under different impact energy levels*

6.5 Effect of impact strain rate on impact properties

Effect of dynamic or impact loading on syntactic foams is widely studied (Altenaiji *et al*., 2014; Goel *et al*., 2014;Myers *et al*., 2015; Zhang *et al*., 2016; Pham *et al*., 2018). It is conclusive that dynamic or impact loading leads to brittleness. Higher strain rate leads to higher peak stress, higher plateau stress and higher energy absorption.

The failure modes in syntactic foams under quasi-static and dynamic or impact conditions are different. In quasi-static loading, a slow and diffusive compression of the specimen is observed. The hollow spheres are broken and flattened and the matrix material is deformed plastically, with the specimen remaining a whole piece. In dynamic loading, the nature of failure changes due to the restricting effect of the material during sudden loading. Hollow spheres rupture, cracks emerge and the specimen is broken into large pieces.

Impact loading test is generally applied with either split-Hopkinson press bar (SHPB) for high strain rate (HSR) (Omar *et al*., 2015; Licitra *et al*., 2015) or drop weight test for low strain rate (Li *et al*, 2007; Woldesenbet, 2008). In SHPB, strain rate is constant and the effect of impact loading is normally described as a function of discrete strain rate. In drop weight test, however, the impact energy is gradually absorbed by specimen and the strain rate is decreasing. Therefore, the effect of impact loading is normally described as a function of the initial strain rate. In this work, the initial strain rate, which is acquired by dividing the initial impact velocity with the height of specimen, is used. In this section, the impactor mass was kept constant, 12 kg for syntactic foams U2, T2 and T3, and 15 kg for the other types of syntactic foams.

6.5.1 Effect of strain rate on impact peak stress

Figure 6.19 presents the relation between peak stress and initial strain rate in the uniform, layered and mixed syntactic foams. Peak stress increases with initial strain rate for all types of syntactic foams, which agrees with the results of similar studies (Goel *et al*., 2012; Zou *et al*., 2013; Luong *et al*., 2013).

6.5.2 Effect of strain rate on impact energy absorption

Figure 6.20 shows the effect of initial strain rate on specific energy absorption in the uniform, layered and mixed syntactic foams. At lower initial strain rates, where the impact energy is insufficient to densify the specimen (like in U3, M1-M3 and P1-P3), specific energy absorption increases rapidly with initial strain rate. After densification, specific energy absorption either increases slightly with strain rate (U1, U2, T2, T3 and D3-D5) or remains constant (T1, D1, D2

and D6). The effect of impact loading parameters is secondary, because specific energy absorption describes the capacity of the syntactic foam and is primarily determined by the material.

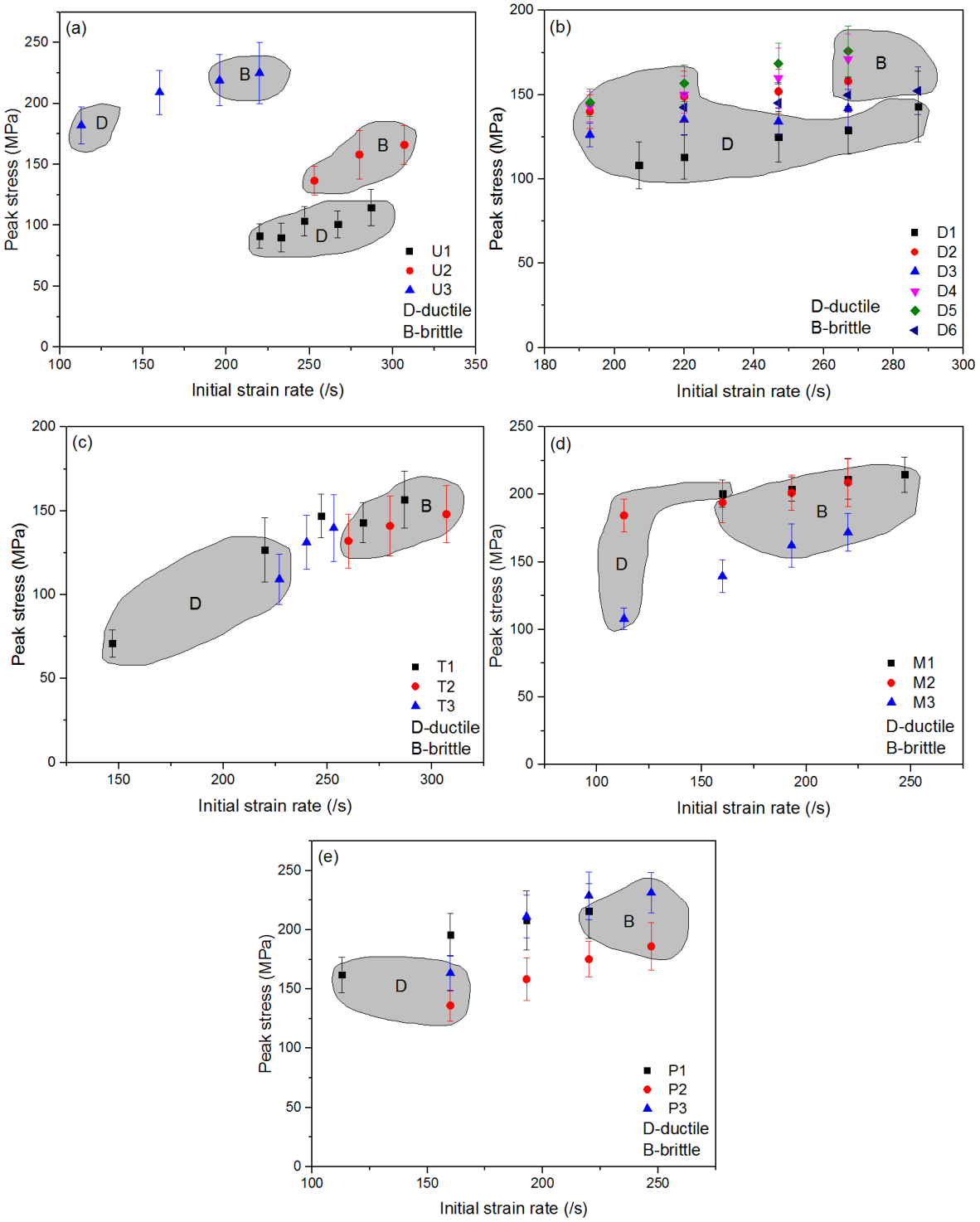

Figure 6.19 *Effect of strain rate on peak stress and ductility in AMSFs: (a) uniform, (b) double-CM layered, (c) triple-CM layered, (d) fully mixed and (e) partly mixed*

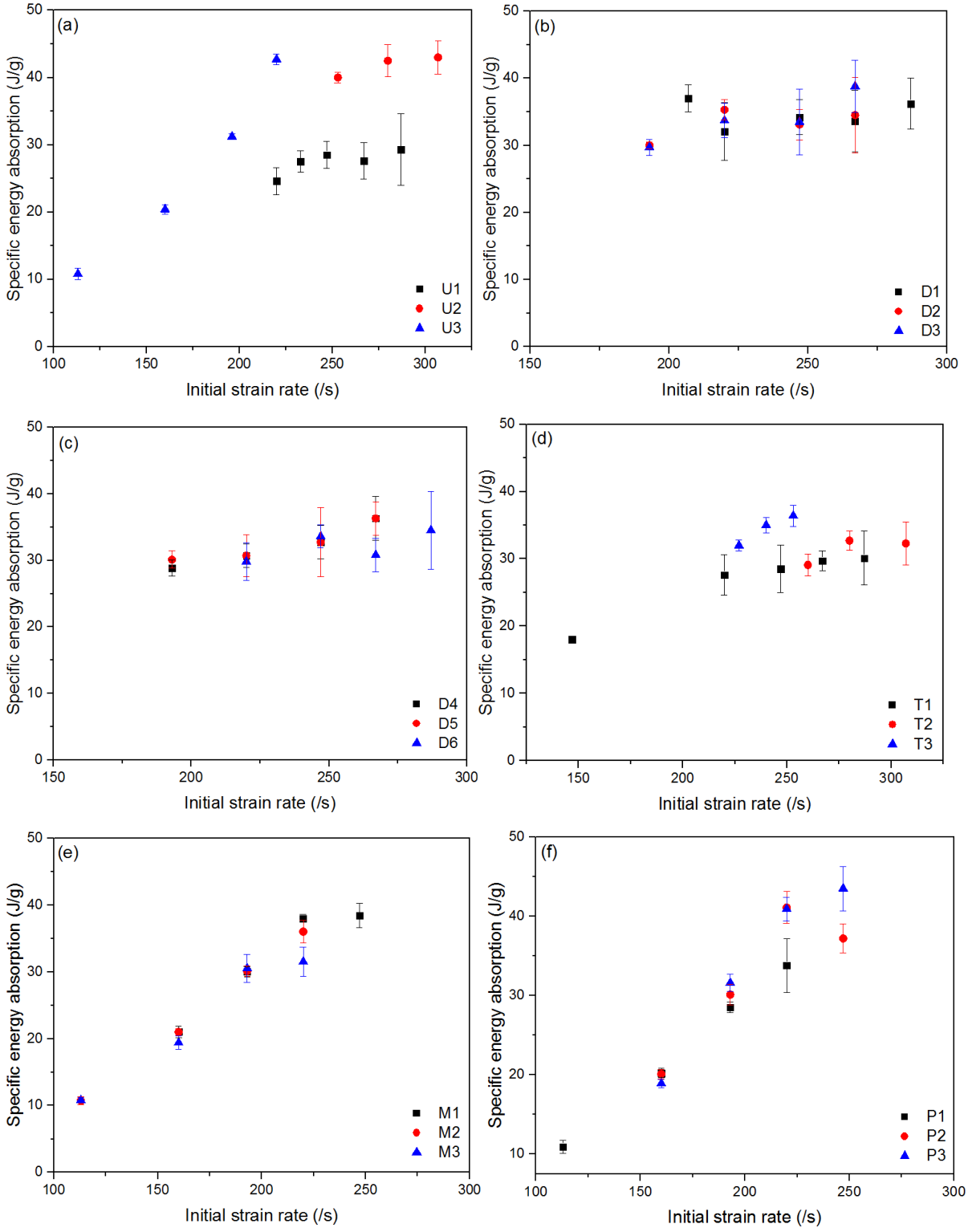

Figure 6.20 *Effect of strain rate on specific energy absorption in AMSFs: (a) uniform, (b) double-CM layered D1-D3, (c) double-CM layered D4-D6, (d) triple-CM layered, (e) fully mixed and (f) partly mixed*

6.5.3 Effect of strain rate on impact ductility

The effect of initial strain rate on impact ductility is also shown in Figure 6.19. As shown, some syntactic foams, like U1, D1 and D3, have better ductility; some, like U2, U3, M1-M3 and P1-P3, have poor ductility; and some, like T1, T3, D2 and D4-D6, have medium ductility.

As discussed previously, small CM size leads to high specific energy absorption but poor ductility due to the high peak stress. However, high specific energy absorption is pointless without sufficient ductility, because the syntactic foam will crack apart before the energy absorption capacity is fulfilled. Therefore, it is necessary for the syntactic foam to remain ductile or at least have a medium ductility before densification under an impact energy. It would be even better if the syntactic foam remains ductile under an impact higher than the densification energy. In this study, D1 (L-S) and D3 (S-L-S) are found to be optimised layered structures with both high energy absorption capacity, derived from small CMs, and high ductility, derived from large CMs.

6.6 Effect of impact momentum on impact properties

Up to date, few studies have discussed the effect of impact momentum on impact properties of syntactic foams. In most studies, impact mass or impact velocity is changed separately to study their effects. Different combinations of impact mass and impact velocity can result in the same impact energy but different momenta, or vice versa. In this work, we fix impact energy and change the initial impact momentum, through changing the combination of impact mass and impact velocity, so that we can study the effect of impact momentum alone.

Samples under similar impact energies are grouped together as the impact energies are normally not identical.

6.6.1 Effect of impact momentum on impact peak stress

Figure 6.21 shows the effect of impact momentum on peak stress in selected syntactic foam samples under similar impact energies. In both uniform and layered syntactic foams, peak stress generally decreases with increasing impact momentum. For the same impact energy, a higher impact momentum means a higher impact mass and a lower impact velocity. The latter leads to lower strain rate and lower peak stress. This suggests that impact velocity is more important to the impact behaviour than impact mass.

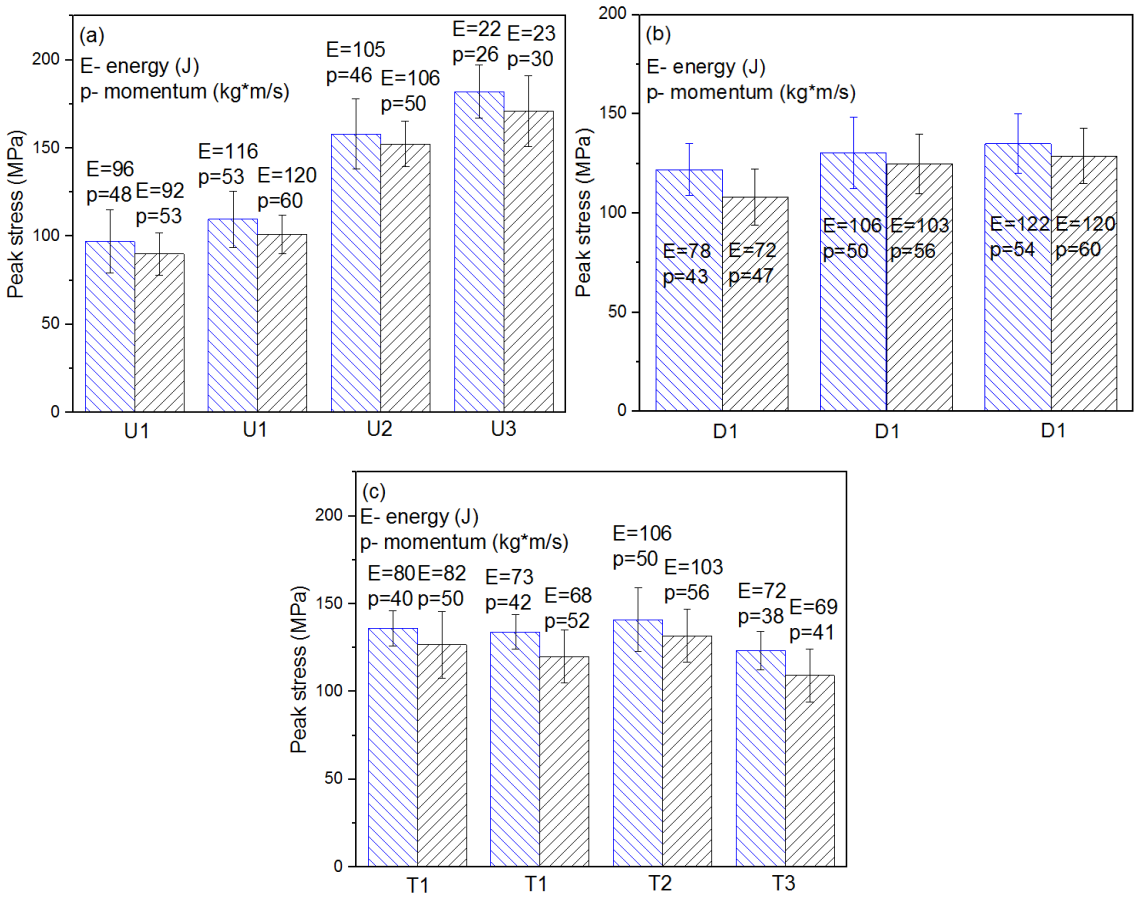

Figure 6.21 *Effect of impact momentum on peak stress in AMSFs: (a) uniform, (b) double-CM layered, (c) triple-CM layered*

6.6.2 Effect of impact momentum on impact energy absorption

Figure 6.22 shows the relation between specific energy absorption and impact momentum. Under a similar impact energy, changing impact momentum can lead to either an increase or a decrease in specific energy absorption. The effect of impact momentum on specific energy absorption is inconclusive. Although both impact momentum and impact energy are dependent variables derived from impact mass and impact velocity, it seems that impact energy is more important to the energy absorption process while impact momentum only affects peak stress.

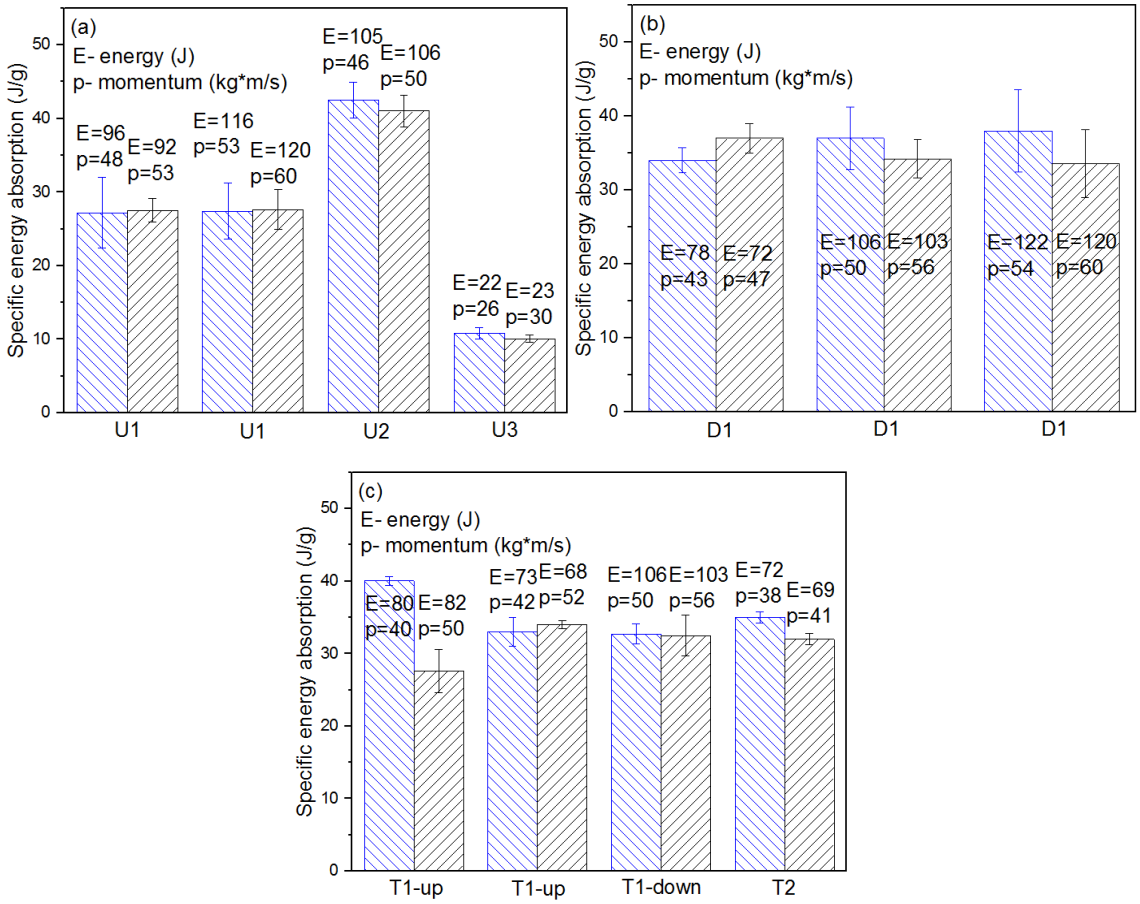

Figure 6.22 *Effect of impact momentum on specific energy absorption in AMSFs: (a) uniform, (b) double-CM layered, (c) triple-CM layered*

Chapter 7 Conclusions and Future Work

7.1 Conclusions

7.1.1 Microstructure

AMSFs with uniform, layered and mixed structures were fabricated by the pressure infiltration process. The uniform, layered and mixed AMSFs had porosity ranges of 42% - 49%, 40.5% - 48.2% and 40% - 46.7%, respectively. Uniform AMSFs have a homogeneous microstructure containing large (250-500 μm, L), medium (125-250 μm, M) or small (70-125 μm, S) CMs. Double-CM layered AMSFs contain half each of L and S, and have six layer structures: L-S, L-S-L, S-L-S, L-S-L-S, L-S-L-S-L and S-L-S-L-S. Triple-CM layered AMSFs contain one third each of L, M and S, and have three layer structures: L-M-S, M-L-S and L-S-M. All layered AMSFs exhibited homogeneous microstructures with uniformly distributed CMs in the Al matrix. Fully mixed AMSFs contain mixed structure of L and S, with 25%, 50% or 75% of L. Partly mixed AMSFs contain several layers of L-S mixtures: L-25%L/75%S-S-25%L/75%S-L, L-50%L/50%S-S-50%L/50%S-L or 75%L/25%S-S-75%L/25%S. The mixed AMSFs also exhibited homogeneous microstructures with uniformly distributed CMs in the Al matrix.

7.1.2 Compressive behaviour

Uniform AMSFs with small CMs had higher compressive strengths than those with larger CMs. Each layered AMSF had a single yield strength, although each layer has a different yield strength, because the layers are well bonded and forced to deform in coordination. Increasing number of layers and reducing layer thickness in layered AMSFs led to higher compressive strength, while changing order of layers had no effect on compressive strength. Mixed AMSFs

behaved like uniform AMSFs, the compressive strength was higher than the average of its component.

Energy absorption up to densification in AMSFs was mainly determined by the plateau stress. Uniform AMSFs with smaller CMs and layered AMSFs with more layers had higher compressive strength and therefore higher energy absorption, provided they are ductile. Mixed AMSFs had higher energy absorption than the average of its component.

7.1.3 Impact behaviour

Uniform AMSFs with smaller CMs and layered AMSFs with more layers had higher peak stresses. Mixed AMSFs had a higher peak stress than the average of peak stresses of its constituent layers, while layered AMSFs had a lower peak stress than the average of peak stresses of its constituent layers. A higher strain rate led to a higher peak stress in all uniform, layered and mixed AMSFs. Impact on different side of the layered structure showed similar properties. Under the same impact energy, the effect of impact momentum on peak stress was not significant. Energy absorption up to densification had the same trend as peak stress.

Uniform AMSFs with smaller CMs were more brittle. Layered structures had better ductility than uniform and mixed structures. Soft layers yield before strong layers regardless the relative layer locations. Layered structures with more layers were more brittle. Mixed AMSFs were more brittle than uniform ASMFs. Impact on different side of the layered structure had no effect on impact ductility.

Layered structures combining high strength layers and high ductility layers can have a reduced peak stress and an improved ductility under impact, without compromising the energy absorption capacity. Layered structures are a promising solution for optimum energy absorption performance combining high energy absorption capacity and good ductility.

7.1.4 Analytical model

An analytical model has been developed to simulate the stress and strain evolutions in ASMFs. Impact loading generates an elastic wave and a plastic wave at the top of specimen. The elastic wave turns into a plastic wave when it bounces back at the bottom the specimen. The two plastic waves then propagate inside the specimen with the same speed but opposite directions. In each cycle when the two plastic waves propagate from one end to the other, the specimen can be divided into four zones: one wave has passed (X2), neither wave has passed, and both waves have passed. The stress and strain in each zone are calculated separately and summed up to give the total inertia stress and strain in the specimen. The base stress is the sum of the inertia stress and the contact stress, which is calculated from the loss of impactor momentum. The evolutions of base stress and strain during impact predicted by the analytical model agreed well with the experimental results.

7.2 Future work

Layered AMSFs were found to have better ductility than uniform AMSFs under impact loading, without compromising energy absorption capacity. However, the improvement on ductility

has not been optimized in this work. To increase the ductility further, more studies on the effects of layered structures, including CM size, proportion, distribution and layer thickness, are needed.

Theoretically, impact peak stress is directly related to the impact force, which is expected to be proportional to the momentum of the projectile or hammer at the point of impact. However, the effect of impact momentum on peak stress is inconclusive in this work. Further studies are necessary to understand the effect of impact momentum on the behaviour of AMSFs, to complement the understanding of the effect of impact energy.

The bonding between layers in layered AMSFs was found to have a significant effect on the behaviour of the ASMFs, e.g., the ductility under impact loading. Further tests, like shear test, can be carried out to study the effect of layer bonding on static and impact behaviour of layered AMSFs, in order to maximise their energy absorption performance.

References

Ahmad, Z., Thambiratnam, D.P., Tan, A.C.C. (2010), Dynamic energy absorption characteristics of foam-filled conical tubes under oblique impact loading, *International Journal of Impact Engineering* 37, 475-488.

Ahmadi, H., Liaghat, G.H., Shokrieh, M.M., Hadavinia, H., Ordys, A. and Aboutorabi, A. (2015), Quasi-static and dynamic compressive properties of ceramic microballoon filled syntactic foam, *Journal of Composite Materials* 49 (10), 1255-1266.

Ali, M., Qamhiyah, A., Flugrad, D., Shakoor, M. (2008), Theoretical and finite element study of a compact energy absorber. *Advances in Engineering Software* 39, 95-106.

Al-Sahlani, K., Taherishargh, M., Kisi, E., Fiedler, T. (2017), Controlled shrinkage of expanded glass particles in metal syntactic foams, *Materials* 10 (9), 1073.

Altenaiji, M., Guan, Z.W., Cantwell, W.J., Zhao, Y. and Schleyer, G.K. (2014), Characterisation of aluminium matrix syntactic foams under drop weight impact, *Materials & Design* 59, 296-302.

Alizadeh, M., Mirzaei-Aliabadi, M. (2012), Compressive properties and energy absorption behavior of AleAl2O3 composite foam synthesized by space-holder technique, *Materials & Design* 35, 419-424.

Anantharaman, H., Shunmugasamy, V.C., Strbik iii, O.M., Gupta, N., Cho, K. (2015), Dynamic properties of silicon carbide hollow particle filled magnesium alloy (AZ91D) matrix syntactic foams, *International Journal of Impact Engineering* 82, 14-24.

Anbuchezhiyan, G., Mohan, B., Sathianarayanan, D., Muthuramalingam, T., (2017), Synthesis and characterization of hollow glass microspheres reinforced magnesium alloy matrix syntactic foam, *Journal of alloys and compounds* 719, 125-132.

Avalle, M., Chiandussi, G. (2007), Optimisation of a vehicle energy absorbing steel component with experimental validation, *International Journal of Impact Engineering* 34, 843-858.

Balakrishnan, S., Start, P.R., Raghavan, D., Hudson, S.D., The Influence of clay and elastomer concentration on the morphology and fracture energy of preformed acrylic rubber dispersed clay filled epoxy nanocomposites, *Polymer* 46, 11255-11262.

Balch, D.K., Dunand, D.C. (2006), Load partitioning in aluminum syntactic foams containing ceramic cicrospheres, *Acta Materialia* 54 (6), 1501-1511.

Balch, D.K, O'Dwyer, J.G., Davis, G.R., Cady, C.M., Gray III, G.T., Dunand, D.C. (2005), Plasticity and damage in aluminum syntactic foams deformed under dynamic and quasi-static conditions, *Materials Science and Engineering A* 391, 408-417.

Banhart, J., Ashby, M.F. and Fleck, N.A. (1999), Metal foams and porous metal structures, Bremen: Verlag MIT Publishing.

Baroutaji, A., Sajjia, M., Olabi, AG. (2017), On the crashworthiness performance of thinwalled energy absorbers: recent advances and future developments, *Thin-Walled Structure* 118, 137-163.

Brook, R.J. (1995), Materials science and technology, Processing of Ceramics. Wiley-VCH.

Broxtermann, S., Vesenjak, M., Krstulovic-Opara, L., Fiedler, T. (2018), Quasi static and dynamic compression of zinc syntactic foams, *Journal of Alloys and Compounds* 768, 962-969.

Bunn, P., Mottram, J.T. (1992), Manufacture and compression properties of syntactic foams, *Composites* 24 (7), 565-571.

Castro, G., Nutt, S.R. (2012), Synthesis of syntactic steel foam using mechanical pressure infiltration, *Materials Science and Engineering A* 535, 274-280.

Chirwa, E.C. (1993), Theoretical analysis of tapered thin-walled metal inverbucktube, *International Journal of Mechanical Science* 35, 325-351.

Chittineni, K., Woldesenbet, E. (2010), Energy absorption of integrated functionally gradient syntactic foam, *Journal of Cellular Plastics* 46 (4), 295-319.

Chuang, C.H., Yang, R.J., Li, G., Mallela, K., Pothuraju, P. (2008), Multidisciplinary design optimization on vehicle tailor rolled blank design, *Structural Multidisciplinary Optimization* 35, 551-560.

Cox, J., Luong, D.D., Shunmugasamy, V.C., Gupta, N., Strbik, O.M., Cho, K. (2014), Dynamic and thermal properties of aluminium alloy A356/silicon carbide hollow particle syntactic foams, *Metals* 4 (4), 530-548.

D'Almeida & J.R.M. (1999), An analysis of the effect of the diameters of glass microspheres on the mechanical behaviour of glass-microsphere/epoxy-matrix composites, *Composites Science and Technology* 59, 2087-2091.

Daoud, A., *Abou* El-khair, M.T., Abdel-Aziz, M., Rohatgi, P. (2007), Fabrication, microstructure and compressive behaviour of ZC63 Mg-microballoon foam composites, *Composites Science and Technology* 67 (9), 1842-1853.

DIN 50134 standard (2018), Testing of metallic materials - Compression test of metallic cellular materials.

Dou, Z.Y., Jiang, L.T., Wu, G.H., Zhang, Q., Xiu, Z.Y., Chen, G.Q. (2007), High strain rate compression of cenosphere-pure aluminum syntactic foams. *Scripta Materialia* 57 (10), 945-948.

Durkin, S., Fowkes, N., Redwood, N., Bassom, A. (2016), Innovative approach to open pit edge protection, *Proceedings of ninth AusIMM open pit operators' conference, Conference, pp. 138-149.*

El-Sobky, H., Singace, A.A., Petsios, M. (2001), Mode of collapse and energy absorption characteristics of constrained frusta under axial impact loading, *International Journal of Mechanical Sciences* 43, 743-757.

Fan, T. (2016), Dynamic crushing behavior of functionally graded honeycomb structures with random defects. *International Journal of Materials Research* 107, 783-789.

Fang, J., Gao, Y., Sun, G., Zheng, G., Li, Q. (2015), Dynamic crashing behavior of new extrudable multi-cell tubes with a functionally graded thickness, *International Journal of Mechanical Sciences* 103, 63-73.

Ferguson, J.B., Santa Maria, J.A., Schultz, B.F., Rohatgi, P.K. (2013), Al-Al_2O_3 syntactic foams - Part II: Predicting mechanical properties of metal matrix syntactic foams reinforced with ceramic spheres, *Materials Science and Engineering A* 582, 423-432.

Ferreira, S.C., Velhinho, A., Silva, R.J.C., Rocha, L.A. (2010), Corrosion behaviour of aluminium syntactic functionally graded composites, *International Journal of Materials and Product Technology* 39 (1–2), 122-135.

Fiedler, T., Taherishargh, M., Krstulovic-Opara, L., Vesenjak, M. (2015), Dynamic compressive loading of expanded perlite/aluminum syntactic foam, *Materials Science and Engineering A* 626, 296-304.

Fu, J., Naguib, H.E. (2006), Effect of nanoclay on the mechanical properties of PMMA/Clay nanocomposite foams, *Journal of cellular plastics* 42, 325-342.

Gan, N., Feng, Y., Yin, H., Wen, G., Wang, D., Huang, X. (2016), Quasi-static axial crushing experiment study of foam-filled CFRP and aluminum alloy thin-walled structures, *Composite Structures* 157, 303-319.

Geng, H., Liu, J., Guo, A., Ren, S., Xu, X., Liu, S. (2016), Fabrication of heat-resistant syntactic foams through binding hollow glass microspheres with phosphate adhesive, *Material & Design* 95, 32-38.

George, R., Bardelcik, A., Worswick, M. (2012), Hot forming of boron steels using heated and cooled tooling for tailored properties, *Journal of Materials Processing Technology* 212, 2386-2399.

Gibson, L.J., Ashby, M.F. (1999), Cellular solids: structure and properties, Cambridge: Cambridge University Press.

Goel, M.D., Matsagar, V.A., Gupta, A.K. (2015), Blast resistance of stiffened sandwich panels with aluminum cenosphere syntactic foam, *International Journal of Impact Engineering* 77, 134-146.

Goel, M.D., Matsagar, V.A., Gupta, A.K., Marburg, S. (2013), Strain rate sensitivity of closed cell aluminium fly ash foam. *Transactions of Nonferrous Metals Society of China* 23 (4), 1080-1089.

Goel, M.D., Mondal, D.P., Yadav, M.S. and Gupta, S.K. (2014), Effect of strain rate and relative density on compressive deformation behavior of aluminum cenosphere syntactic foam, *Materials Science and Engineering A* 590, 406-415.

Goel, M.D., Peroni, M., Solomos, G., Mondal, D.P, Matsagar, V.A., Gupta, A.K., Larcher, M. and Marburg, S. (2012), Dynamic compression behavior of cenosphere aluminum alloy syntactic foam, *Materials & Design* 42, 418-423.

Griffith, A.A. (Ed.) (1924), Applied mechanics, Delft: Proc. First Int. Cong. 55-63.

Gupta, N. (2007), A functionally graded syntactic foam material for high energy absorption under compression. *Materials Letters* 61, 979-982.

Gupta, N., Nagorny, R. (2006), Tensile properties of glass microballoon-epoxy resin syntactic foams, *Journal of Applied Polymer Science* 102, 1254-1261.

Gupta, N., Ricci, W. (2006), Comparison of compressive properties of layered syntactic foams having gradient in microballoon volume fraction and wall thickness, *Materials Science and Engineering A 427*, 331-342.

Gupta, N., Rohatgi P.K.(2015), Metal matrix syntactic foams, processing, microstructure, properties and applications, First ed. Pennsylvania: DEStech Publication.

Gupta, N., Shunmugasamy, V.C. (2011), High strain rate compressive response of syntactic foams: trends in mechanical properties and failure mechanisms, *Materials Science and Engineering A* 528, 7596-7605.

Gupta, N., Woldesenbet, E., Mensah, P. (2004), Compression properties of syntactic foams: effect of cenosphere radius ratio and specimen aspect ratio, *Composites Part A* 35, 103-111.

Gupta, N., Ye, R., Porfiri, M. (2010), Comparison of tensile and compressive characteristics of vinyl ester/glass microballoon syntactic foams, *Composites Part B* 41 (3), 236-245.

Gupta, N., Zeltmann, S.E., Shunmugasamy, V.C., Pinisetty, D. (2014), Applications of polymer matrix syntactic foams, *Journal of the Minerals, Metals & Materials Society* 66 (2), 245-254

Hangai, Y., Takahashi, K., Utsunomiya, T., Kitahara, S., Kuwazuru, O., Yoshikawa, N. (2012) Fabrication of functionally graded aluminium foam using aluminium alloy die castings by friction stir processing, *Materials Science and Engineering A* 534, 716-719.

Hangai, Y., Zushida, K., Kuwazuru, O., Yoshikawa, N. (2016), Functionally graded Al foam fabricated by sintering and dissolution process with remaining spacers, *Materials Transactions* 57 (5), 748-750,

Hartmann, M., Crößman, I., Reindel, K. and Singer, R.F. (1999), Behaviour of composites structures, in Banhart, J., Ashby, M.F. and Fleck N.A. (eds), *Metal Foams and Porous Metal Structures*, Bremen: Verlag MIT, pp. 331-6.

Harrigan, J.J., Reid, S.R., Tan, P.J., Reddy, T.Y. (2005), High rate crushing of wood along the grain. *International Journal of Mechanical Sciences*. 47 (4-5), 521–544.

Hassani, A., Habibolahzadeh, A., Bafti, H. (2012), Production of graded aluminium foams via powder space holder technique, *Material & Design* 40, 510-515.

He, S.Y., Zhang, Y., Dai, G., Jiang, J.Q. (2014), Preparation of density-graded aluminium Foam, *Materials Science and Engineering A* 618, 496-499,

Hebert, M., Rousseau, C.E., Shukla, A. (2008), Shock loading and drop weight impact response of glass reinforced polymer composites, *Composite Structures* 84 (3), 199-208.

Hinves, J.B and Douglas, C.D. (1993), The development of a hybrid advanced composite syntactic foam structural component for use in undersea vehicles, IEEE III, pp. 468-472.

Ho, M.W., Lam, C.K., Lau, K.T., Ng, D.H.L., Hui, D. (2006), Mechanical properties of epoxy-based composites using nanoclays, *Composite Structures* 75, 415-421.

Huang, R., Li, P. (2015), Elastic behaviour and failure mechanism in epoxy syntactic foams: the effect of glass microballoon volume fractions. *Composite Part B* 78, 401-408.

Huang, R., Li, P., Liu, T. (2016), X-ray microtomography and finite element modelling of compressive failure mechanism in cenosphere epoxy syntactic foams, *Composite Structures* 140, 157-165.

Hull, D., Clyne, T.W. (1996), An introduction to composite materials, Cambridge: Cambridge University Press.

Hussain, F., Chen, J., Hojjati, M. (2007), Epoxy-silicate nanocomposites: cure monitoring and characterization, *Materials Science and Engineering A* 445-446, 467-476.

Jahsman, W.E. (1968), Static and dynamic material behaviour of syntactic foam, *Mechanical Behaviour of Materials under Dynamic Loads*, U.S. Lindholm, ed., Springer- Verlag, 365-387

Jamil, A., Guan, Z.W. and Cantwell, W.J. (2017), The static and dynamic response of CFRP tube reinforced polyurethane, *Composite Structure* 161, 85-92

Jayatilaka, D.S. (1979), Fracture of engineering brittle Materials, London: Applied Science Publishers.

Johnson, W. (1972), Impact strength of materials, London: Edward Arnold.

Karagiozova, D., Alves, M. (2015), Propagation of compaction waves in cellular materials with continuously varying density. *International Journal of Solids and Structures*. 71, 323-337

Karagiozova, D., Langdon, G.S., Nurick, G.N. (2010), Blast attenuation in cymat foam core sacrificial claddings. *International Journal of Mechanical Sciences*. 52 (5), 758-776.

Karagiozova, D., Langdon, G.S., Nurick, G.N. (2012), Propagation of compaction waves in metal foams exhibiting strain hardening. *International Journal of Solids and Structures*. 49 (19-20), 2763-2777.

Karbasian, H., Tekkaya, A.E. (2010), A review on hot stamping, *Journal of Materials Processing Technology* 210, 2103-2118.

Karthikeyan, C.S., Sankaran, S., Kumar, M.N.J., Kishore (2000), Processing the compressive strength of syntactic foams with and without fibrous reinforcements, *Journal of Applied Polymer Science* 81, 405-411.

Kim, H.S., Khamis, M.A. (2001), Fracture and impact behaviours of hollow micro-sphere/epoxy resin composites, *Composites Part A* 32 (9), 1311-1317.

Kim, H.S., Oh, H.H. (2000), Manufacturing and impact behavior of syntactic foam, *Journal of applied polymer science* 76 (8), 1324-1328.

Kiser, M., He, M.Y., Zok, F.W. (1999), The mechanical response of ceramic microballoon reinforced aluminum matrix composites under compressive loading, *Acta Materialia* 47 (9), 2685-2694.

Kishore, Shankar, R., Sankaran, S. (2005), Gradient syntactic foams: Tensile strength, modulus and fractographic features, *Materials Science and Engineering A* 412, 153-158.

Koopman, M., Chawla, K.K., Carlisle, K.B., Gladysz, G.M. (2006), Microstructural failure modes in three-phase glass syntactic foams, *Journal of Materials Science* 41, 4009-4014.

Kranjc, M., Zupanic, A., Miklavcic, D., Jarm, T. (2010), Numerical analysis and thermographic investigation of induction heating, *International Journal of Heat and Mass Transfer* 53, 3585-3591.

Lam, C.K., Cheung, H.Y., Lau, K.T., Zhou, L.M., Ho, M.W., Hui, D. (2005), Cluster size effect in hardness of nanoclay/epoxy composites, *Composites Part B* 36, 263-269.

Lapčík, L., Ruszala, M.J.A., Vašina, M., Lapčíková, B., Vlček, J., Rowson, N.A., Grover, L.M., Greenwood, R.W. (2016), Hollow spheres as nanocomposite fillers for aerospace and automotive composite materials applications, *Composites: Part B* 106, 74-80.

Lau, K-t., Gu, C., Hui, D. (2006), A critical review on nanotube and nanotube/nanoclay related polymer composite materials. *Composites Part B* 37 (6), 425-436.

Le Gall, M., Choqueuse, D., Le Gac, P-Y., Davies, P., Perreux, D. (2014), Novel mechanical characterization method for deep sea buoyancy material under hydrostatic pressure, *Polymer Testing* 39 (Supplement C), 36-44.

Li, G., Jones, N. (2007), Development of rubberized syntactic foam, *Composites Part A* 38, 1483-1492.

Li, G., John, M. (2008), A crumb rubber modified syntactic foam, *Materials Science and Engineering A* 474, 390-399.

Li, P., Petrinic, N., Siviour, C.R., Froud, R., Reed, J.M. (2015), Strain rate dependent compressive properties of glass microballoon epoxy syntactic foams. *Materials Science and Engineering A* 515(1-2), 19-25.

Licitra, L., Luong, D.D., Strbik, O.M. and Gupta, N. (2015), Dynamic properties of alumina hollow particle filled aluminium alloy A356 matrix syntactic foams, *Materials and Design: Part B* 66, 504-515.

Lopatnikov, S.L., Gama, B.A., Haque, M.J., Krauthauser, C., Gillespie Jr., J.W. (2004), High-velocity plate impact of metal foams. *International Journal of Impact Engineering*. 30 (4), 421-445

Luong, D.D., Gupta, N., Daoud, A., Rohatgi, P.K. (2011), High strain rate compressive characterization of aluminium alloy/fly ash cenosphere composites, *Journal of the Minerals, Metals & Materials Society* 63 (2), 53-56.

Luong, D.D., Gupta, N., Rohatgi, P.K. (2011), The high strain rate compressive response of Mg-Al alloy/fly ash cenosphere composites. *Journal of the Minerals, Metals & Materials Society* 63 (2), 48-52.

Luong, D.D., Shunmugasamy, V.C., Gupta, N., Lehmhus, D., Weise, J., Baumeister, J. (2015), Quasi-static and high strain rates compressive response of iron and invar matrix syntactic foams. *Material & Design* 66, 516-531.

Luong, D.D., Strbik, O.M., Hammond, V.H., Gupta, N. and Cho, K. (2013), Development of high performance lightweight aluminum alloy/SiC hollow sphere syntactic foams and compressive characterization at quasi-static and high strain rates, *Journal of alloys and compounds* 550, 412-422.

Maharsia, R., Gupta, N., Jerro, H.D. (2006), Investigation of flexural strength properties of rubber and nanoclay reinforced hybrid syntactic foams. *Materials Science and Engineering A* 417, 249-258.

Májlinger, K., Orbulov, I.N. (2014), Characteristic compressive properties of hybridmetal matrix syntactic foams, *Materials Science and Engineering A* 606, 248-256.

Mamalis, A.G., Johnson, W. (1983), The quasi-static crumpling of thin-walled circular cylinders and frusta under axial compression, *International Journal of Mechanical Sciences* 25, 713-732.

Mamalis, A.G., Johnson, W., Viegelahn, G.L. (1984), The crumpling of steel thin-walled tubes and frusta under axial compression at rlevated strain-rates: some experimental results, *International Journal of Mechanical Sciences* 26, 537-547.

Mamalis, A.G., Manolakos, D.E., Saigal, S., Viegelahn, G., Johnson, W. (1986), Extensible plastic collapse of thin-wall frusta as energy absorbers, *International Journal of Mechanical Sciences* 28, 219-229.

Marchi, C.S., Mortensen, A. (2002), Material definitions, processing and recycling, in Degischer, H. and Kriszt, B. (eds), Handbook of Cellular Metals, Weinheim: Viley, 43-56.

Mondal, D.P., Datta Majumder, J., Jha, N., Badkul, A., Das, S., Patel, A. (2012), Titanium-cenosphere syntactic foam made through powder metallurgy route, *Material & Design* 34, 82-89.

Mondal, D.P., Goel, M.D., Bagde, N., Jha, N., Sahu, S., Barnwal, A.K. (2014), Closed cell ZA27-SiC foam made through stir-casting technique, *Materials & Design* 57 (Supplement C), 315-324.

Mondal, D.P., Goel, M.D., Das, S. (2009), Compressive deformation and energy absorption characteristics of closed cell aluminum-fly ash particle composite foam. *Materials Science and Engineering A* 507, 102-109.

Mondal, D.P., Goel, M.D., Das, S. (2009), Effect of strain rate and relative density on compressive deformation behaviour of closed cell aluminum-fly ash composite foam. *Material & Design* 30 (4), 1268-1274.

Mousanezhad, D., Ghosh, R., Ajdari, A., Hamouda, A., Nayeb-Hashemi, H., Vaziri, A. (2014), Impact fesistance and energy absorption of regular and functionally graded hexagonal honeycombs with cell wall material strain hardening. *International Journal of Mechanical Sciences* 89, 413-422.

Movahedi, N., Murch, G.E., Belova, I.V. and Fiedler, T. (2019), Functionally graded metal syntactic foam: fabrication and mechanical properties, *Materials & Design* 168, 107652.

Myers, K., Katona, B., Cortes, P. and Orbulov, I.N. (2015), Quasi-static and high strain rate response of aluminum matrix syntactic foams under compression, *Composites Part A* 79, 82-91.

Nadler, J.H., Hurysz, K.M., Clark, J.L., Cochran, J.K., Lee, K.J., Sanders, J. (1999), Sintering methods, in Banhart, J., Ashby, M.F., Fleck, N.A. (eds), Metal Foams and Porous Metal Structures, Bremen: Verlag MIT, 179-182.

Naebe, M., Shirvanimoghaddam, K. (2016), Functionally graded materials: a review of fabrication and properties, *Applied Materials Today* 5, 223-245.

Nagel, G.M., Thambiratnam, D.P. (2004), A numerical study on the impact response and energy absorption of tapered thin-walled tubes, *International Journal of Mechanical Sciences* 46, 201-216.

Nagel, G.M., Thambiratnam, D.P. (2005), Computer simulation and energy absorption of tapered thin-walled rectangular tubes, *Thin-walled Structures* 43, 1225-1242.

Nagel, G.M., Thambiratnam, D.P. (2006), Dynamic simulation and energy absorption of tapered thin-walled tubes under oblique impact loading, *International Journal of Impact Engineering* 32, 1595-1620.

Omar, M.Y., Xiang, C., Gupta, N., Strbik, O.M. and Cho, K. (2015), Syntactic foam core metal matrix sandwich composite: compressive properties and strain rate effects, *Materials Science and Engineering A* 643, 156-168.

Orbulov, I.N., Ginsztler, J. (2012), Compressive behaviour of metal matrix syntactic foams, *Acta Polytech Hungarica* 9 (2), 43-56.

Orbulov, I.N., Májlinger, K. (2013), Description of the compressive response of metal matrix syntactic foams, *Materials & Design* 49, 1-9.

Orbulov, I.N., Májlinger, K. (2014), Compressive properties of metal matrix syntactic foams in free and constrained compression, *Journal of the Minerals Metals & Materials Society* 66 (6), 882-891.

Orbulov, I.N., Nemeth, A., Dobránszky, J. (2010), Compressive strength and hardness of metal matrix syntactic foams. *Journal of Physics: Conference Series* 240, 012168.

Ouellet, S., Cronin, D., Worswick, M. (2006), Compressive response of polymeric foams under quasi-static, medium and high strain rate conditions. *Polymer Testing* 25 (6), 731-743.

Palmer, R.A., Gao, K., Doan, T.M., Green L., Cavallaro, G. (2007), Pressure infiltrated syntactic foams-process development and mechanical properties, *Materials Science and Engineering A* 464, 85-92.

Park, C., Nutt, S.R. (2002), Strain rate sensitivity and fefects in steel foam, *Materials Science and Engineering A* 323 (1-2), 358-366.

Perez-Santiago, R. Billur, E., Ademaj, A., Sarmiento, C., Berlanga, R., Altan, T. (2013), Hot stamping a B-pillar with tailored properties: experiments and preliminary simulation results, International Hot Stamping conferences, Lulea, Sweden.

Peroni, L., Scapin, M., Fichera, C. Lehmhus, D., Weise, J., Baumeister, J., Avalle, M. (2014), Investigation of the mechanical behaviour of AISI 316L stainless steel syntactic foams at different strain-rates, *Composites Part B* 66, 430-442.

Pham, T.M., Chen, W., Hao, H. (2018), Failure and impact resistance analysis of plain and fiber-reinforced-polymer confined concrete cylinders under axial impact loads, *International Journal of Protective Structures* 9 (1), 4-23.

Pham, T.M., Chen, W., Kingston, J. and Hao, H. (2018), Impact response and energy absorption of single phase syntactic foam, *Composites Part B* 150, 226-233.

Pham, T.M., Kingston, J., Strickland, G., Chen, W., Hao, H. (2018), Effect of crumb rubber on mechanical properties of multi-phase syntactic foams, *Polymer Testing* 66, 1-12.

Puga, H., Carneiro, V.H., Jesus, C., Pereira, J., Lopes, V. (2018), Influence of particle diameter in mechanical performance of Al expanded clay syntactic foams, *Composite Structures* 184, 698-703.

Reid, S.R., Bell, W.W., Barr, R.A. (1983), Structural plastic shock model for one-dimensional ring systems, *International Journal of Impact Engineering*, 1 (2), 175-191.

Reid, S.R., PENG, C. (1997), Dynamic uniaxial crushing of wood, *International Journal of Impact Engineering*, 19 (5-6), 531-570

Rieder, K.A. and Mindess, S. (1998), New test method to evaluate the impact behaviour of biaxially confined concrete. *Materials and Structures* 31 (10), 669-675.

Rohatgi, P.K., Daoud, A., Schultz, B.F., Puri, T. (2009), Microstructure and mechanical behavior of die casting AZ91D-Fly ash cenosphere composites, *Science Direct* 40, 883-896.

Rohatgi, P.K., Gajdardziska-Josifovska, M., Robertson, D.P., Kim, J.K., Guo, R.Q. (2002), Age-hardening characteristics of aluminum alloy-hollow fly ash composites, *Metallurgical and Materials Transactions A* 33A, 1541-1547.

Rohatgi, P.K., Kim, J.K., Gupta, N., Alaraj, S., Daoud, A. (2006), Compressive characteristics of A356/Fly ash cenosphere composites synthesized by pressure infiltration technique, *Composites Part A* 37(3), 430-437.

Rostilov, T.A., Ziborov, V.S. (2021), Experimental study of shock wave structure in syntactic foams under gigh-velocity impact, *Acta Astronautica*, 178, 900-907

Rousseau, C.E., Plume, G., Goni, M. and Ale, B. (2017), Behavior of syntactic foam under plate impact, *Mechanics Research Communications* 83, 1-5.

Ruan, D., Lu, G., Wang, B., Yu, T.X. (2003), In-plane dynamic crushing of honeycombs-a finite element study, *International Journal of Impact Engineering* 28, 161-182.

Santa Maria, J.A., Schultz, B.F., Ferguson, J.B., Gupta, N., Rohatgi, P.K. (2014), Effect of hollow sphere size and size distribution on the quasi-static and high strain rate compressive properties of Al-A380-Al_2O_3 syntactic foams, *Journal of Materials Science* 49, 1267-1278.

Santa Maria, J.A., Schultz, B.F., Ferguson, J.B., Rohatgi, P.K. (2013), Al-Al_2O_3 syntactic foams - PartI: effect of matrix strength and hollow sphere size on the quasi-static properties of Al-A206/Al_2O_3 syntactic foams, *Materials Science and Engineering A* 582, 415-422.

Shams, A., Panteghini, A., Bardella, L., Porfiri, M. (2017), A micromechanical model to study failure of polymer-glass syntactic foams at high strain rates. *Computational Materials Science* 135, 189-204.

Shen, C., Lu, G., Yu, T. (2013), Dynamic behavior of graded honeycombs-a finite element study, *Composite Structures* 98, 282-293.

Shen, C., Lu, G., Yu, T., Ruan, D. (2015), Dynamic response of a cellular block with varying cross-section. *International Journal of Impact Engineering* 79, 53-64.

Song, B., Chen, W., Frew, D.J. (2004), Dynamic compressive response and failure behaviour of an epoxy syntactic foam, *Journal of composite materials* 38, 915-936.

Song, B., Chen, W., Lu, W. (2007), Mechanical characterization at intermediate strain rates for rate effects on an epoxy syntactic foam. *International Journal of Mechanical Sciences* 49 (12), 1336-1343.

Sun, G., Xu, F., Li, G., Li, Q. (2014), Crashing analysis and multiobjective optimization for thinwalled structures with functionally graded thickness. *International Journal of Impact Engineering* 64, 62-74.

Swetha, C., Kumar, R. (2011), Quasi-static uniaxial compression behaviour of hollow glass microspheres/epoxy based syntactic foams, *Material & Design* 32 (8-9), 4152-4163.

Szlancsik, A., Katona, B., Bobor, K., Majlinger, K., Orbulov, I.N. (2015), Compressive behaviour of aluminium matrix syntactic foams reinforced by iron hollow spheres, *Materials & Design* 83, 230-237.

Taherishargh, M., Belova, I.V., Murch, G.E., Fiedler, T. (2014), Low-density expanded perlite-aluminium syntactic foam, *Materials Science and Engineering A* 604, 127-134.

Taherishargh, M., Belova, I.V., Murch, G.E., Fiedler, T. (2015), Pumice/aluminium syntactic foam, *Materials Science and Engineering A* 635, 102-108.

Tan, P.J., Reid, S.R., Harrigan, J.J., Zou, Z., Li, S. (2005a), Dynamic compressive strength properties of aluminium foams. Part I - experimental data and observation. *Journal of the Mechanics and Physics of Solids*, 53 (10), 2174-2205.

Tan, P.J., Reid, S.R., Harrigan, J.J., Zou, Z., Li, S. (2005b), Dynamic compressive strength properties of aluminium foams. Part II - shock theory and comparison with experimental data. *Journal of the Mechanics and Physics of Solids*, 53 (10), 2206-2230.

Tao, X.F., Zhang, L.P., Zhao, Y.Y. (2009), Al matrix syntactic foam fabricated with bimodal ceramic microspheres, *Materials & Design* 30, 2732-2736.

Tao, X.F., Zhao, Y.Y. (2009), Compressive behaviour of Al matrix syntactic foams toughened with Al particles, *Scripta Materialia* 61(5), 461-464.

Tao, X.F., Zhao, Y.Y. (2012), Compressive failure of Al alloy matrix syntactic foams manufactured by melt infiltration, *Materials Science and Engineering A* 549, 228-232.

Viot, P., Shankar, K., Bernard, D. (2008), Effect of strain rate and density on dynamic behaviour of syntactic foam. *Composite Structures* 86 (4), 314-327.

Wang, H., Zhou, X.Y., Long, B., Liu, H.Z. (2013), Compression behavior of Al_2O_3k/Al composite materials fabricated by counter-gravity infiltration casting. *Materials Science and Engineering A* 582, 316-320.

Woldesenbet, E. (2008), Low velocity impact properties of nanoparticulate syntactic foams, *Materials Science and Engineering A* 496, 217-222.

Woldesenbet, E., Gupta, N., Jadhav, A. (2005), Effect of density and strain rate on properties of syntactic foams, *Journal of Materials Science* 40 (15), 4009-4017.

Woldesenbet, E., Peter, S. (2009), Radius ratio effect on high-strain rate properties of syntactic foam composites, *Journal of Materials Science* 44, 1551-1559.

Woldesenbet, E., Sankella, N. (2009), Flexural properties of nanoclay syntactic foam sandwich structures, *Journal of sandwich structure & materials* 11, 425-444.

Wouterson, E.M., Boey, F.Y.C., Hu, X., Wong, S.C. (2007), Effect of fiber reinforcement on the tensile, fracture and thermal properties of syntactic foam, *Polymer* 48 (11), 3183-3191.

Wu, G.H., Dou, Z.Y., Sun, D.L., Jiang, L.T. (2007), Compression behaviours of cenosphere-pure aluminum syntactic foams, *Scripta Materialia* 56, 221-224.

Wu, X., Dong, L., Zhang, F., Zhou, Y., Wang, L., Wang, D., Yin, Y. (2016), Preparation and characterization of three phase epoxy syntactic foam filled with carbon fiber reinforced hollow epoxy macrospheres and hollow glass microspheres. *Polymer Composites* 37 (2), 497–502.

Wu, X., Wang, Y., Yang, X., Yu, J., Wang, L., Hou, S., Jiang, P.A. (2015), "Rolling ball method" to make glass fiber reinforced hollow epoxy macrospheres used for a three phase epoxy syntactic foam, *RSC Advances* 5 (75), 61204-17.

Xia, X., Feng, J., Ding, J., Song, K., Chen, X., Zhao, W. (2015), Fabrication and characterization of closed-cell magnesium-based composite foams, *Material & Design* 74, 36-43.

Xu, Z., Hao, H. Li, H.N. (2012), Experimental study of dynamic compressive properties of fibre reinforced concrete material with different fibres. *Materials & Design* 33, 42-55.

Xue, X.B., Wang, L.Q., Wang, M.M., Lü, W.J., Zhang, D. (2012), Manufacturing, compressive behaviour and elastic modulus of Ti matrix syntactic foam fabricated by powder metallurgy, *Transactions of Nonferrous Metals Society of China* 22, 188-192.

Yang, R.J., Fu, Y., Li, G. (2007), Application of tailor rolled blank in vehicle front end for frontal impact, *SAE International* 2007-01-0675.

Yin, H., Fang, H., Wen, G., Wang, Q., Xiao, Y. (2016), An adaptive RBF-based multi-objective optimization method for crashworthiness design of functionally graded multi-cell tube, *Structural Multidisciplinary Optimization* 53, 129-144.

Yu, H., Guo, Z., Li, B., Yao, G., Luo, H., Liu, Y. (2007), Research into the effect of cell diameter of aluminum foam on its compressive and energy absorption properties, *Materials Science and Engineering A* 454, 542-546.

Yu, M., Zhu, P., Ma, Y. (2012), Experimental study and numerical prediction of tensile strength properties and failure modes of hollow spheres filled syntactic foams, *Computational Material Science* 63, 232-243.

Zaretsky, E., Ben-dor, G. (1995), Compressive stress-strain relations and shock hugoniot curves of flexible foams, *Journal of Engineering Materials and Technology*, 117 (3) 278-28

Zhang, B., Lin, Y., Li, S., Zhai, D. and Wu, G. (2016), Quasi-static and high strain rates compressive behavior of aluminum matrix syntactic foams, *Composites: Part B* 98, 288-296.

Zhang, J., Wei, H., Wang, Z., Zhao, L. (2015), Dynamic crushing of uniform and density graded cellular structures based on the circle arc model, *Latin American Journal of Solids and Structures* 12, 1102-1125.

Zhang, L.P., Zhao, Y.Y. (2007), Mechanical response of Al matrix syntactic foams produced by pressure infiltration casting, *Journal of Composite Materials* 41(17), 2105-2117.

Zhang, Q., Lee, P.D., Singh, R., Wu, G.H., Lindley, T.C. (2009), Micro-CT characterization of structure features and deformation behavior of fly ash/aluminum syntactic foam, *Acta Materialia* 57, 3003-3011.

Zhang, X., An, L., Ding, H. (2014), Dynamic crushing behavior and energy absorption of honeycombs with density gradient. *Journal of Sandwich Structures and Materirals* 16, 125-147.

Zhang, X., Leng, K., Zhang, H. (2017), Axial Crushing of Embedded Multi-cell Tubes, *International Journal of Mechanical Sciences* 131-132, 459-470.

Zhang, X., Wen, Z., Zhang, H. (2014), Axial crushing and optimal design of square tubes with graded thickness, *Thin-walled Structures* 84, 263-274.

Zhang, X., Zhang, H. (2013), Energy absorption of multi-cell stub columns under axial compression, *Thin-Walled Structures* 68, 156-163.

Zhao, Y.Y, Tao, X.F. (2009), Behaviour of metal matrix syntactic foams in compression, *Journal of Materials Science & Technology* 25, 1785-1794.

Zheng, Z.J., Liu, Y.D., Yu, J.L., Reid, S.R. (2012), Dynamic crushing of cellular material: continuum-based wave models for transitional and shock modes. *International Journal of Impact Engineering*. 42, 66-79

Zou, L.C., Zhang, Q., Pang, B.J., Wu, G.H., Jiang, L.T. and Su, H. (2013), Dynamic compressive behavior of aluminum matrix syntactic foam and its multilayer structure, *Materials and Design* 45, 555-560.